Conductive probe based investigations on ZnO varistor ceramics

Andreas Nevosad

A dissertation submitted to the Institute of Physics Montanuniversität Leoben
in partial fulfillment of the requirements for the degree of Doktor der montanistischen Wissenschaften

Under supervision of
Ao. Univ. Prof. Dr. Christian Teichert

Refereed by
Ao. Univ. Prof. Dr. Christian Teichert and
Ao. Univ. Prof. Dr. Klaus Reichmann

Institute of Physics
Montanuniversität Leoben
November 2013

Eidesstattliche Erklärung:

Ich erkläre an Eides statt, dass ich diese Arbeit selbstständig verfasst, andere als die angegebenen Quellen und Hilfsmittel nicht benutzt und mich selbst auch sonst keiner unerlaubten Hilfsmittel bedient habe.

Affidavit:

I declare in lieu of oath, that I wrote this thesis and performed the associated research myself, using only literature cited in this volume.

Leoben, November 2013, Andreas Nevosad

Dedicated to Marlies

Keywords

Varistor, ZnO, grain boundaries, atomic force microscopy (AFM), conductive atomic force microscopy (C-AFM), Kelvin probe force microscopy (KPFM), scanning surface potential microscopy (SSPM), micro four-point probe (M4PP);

Author:

Dipl. Ing. Andreas Nevosad

Contact:

andreas.nevosad@gmail.com
Institute of Physics, Montanuniversitaet Leoben
Franz-Josef Strasse 18, 8700 Leoben, AUSTRIA
Tel +43 3842 402 4601; Fax +43 3842 402 4602
www.unileoben.ac.at\~ spmgroup

Abstract

Varistors are non-linear, voltage dependent resistors. Due to this property they are used as over-voltage protection in electric circuits and electronic devices. The standard material for the manufacturing of varistors are doped ZnO ceramics. Their special electrical behavior is caused by the formation of so-called double Schottky barriers at the ZnO grain boundaries. Therefore, the determination of the electrical properties of individual grain boundaries is crucial for a deeper understanding in the behavior of varistor devices.
In this work, the electrical properties of industrially manufactured varistor ceramics were investigated with regard to the microstructure. The experimental techniques employed were on the one hand variants of atomic force microscopy (AFM) and on the other hand a new micro four-point probe (M4PP) measurement setup. The utilized AFM based methods were conductive atomic force microscopy (C-AFM), Kelvin probe force microscopy (KPFM), scanning surface potential microscopy (SSPM), and scanning impedance microscopy (SIM).
The AFM investigations revealed a high conductivity of the ZnO grain interior and a high resistivity of the grain boundaries. KPFM and SSPM allowed to identify a specific grain boundary with reduced resistance causing a preferred current path, which was previously found by thermography measurements. Furthermore, it was possible to detect asymmetric behavior for current paths across two grain boundaries.
The M4PP measurements allowed to investigate the current to voltage characteristics of individual grain boundaries, at which asymmetries and strong variations in the parameters - most important for the device performance - were found.

Kurzfassung

Varistoren sind nicht-lineare, spannungsabhängige Widerstände. Aufgrund dieser Eigenschaft werden sie als Überspannungsschutz in elektrischen Schaltkreisen und Elektronikbauteilen verwendet. Das Standardmaterial zur Herstellung von Varistoren sind dotierte ZnO-Keramiken. Deren spezielles elektrisches Verhalten wird durch die Bildung von Doppel-Schottky-Barrieren an den ZnO-Korngrenzen verursacht. Daher ist die Bestimmung der elektrischen Eigenschaften individueller Korngrenzen grundlegend für das Verständnis des Verhaltens von Varistor-Bauteilen.
In dieser Arbeit wurden die elektrischen Eigenschaften von industriell hergestellten Varistor-Keramiken in Bezug auf die Mikrostruktur untersucht. Die verwendeten Untersuchungsmethoden waren einerseits Varianten der Rasterkraftmikroskopie (Atomic Force Microscopy, AFM) und andererseits ein neu aufgebautes Mikro-Vier-Punkt-Messsystem (M4PP). Als Rasterkraftmikroskopie - basierte Methoden wurden die Leitfähigkeits-Rasterkraftmikroskopie (Conductive Atomic Force Microscopy, C-AFM), Kelvinsonden-Rasterkraftmikroskopie (Kelvin Probe Force Microscopy, KPFM), Oberflächenpotential-Rasterkraftmikroskopie (Scanning Surface Potential Microscopy, SSPM) und Impedanz-Rasterkraftmikroskopie (Scanning Impedance Microscopy, SIM) verwendet.
Die AFM Untersuchungen zeigten eine hohe Leitfähigkeit innerhalb des ZnO Korns und einen hohen Widerstand an den Korngrenzen. Mittels KPFM und SSPM konnte ein, mit Thermographie gefundener, Hauptstrompfad durch ein Bauteil genau lokalisiert werden und die Bildung des Strompfades einer spezifischen Korngrenze mit reduziertem Widerstand zugeordnet werden. Weiters konnte asymmetrisches Verhalten auch für Strompfade über zwei Korngrenzen nachgewiesen werden.
Die M4PP Messungen erlaubten eine Untersuchung der Strom-Spannungs Charakteristik einzelner Korngrenzen, wobei Asymmetrien und starke Unterschiede in den für das Verhalten des Bauteiles wichtigen Parameter gefunden wurden.

Contents

1 Introduction 1

2 Fundamentals 3
2.1 ZnO . . . 3
2.2 ZnO varistor ceramics . . . 4
2.2.1 Manufacturing process of multilayer varistors . . . 5
2.2.2 Grain boundary behavior . . . 6
2.2.3 Dopants in ZnO varistor ceramics . . . 7
2.3 Atomic force microscopy . . . 10
2.3.1 Conductive atomic force microscopy . . . 10
2.3.2 Kelvin probe force microscopy and scanning surface potential microscopy . . . 11
2.3.3 Scanning impedance microscopy . . . 13
2.4 Four-point probe . . . 14
2.5 Electron backscatter diffraction . . . 15
2.6 Lock-in thermography . . . 16

3 Experimental 17
3.1 Sample preparation . . . 17
3.2 Keithley 2636A dual source meter . . . 18
3.3 Atomic force microscopy . . . 19
3.3.1 Conductive atomic force microscopy . . . 19
3.3.2 Kelvin probe force microscopy, scanning surface potential microscopy 20
3.3.3 Scanning impedance microscopy . . . 20
3.4 Micro four-point probe . . . 21
3.5 Electron backscatter diffraction . . . 24
3.6 Lock-in thermography . . . 25

4 Results **27**
4.1 Praseodymium system, AFM based investigations 27
4.1.1 C-AFM investigations 27
4.1.2 KPFM and SSPM investigations 33
4.1.3 SIM investigations 39
4.2 Praseodymium system, Micro four-point probe investigations 48
4.2.1 Simulation 48
4.2.2 Experimental results 50
4.3 Bismuth-system, AFM based investigations 58
4.3.1 C-AFM investigations 58
4.3.2 KPFM and SSPM investigations 59

5 Summary and Outlook **61**

1 Introduction

Varistors (**Var**iable Res**istor**) are passive electronic components which are widely used as overvoltage protection in electric circuits and electronic devices. They show a highly non-linear current to voltage behavior with typical exponential factors between 20 and 70 [1]. Commercial varistors are available in as stacks sizes of meters for the protection of high voltage power lines with AC fields of hundreds of kV, down to sub-millimeter small surface mounted devices which are operated at a few volts in DC.

The first ceramic material with pronounced varistor behavior was manufactored in the early 1930s from partially sintered SiC particles [2]. In 1969, the first ZnO based varistor material was developed by M. Matsuoka at Matsushita Electric (Japan). Nowadays, polycrystalline ZnO ceramics with Pr or Bi doping, which show highly non-linear current-voltage characteristics with rapidly decreasing resistance above a specific switching voltage, are the standard varistor materials [3, 4, 5]. These ceramics form so called double Schottky barriers at the grain boundaries which are causing the strong varistor effect [6]. Each electrically active ZnO grain boundary between the electrodes shifts the switching voltage by about 3 V [2]. This allows to adjust the switching voltage of the device by increasing the number of grain boundaries between the electrodes due to smaller grains or a larger electrode distance.

Open questions in the research of ZnO varistors are the correlation between the formation of the barrier at the grain boundary and the crystallographic orientation of the ZnO grains. Also the contribution of the polarity in the ZnO crystals to the formation of the double Schottky barrier at the grain boundary is not yet fully understood. Furthermore, the quality and the spread of the barrier properties within a varistor ceramic is not clarified yet [1].

Aim of this work was the electrical characterization of industry grade varistor materials [7, 8] on the micro-structural level with special respect to the correlation between the electrical properties of individual grain boundaries (GBs) and the crystallographic orientation of the GB and the adjacent grains.

For the electrical characterization of individual grain boundaries, conductive probe based methods like atomic force microscopy (AFM) [9] and a newly established micro four-point probe (M4PP) are appropriate to characterize polycrystalline varistor ceramics with micrometer sized grains.
As AFM based techniques, conductive atomic force microscopy (C-AFM) [10, 11], Kelvin probe force microscopy (KPFM) [12, 13], scanning surface potential microscopy (SSPM) [14, 15, 16] and scanning impedance microscopy (SIM)[17, 18] were employed.
Additional measurements were made in collaboration with Materials Center Leoben (MCL) and Erich Schmidt Institut (ESI) Leoben which made the electron backscatter diffraction (EBSD) investigations [19]. The EBSD investigations were performed to find a possible relation between the electrical properties and the crystallographic orientation.
This work focuses on praseodymium doped multilayer varistor (MLV) samples with a low switching voltage and therefore a small number of active grain boundaries between the electrodes. These samples were investigated with regard to asymmetric device behavior. Lock-in thermography - performed at the Institut für Struktur- und Funktionskeramik, Montanuniversität Leoben (ISFK) - revealed the formation of hot spots in these samples. SSPM allowed to detect the specific grain boundary which is causing a preferred current path at the hot spot [20]. Due to the large grain size, these samples were also used in the M4PP investigations, where it was possible to measure the electrical properties of individual grain boundaries. These microscopic investigations revealed a wide variation of electrical properties of the individual grain boundaries, which was not expected from macroscopic measurements. Further investigations were performed on praseodymium doped and bismuth doped samples with smaller grain size and therefore higher switching voltage.
This work was performed within the framework of the FFG bridge project # 824890 "Zusammenhang zwischen dem Mikrogefüge und den makroskopischen, elektrischen Eigenschaften von Zinkoxid-Varistoren". The obtained electrical properties were used in a cooperating work by Michael Hofstätter to develop a network model to simulate the electrical properties of entire devices [21].

2 Fundamentals

2.1 ZnO

ZnO is a II-VI compound semiconductor with a direct bandgap of $\sim$3.37 eV at 300 K [5, 22, 23]. Under ambient conditions, ZnO forms the hexagonal wurtzite structure, which is depicted in Fig. 2.1. The Zn cations and O anions in the wurtzite structure are arranged in tetrahedrons where one species of atoms is surrounded by the other and vice versa. This structure shows crystallographic polarity and piezoelectricity because it does not posses an inversion symmetry. By convention, the [0001] axis is the positive z-direction and points from the O terminated plane to the Zn plane. The wurtzite unit cell is described by the lattice parameters a and c which have a ratio of $c/a = \sqrt{8/3} = 1.633$ for the ideal cell. The literature values for the lattice parameters in ZnO range from 3.2475 Å to 3.2501 Å for the a parameter and from 5.2042 Å to 5.2075 Å for c. The resulting c/a ratios are around 1.6. The bond length between Zn and O is about u = 0.382 times the lattice parameter c [22, 24].

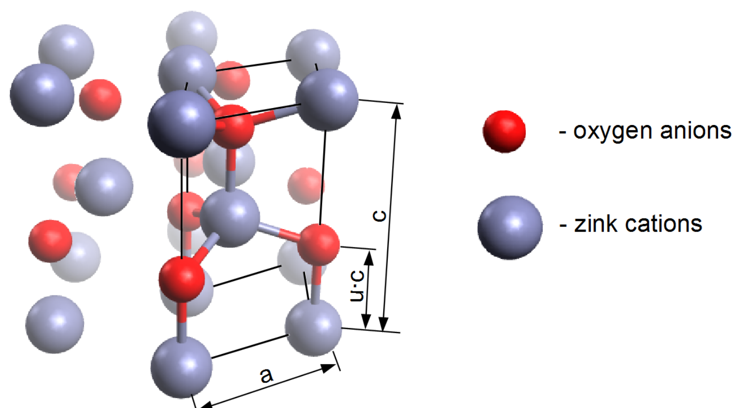

Figure 2.1: Wurtzite structure of ZnO with unit cell, tertraeder bonds and lattice parameters.

2 Fundamentals

2.1 ZnO

ZnO is a II-VI compound semiconductor with a direct bandgap of $\sim$3.37 eV at 300 K [5, 22, 23]. Under ambient conditions, ZnO forms the hexagonal wurtzite structure, which is depicted in Fig. 2.1. The Zn cations and O anions in the wurtzite structure are arranged in tetrahedrons where one species of atoms is surrounded by the other and vice versa. This structure shows crystallographic polarity and piezoelectricity because it does not posses an inversion symmetry. By convention, the [0001] axis is the positive z-direction and points from the O terminated plane to the Zn plane. The wurtzite unit cell is described by the lattice parameters a and c which have a ratio of $c/a = \sqrt{8/3} = 1.633$ for the ideal cell. The literature values for the lattice parameters in ZnO range from 3.2475 Å to 3.2501 Å for the a parameter and from 5.2042 Å to 5.2075 Å for c. The resulting c/a ratios are around 1.6. The bond length between Zn and O is about u = 0.382 times the lattice parameter c [22, 24].

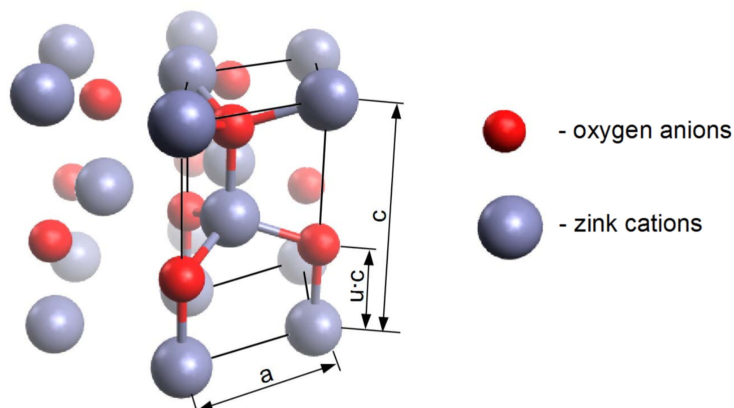

Figure 2.1: Wurtzite structure of ZnO with unit cell, tertraeder bonds and lattice parameters.

2.2 ZnO varistor ceramics

A varistor is a passive electronic device with a highly nonlinear current-voltage (I-V) behavior. The I-V characteristics can be described by a power law:

$$I = \left(\frac{V}{C}\right)^{\alpha} \tag{2.1}$$

where I is the current through the device, V the applied voltage, C a constant, and α the nonlinearity exponent. A value of $\alpha = 1$ would result in an Ohmic resistor and $\alpha = \infty$ would result in an ideal varistor.

Fig. 2.2 shows the I-V behavior of a MLV device with a small number of GBs between the electrodes. The switching voltage at ~3 V, the leakage region below switching, and the breakdown region at higher voltages are marked. The highly nonlinear effect in varistor ceramics is caused by the formation of electrical barriers at the ZnO grain boundaries. The nature of these barriers is described in section 2.2.2. The formation of these barriers is triggered by specific dopants. The two important ZnO varistor systems are distinguished by their main doping element, which are on the one hand Bismuth (Bi) doped systems and Praseodymium (Pr) doped systems on the other. The effects of these elements and other dopants which are important for technical varistor ceramics are described in section 2.2.3.

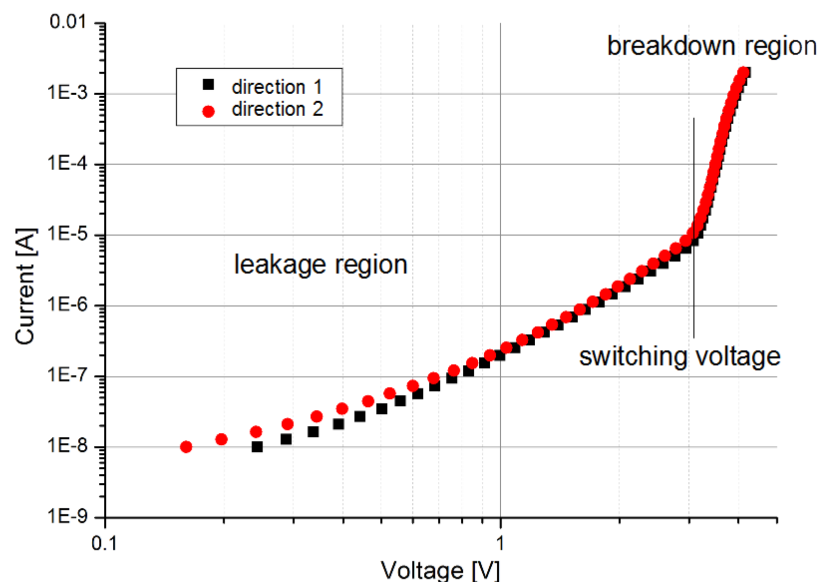

Figure 2.2: I-V curve of a MLV device; Note the switching voltage of ~3.3 V, the leakage and the breakdown region.

2.2.1 Manufacturing process of multilayer varistors

Technical multilayer varistor devices are manufactured in a tape casting and sintering process, similar to the production of other multilayer devices like multilayer capacitors and multilayer piezoactuators. The fabrication process is sketched in Fig. 2.3. The ZnO and the dopants are mixed as powders with a polymer binder in a slurry. This slurry is cast on a moving carrier film, and the so called green sheet is formed. The thickness of the slurry-film is controlled with a doctor blade system. After drying to stabilize the material, the green sheet is cut into several pieces and the internal electrodes are screen printed onto these pieces. Then the pieces are stacked, pressed and further cut (green chips). These parts are sintered in oxygen rich atmosphere. Finally, the termination caps are fired on the devices [25]. The internal electrodes and the termination caps are typically made of Ag/Pd alloys. An optical image of a MLV cross section is presented in Fig. 2.4. The inner electrodes and the terminal caps are clearly visible and marked in the image. This device features only one pair of inner electrodes in a distance of 20 μm, but devices with more electrode pairs are common.

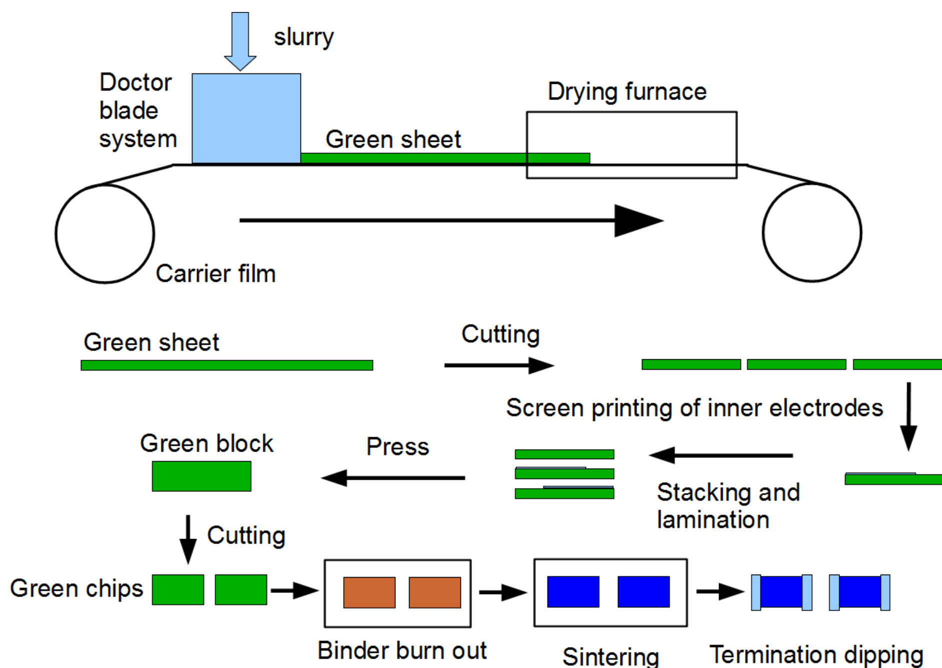

Figure 2.3: Scheme of the multilayer varistor production process after [1, 25].

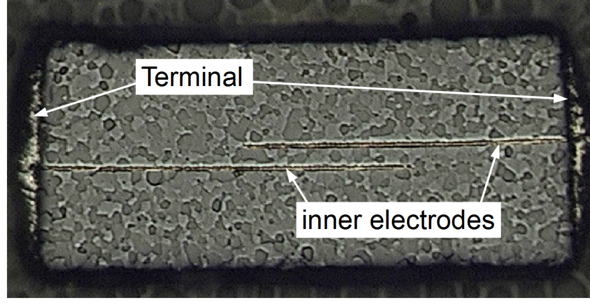

Figure 2.4: Optical micrograph of a cross sectioned and polished MLV specimen.

2.2.2 Grain boundary behavior

As already mentioned, the highly nonlinear current to voltage behavior, the varistor effect, is caused by the formation of electrostatic barriers at the grain boundaries.

In a simple model, as depicted in Fig. 2.5, the grain boundaries are assumed to consist of the same material as the grain interior, but contain defects and dopants. Therefore, the GB has a different Fermi level (E_{FGB}) and electronic states within the bandgap. To reach thermodynamic equilibrium, the electrons flow to the grain boundary and get trapped by the traps and dopants until the Fermi energy is equal in the whole material. The trapped electrons act as a negatively charged layer at the GB and leave positively charged donor sites at the sides of the GB. This process results in an electrostatic field and an electrostatic barrier Φ_B at the GB. The model ignores the discrete nature of the charges and allows therefore to calculate the magnitude of the potential barrier by solving the Poisson equation for the potential barrier, Φ(x), from knowing the grain boundary charge density ρ(x):

$$\frac{d^2}{dx^2}\Phi(x) = \frac{\rho(x)}{\varepsilon\varepsilon_0} \tag{2.2}$$

where ε is the relative permittivity and ε_0 is the vacuum permittivity.

The trapped charge in a boundary is a two dimensional layer of areal density n_t. Solving the Poisson equation results in the barrier height Φ_B and in the width d of the depletion layer by the following relations with n_0 as carrier concentration in the grains:

$$\Phi_B(V=0) = \frac{e^2 n_t^2}{8\varepsilon\varepsilon_0 n_0} = \frac{Q_i^2}{8\varepsilon\varepsilon_0 n_0} \tag{2.3}$$

$$d = \frac{Q_i}{2n_0} \approx \left(\frac{\varepsilon\Phi_B}{n_0}\right)^{1/2} \tag{2.4}$$

Applying a voltage across the GB changes the band structure and current flows. Simultaneously, additional electrons are trapped at the GB and a dynamic flow of trapped charges between the GB and the grains develops. Equation 2.5 describes the current density $j(V)$, depending on an applied voltage V as an thermionic emission process. A^* is the Richardson constant, T the absolute temperature, ε_ξ the Fermi level in the grains and k the Boltzmann constant [26].

$$j(V) = A^* T^2 e^{\frac{-e\Phi_B(V)+\varepsilon_\xi}{kT}} \left(1 - e^{\frac{-eV}{kT}}\right) \tag{2.5}$$

The height of the barrier depends on the applied bias and on the energy distribution of the interface states and can be approximated with a critical voltage V_C as:

$$\Phi_B(V) = \frac{V_C}{4}\left(1 - \frac{V}{V_C}\right)^{1/2}. \tag{2.6}$$

As can be seen in Equation 2.3, the barrier height decreases with increasing grain conductivity. Nevertheless the formation of the barrier requires a difference in Fermi level between the grains and the GB and therefore a certain grain conductivity to allow a filling of the traps at the GB. Since the grains and grain boundaries are in series, conductive grains are also required for the device functionality. Typical values for varistor ceramics are for the trap density $10^{13}\,\mathrm{cm}^{-2}$, for the conductivity $10^{17}\,\mathrm{cm}^{-3}$ and for the barrier height 0.8 eV. These values result in a depletion region width of ~0.1 µm, and an electric field close to the GB of ~1 MV/cm [2, 27, 28, 29].
Once a bias is applied hot electrons are formed in the high electric fields at the GB. Some of the electrons can cross the barrier and gain sufficient energy to produce minority carriers (holes) upon impact excitation of valence electrons and acceptor states within the depletion region as depicted in Fig. 2.5 c). The holes recombine with some of the electrons trapped at the barrier, thereby reducing the barrier height and emitting a photon. The reduced barrier yields an increase of the electron flow. This positive feedback causes the very large nonlinearity exponents of varistors [2].

2.2.3 Dopants in ZnO varistor ceramics

Dopants are crucial for the formation of ZnO based varistor materials. Dopants influence the grain growth and therefore the microstructure formation during sintering, the dewetting charactersistics of the liquid phase after cooling and the electronic defect states which determine the varistor characteristics [2]. The model described in chapter 2.2.2 shows clearly the need of two kinds of electrically active dopants, one to

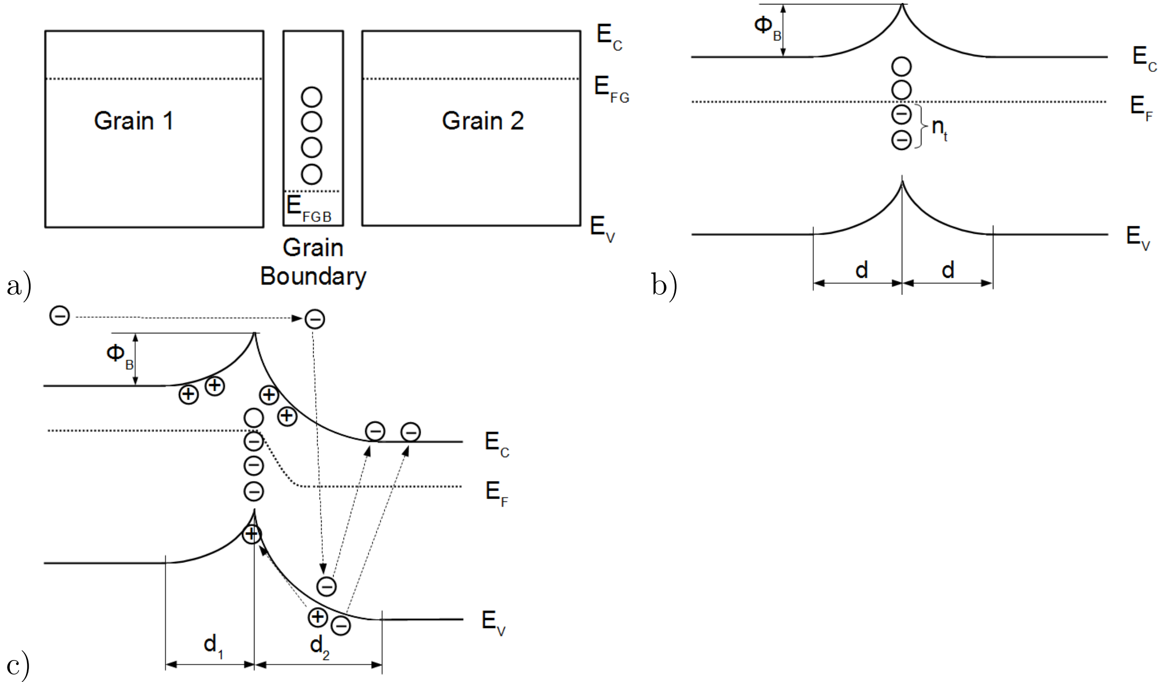

Figure 2.5: Grain boundary; a) thought experiment when not in contact; b) Barrier formation; c) Barrier with an applied voltage; Φ_B: Barrier height, E_V: Valence band energy, E_C: Conduction band energy, E_{FGB}: Fermi energy at the grain boundary, E_{FG}: Fermi energy of the ZnO grains, d: Depletion layer width, n_t: Trapped electrons; redrawn after [2].

control the grain conductivity and the other to influence the charge density at the grain boundary. The electric properties of ZnO are also influenced by the presence of intrinsic defects, which are oxygen vacancies (V_O) and zinc interstitials (Zn_i). These intrinsic defects can already form a potential barrier at the GBs; nevertheless, this barrier and the degree of nonlinearity are small. Oxygen at the GBs is also related to varistor behavior. Two groups of ZnO based varistor materials are commercially applied. These are systems containing bismuth oxide (Bi_2O_3) and systems with praseodymium oxide (Pr_6O_{11}) as main additive to form an insulation between the ZnO grains. Scanning electron microscopy micrographs of commercial varistor devices are presented in Fig. 2.6. The first developed ZnO varistors from M. Matsuoka were of the bismuth oxide type [2]. In Fig. 2.6 a) the scanning electron microscope micrograph of a polished and etched Bi system ZnO varistor sample is shown. The Bi-system forms a Bi rich grain boundary phase and spinel exclusions which are indicated in the image [31]. Also the formation of twins is increased in this system. ZnO varistors with praseodymium were first reported by K. Mukae in 1977 [2, 4]. Already a layer of few praseodymium atoms at the GB can

lead to varistor behavior [24]. The Pr systems form a uniform microstructure without pronounced additional phases or twinning, as can be seen in Fig. 2.6 b). Varistors containing Pr_6O_{11} show a higher capability to withstand electrostatic discharges whereas those with Bi_2O_3 better handle constant surges [25]. The fabrication of varistor devices with highly non-ohmic behavior requires further dopants or additives.

Other dopants are transition elements like cobalt and manganese which go into solution in the ZnO and increase the achievable α exponent by the formation of interface states and deep bulk traps. Aluminum increases the grain conductivity as it acts as a donor in ZnO. Antimony and silicon are grain growth inhibitors in Bi systems through the formation of spinel and pyrochlore phases [5]. Antimony further improves the I-V characteristics and the stability against electrical stress. Sb also promotes the formation of twins in the ZnO grains which are unit cell thick layers of the n-type semiconductor zinc antimonate spinel ($Zn_7Sb_2O_{12}$). On the other hand, TiO_2 and BeO promote the grain growth. Additionally, dopants which mainly control the grain growth also affect the potential barrier formation at the GB [2, 3].

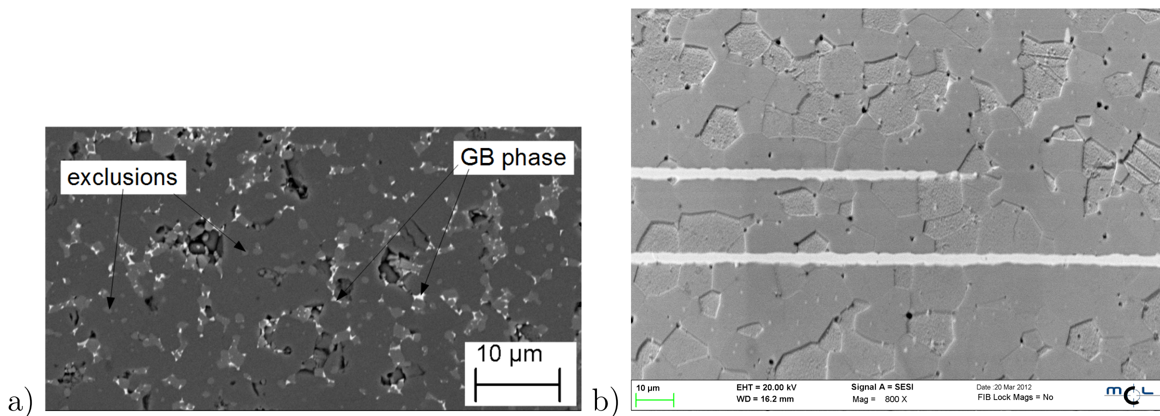

Figure 2.6: Scanning electron microscopy images of ZnO varistors; a) Bismuth system (image taken at the ESI); b) Praseodymium system (image taken at the MCL).

2.3 Atomic force microscopy

Atomic force microscopy (AFM) is a surface analysis method in which a sharp tip on a flexible cantilever is scanned across the surface under investigation. The sample and/or the probe is moved with piezoelectric actuators. A laser beam is reflected from the backside of the cantilever onto a segmented photo diode. The signal from this photo diode is used as input for a feedback loop. The feedback loop is adjusting the elongation of the z-actuator and therefore the distance between the cantilever and the sample surface. From the z-piezo movement, the surface topography is directly determined. As two principal operation modes in AFM the contact mode and the AC mode, which are explained below, have to be distinguished [9, 32].

Contact mode AFM

In contact mode AFM, the tip is constantly pressed on the surface with a certain force. The force causes a deflection of the cantilever. This deflection is detected by the laser and the photo-diode and held constant by the feedback loop. Due to the constant mechanical interaction between tip and sample surface the tip is subject to increased wear and deformation. Soft surfaces may also be influenced by the scanning tip. Nevertheless, several scanning techniques require a scanning in contact mode.

Intermittent contact mode or AC mode AFM

In intermittent contact mode the cantilever is excited to oscillations close to its resonance frequency by a piezoelectric actuator which is acting on the cantilever holder. The oscillation of the cantilever is damped when the tip approaches the sample surface and touches it. This damped amplitude is measured with the photo-diode and a lock in amplifier. Here, the amplitude is used as signal for the height feedback. AC mode is a denotation from Asylum Research company for the intermittent contact mode.

2.3.1 Conductive atomic force microscopy

The principle of conductive atomic force microscopy (C-AFM) is illustrated in Fig. 2.7. In C-AFM, a potential is applied between a conductive AFM tip and the sample. The current through the tip and sample is measured with a current-to-voltage converter. Applying a constant voltage between tip and sample allows the simultaneous and independent acquisition of the surface topography and a two dimensional current image [10].

The electrical properties of single spots can be investigated by keeping the AFM-tip on a certain position and applying a voltage ramp to measure a local current-voltage (I - V) curve. Since C-AFM requires a constant electrical contact between the AFM tip and the specimen surface, electrically conductive AFM probes and scanning in contact mode are necessary.

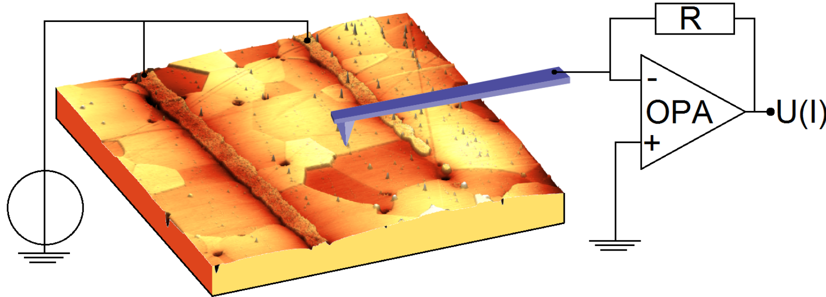

Figure 2.7: Scheme of the conductive AFM setup with an MLV specimen (topography map).

2.3.2 Kelvin probe force microscopy and scanning surface potential microscopy

Kelvin probe force microscopy (KPFM) is a method to map the local contact potential difference (CPD) [12]. The CPD is the difference in work function between two materials. The physical principle of the CPD between two materials is illustrated in Fig. 2.8. One material is considered as that of the tip with the Fermi energy E_{F_Tip} and the work function ϕ_{Tip} the other one represents that of the sample with the Fermi energy E_{F_S} and the work function ϕ_S. E_{Vac} is the local vacuum energy level. In the first image the two materials are in distance without any interaction. In contact (second scheme) the Fermi energies E_{F_Tip} and E_{F_S} align by charge transfer and the local vacuum energy E_{Vac} is shifted by the potential V_{CPD}. Due to the charge transfer an electrostatic filed is established between the two materials which also causes an electrostatic force. In the third image a voltage with the value of the CPD is applied between tip and sample. This compensates the electrostatic field and therefore also the electrostatic force.

This principle is used in KPFM for the measurement of the local contact potential difference between the conductive AFM tip and the sample surface [12]. A scheme for the measurement is displayed in Fig. 2.9. KPFM and SSPM require electrically

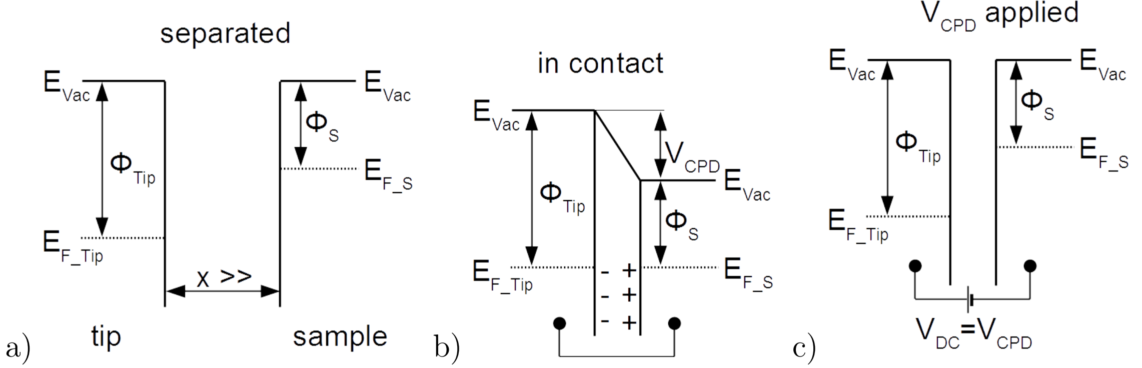

Figure 2.8: Scheme of the band structure of two different materials to explain the work function ϕ and the contact potential difference (CPD); a) separated materials; b) both materials in contact; c) with an applied bias.

conductive probes since a potential has to be applied to the tip. During the first pass the surface topography is measured in AC mode. In the second pass the tip follows the surface topography in close proximity ($\sim 5\,\text{nm}$). During this second pass, an AC and a DC voltage is applied between tip and sample. This electric field excites the cantilever to oscillations via a force as is described in equation 2.7.

$$F = \frac{1}{2}\frac{dC}{dz}\left((V_{DC} - \Delta\Phi)^2 + 2(V_{DC} - \Delta\Phi)V_{AC} * cos(\omega t) + \frac{1}{2}V_{AC}^2 * cos(2\omega t)\right) \tag{2.7}$$

where V_{AC} is the AC voltage with a frequency close to the resonance frequency of the cantilever, V_{DC} is the externally applied DC voltage to suppress the cantilever oscillation, $\Delta\Phi$ is the CPD, and ω is the circular frequency of the cantilever oscillation.

In the second term of equation 2.7 it can be recognized that the first harmonic component of the electrostatic force, and therefore the oscillation of the cantilever, is nullified if the applied DC bias, V_{DC}, is equal to the CPD. A feedback loop adjusts the DC bias constantly to suppress the first order of cantilever oscillations and the DC voltage is recorded as the CPD signal [12, 13]. The CPD is mainly the difference in work-function between the tip and the sample material, but is also influenced by factors like the presence of a water film and the local surface roughness.

Scanning surface potential microscopy (SSPM) is a variant of KPFM where an additional bias is applied across the specimen. Measuring KPFM on a such biased sample results

in a map of the potential distribution on the surface plus the CPD. From the measured surface potential distribution, DC transport properties can be derived [33].

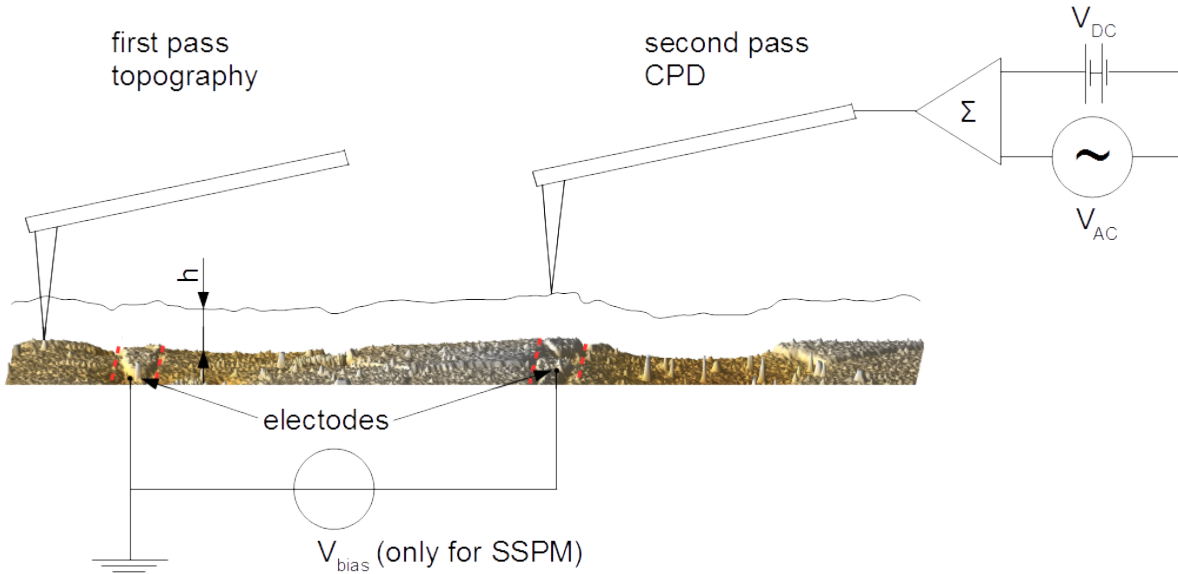

Figure 2.9: Scheme for the Kelvin probe force microscopy (KPFM) and scanning surface potential microscopy (SSPM) measurement setup. Indicated are the two scan passes and a scheme of the electrical circuit.

2.3.3 Scanning impedance microscopy

Scanning impedance microscopy (SIM) is a method similar to SSPM since it is also a two pass technique and voltages are applied to the AFM probe and across the sample as illustrated in Fig. 2.10 [16, 17]. SIM also requires conductive or with a conductive material coated AFM probes. Like in KPFM and SSPM the surface topography is mapped in the first pass of a scan-line. The main difference is that in SSPM a DC bias is applied across the sample and an AC + DC voltage is applied to the probe, whereas in SIM an AC + DC bias is applied across the specimen and a DC voltage to the AFM probe. The DC voltage at the probe is used to increase the electrostatic interaction between tip and sample and therefore the contrast of the image. In the second pass, the cantilever is excited to oscillations by the field between tip and sample surface with a force similar to the one described in Eq. 2.7. The amplitude of these oscillations is measured with a lock-in amplifier and allows to calculate the local AC voltage at

the sample surface. A set of measurements at different excitation frequencies allows to calculate local AC transport parameters [18, 33].

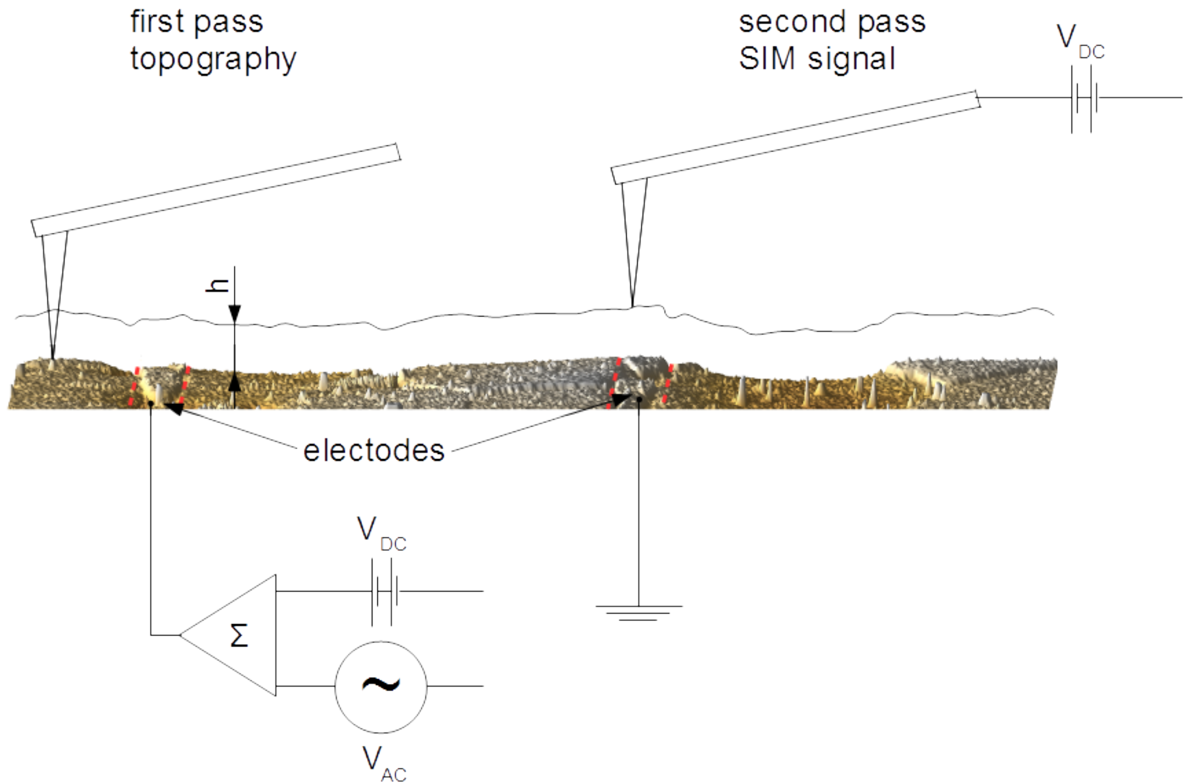

Figure 2.10: Scheme of the scanning impedance microscopy measurement setup. Indicated are two scan passes and a scheme of the electrical circuit.

2.4 Four-point probe

The measurement of resistances in a two-point setup is always influenced by the resistances of the cables and contact properties between the sample and the probe. Since semiconductor surfaces are forming Schottky barriers between a metallic probe and sample surface, they are strongly influencing the measured resistance [34]. A four-point measurement setup (see Fig. 2.11) can overcome these limitations by separating the measurement of current and potential. In four-point measurements, a voltage is applied and the current is measured, or a known current is applied between two probes and the voltage drop is measured current free between the two other probes. The current free

measurement makes the potential measurement independent of contact properties and cable resistances.

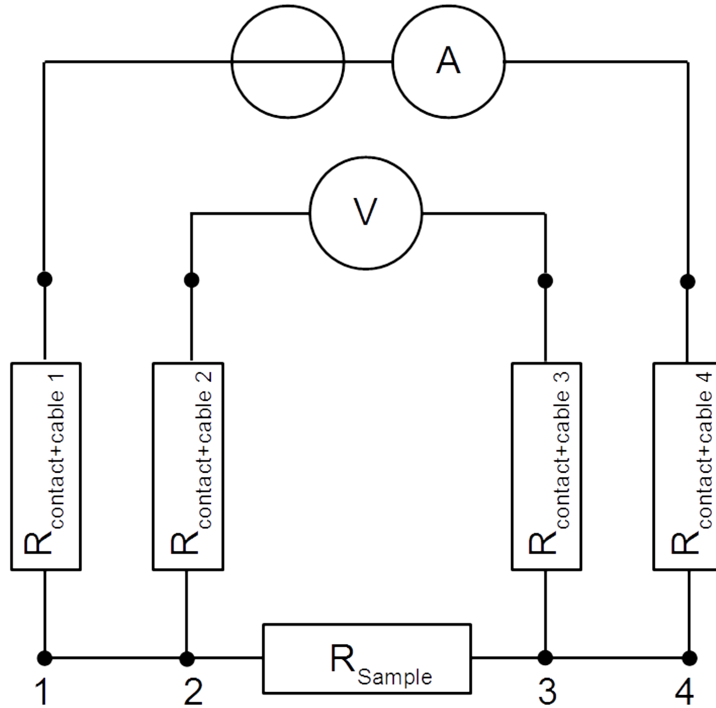

Figure 2.11: Scheme of a four-point probe measurement circuit, R_{Sample} is the resistance under investigation, $R_{contact+cable}$ are the cable and contact resistances.

Conventional four-point measurement setups use four independent macroscopic probes which are separately placed on the sample surface. This requires to manipulate four probes and a certain available area on the sample. A micro four-point probe, which is described in Sec. 3.4, allows to place all four probes at once on a limited space in a well defined distance in the micrometer range.

2.5 Electron backscatter diffraction

Electron backscatter diffraction (EBSD) is implemented in scanning electron microscopes (SEM) to map the crystallographic orientations at the sample surface. The principle of the EBSD measurement is depicted in Fig 2.12. The electrons of the primary beam propagate into the sample material and are inelastically scattered. This forms a cone of diffusely scattered electrons which are scattered at the lattice planes in the specimen if

Bragg's law is fulfilled [35]. Due to the cone, the scattering lattice plane is hit from all directions by electrons and the escaping electrons form interference lines on a fluorescent screen [36] - the so called Kikuchi-pattern. These patterns contain the orientational information and are analyzed by a digital camera and EBSD software. Usually, the sample is tilted by 70 degrees to increase the intensity in the diffraction pattern, and the detector is aligned parallel to the sample surface [19].

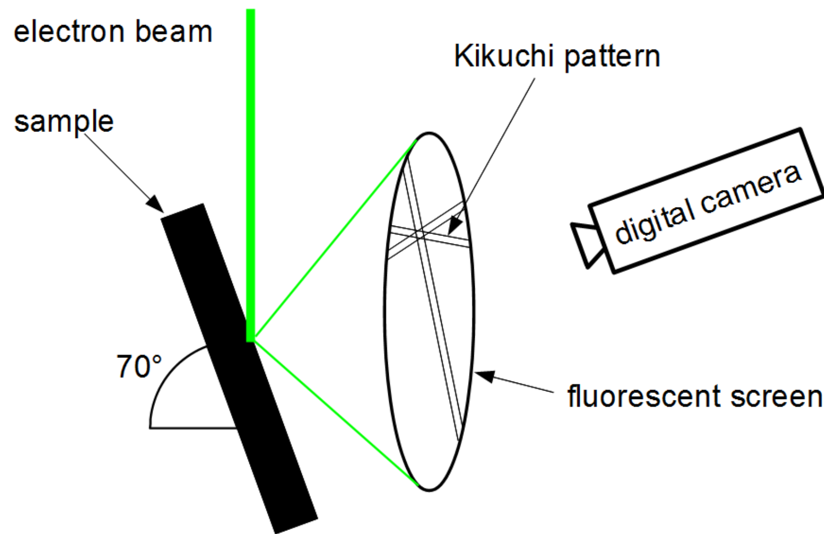

Figure 2.12: Scheme of an EBSD setup after [19].

2.6 Lock-in thermography

Lock-in thermography allows to detect local heat generation in a specimen. Applying a bias across a specimen causes a current flow and therefore the generation of Joule's heat. The resulting thermal radiation is measured with an infrared detector. To calculate the real temperature from the measured signal requires a calibration. A DC bias would cause a uniform temperature increase of the entire sample due to the thermal conductivity. Applying a sinusoidal bias allows to use a lock-in technique to determine local current paths. An offset of half of the bias amplitude generates a thermal signal with the same frequency as the applied bias, furthermore changing the direction of current flow through the sample allows the detection of direction dependent current paths. The amplitude of the thermal signal is proportional to the generated heat and therefore the local current flow. The phase-shift between the temperature and the applied bias allows to estimate the depth of the source of heat under the sample surface.

3 Experimental

3.1 Sample preparation

All multilayer varistor samples investigated here were produced by the EPC-TDK company, Deutschlandsberg, Styria. They were received either soldered onto printed circuit boards or as loose devices. The soldered samples allowed to apply voltages to the MLV electrodes with wires, also soldered onto the board. Theses samples were embedded in Struers Variofast, a transparent, two component cold embedding resin. Fig 3.1 shows such an embedded sample with the wires to the electrode. The loose specimens were thermally embedded in Struers Condufast, which is a mixture of a thermoplastic powder and a steel powder. This embedding in an electrically conductive substrate reduced charging effects and drift in EBSD mapping significantly but it did not offer the possibility to apply a voltage to the internal varistor electrodes. For the SIM investigations with a DI Multimode system, samples with a height lower than 5 mm were required. Therefore, loose samples were fixed with two component glue and two component conductive epoxy resin on a glass plate. The conductive epoxy was connected to the terminal caps of the samples and allowed to apply voltages across the varistor.

All samples were mechanically wet-ground with SiC sandpaper. The last grinding step is recommended to be done with 800 grit SiC paper. Polishing should be started with 9 µm diamond suspension and a perforated disk. The following polishing steps with 6 µm, 3 µm, 1 µm, and 0.25 µm can be done on smooth polishing disks. Each polishing step extends at least for five to eight minutes to securely remove all scratches. As final step, conventional or vibro-polishing with 100 nm SiO_2 suspension was employed. This final polishing step allows to distinguish individual ZnO grains due to their orientation depended abrasion behavior. Conventional polishing with SiO_2 has been done only half a minute for AFM images and about two minutes for optical microscopy investigations

as needed for M4PP. The vibro-polishing for the AFM images was done for 10 minutes without any load on the samples. All grinding and polishing have to be done as gentle as possible, since too much force will cause breakouts of the microstructure in the sample. The residuals from polishing have to be removed after every polishing step by thorough cleaning with a paper tissue under water. Finally the samples should be rinsed with distilled water.

The AFM specimen holder in Fig 3.1 on the right was manufactured from stainless steel to ensure a correct parallel alignment and stable fixation during AFM measurements. A similar holder was made for the M4PP investigations.

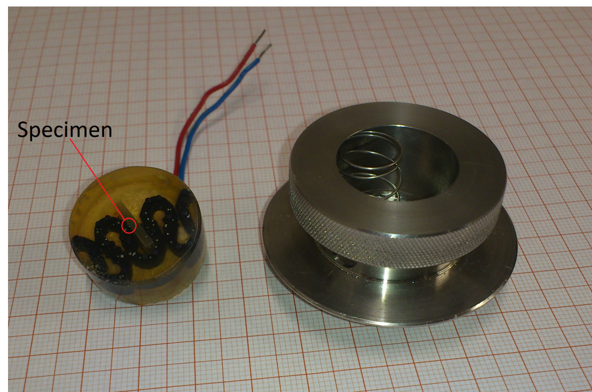

Figure 3.1: Specimen embedded in resin with the home-made AFM sample holder on the right.

3.2 Keithley 2636A dual source meter

All M4PP and some C-AFM measurements were performed employing a Keithley 2636A dual source meter. This instrument features two independent source and measuring units in one device. The parameters of the device are listed in Table 3.1.

Function	Capabilities
Source DC voltage	1 µV to 202 V
Source DC current	20 fA to 1.515 A
Measure DC current	1 µV to 204 V
Measure DC current	1 fA to 1.53 A

Table 3.1: Limits of the Keithley 2636A dual source meter [37];

For the M4PP measurements, both channels were employed. With the first channel a voltage was sweeped between the outer contacts and the current was measured. The second channel was connected to the inner contacts and set to work as current source. The applied current was set to zero and the voltage necessary to keep the current flow between the inner electrodes zero was measured. The M4PP measurements were performed employing the Java based software installed on the Keithley. Important setup parameters which have proven to work best are a measure and source delay of 50 ms and an integration time of 1 power line cycle (= 20 ms for a 50 Hz AC supply). To avoid errors which occur when the system changes the internal current detector range, a fixed current measurement range of 10 µA was chosen.

3.3 Atomic force microscopy

All presented C-AFM, KPFM and SSPM measurements were performed on Asylum Research MFP 3D systems. For the SIM measurements, performed at the Center of Nanomaterials Science at the Oak Ridge National Laboratory USA, a Bruker Multimode with Nanonis controlers was employed.

3.3.1 Conductive atomic force microscopy

The C-AFM images and most local I-V curves were measured employing the ORCA module from Asylum Research. The ORCA module is equipped with a current-to-voltage converter which is mounted in the vicinity of the cantilever holder to reduce noise and allows to apply up to 10 V bias and to measure a current in the range from 0.5 pA to 10 nA. Several I-V curves were measured with the Keithley 2636A (see section 3.2). All voltages were applied to the AFM probe and the sample was grounded.

As conductive probes for C-AFM, DCP11 from NT-MDT and 15Pt300 from Rocky Mountain Nanotechnology (RMN) were used. The DCP11 probes from NT-MDT are made of n-doped diamond coated silicon and feature a tip radius of 100 nm, a typical resonance frequency of 150 kHz and a spring constant of 5.5 N/m. The nanoroughness of the polycrystalline diamond coating enables a good lateral resolution despite the high tip radius, because usually only one diamond crystallite is in contact to the surface

[11]. These tips showed a good wear resistance and durability but the electrical contact properties are might suboptimal due to the small contact area to the surface and the semiconductor behavior. The probes from Rocky Mountain Nanotechnology are fully made of a platinum wire which is fixed on a ceramic chip. The RMN 15Pt300 probes have a tip radius below 20 nm, an average resonance frequency of 20 kHz and a spring constant of 18 N/m. Advantage of these probes is that they are fully metallic and even extensive abrasion and deformation will only increase the tip radius and not reduce the electrical conductivity. A further disadvantage is the about four times higher price compared to DCP11 and a broad resonance peak at low frequencies which makes an operation in AC mode more difficult.

Advantage of these probes is that they are fully metallic and even extensive abrasion and deformation will only increase the tip radius and not reduce the electrical conductivity, which is the main disadvantage of metallic coated probes.

3.3.2 Kelvin probe force microscopy, scanning surface potential microscopy

As probes for KPFM and SSPM conductive, TiN coated silicon probes, type NSG30 from NT-MDT, were used. These probes have a tip radius of 35 nm, a typical resonance frequency of 320 kHz and a average force constant of 40 N/m. A work function of about 5 eV was estimated for the TiN coated tips [38]. To apply the bias voltage to the MLV electrodes in SSPM measurements, one of the user programmable outputs of the Asylum research controller or the Keithley 2636A were used as DC source.

3.3.3 Scanning impedance microscopy

The SIM measurements were performed at the Center for Nanophase Materials Science (CNMS) at the Oak Ridge National Lab, USA within a granted proposal that has been submitted to the CNMS. For these measurements, a Bruker Multi-mode AFM with a Nanonis controler was employed. As cantilevers, Budget Sensors type *Electri*Multi 75 E-G with Cr/Pt coating were used. These probes feature a tip radius below 25 nm, a typical resonance frequency of 75 kHz and a force constant between 1 N/m and 7 N/m.

A Photograph of the setup is displayed in Fig. 3.2. As lock-in amplifier, a Stanford research SR844 with a lock-in range from 25 kHz to 200 MHz was employed. For SIM measurements a AC plus a DC voltage have to be applied to the sample. The AC voltage was provided by the internal frequency generator, the DC voltage was taken from a National Instruments board and both voltages were added by a summing amplifier. The current through the sample was measured with a current to voltage amplifier and read out by a National Instruments board.

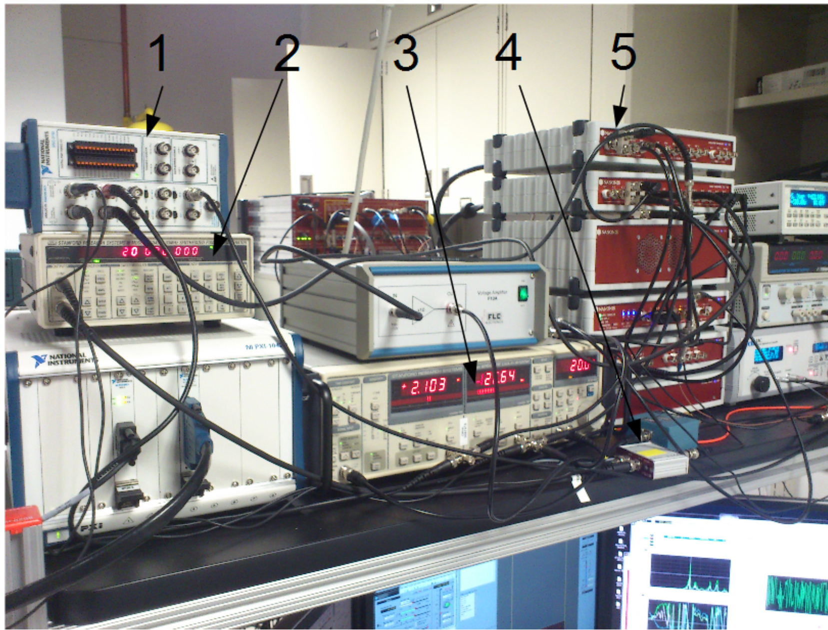

Figure 3.2: SIM setup at the CNMS; 1: DC source, 2: Frequency generator, 3: Lock-in amplifier, 4: Summing amplifier, 5: Nanonis AFM controler;

3.4 Micro four-point probe

Micro four-point probe (M4PP) allows to perform four-point probe investigations on micrometer sized structures with the probes placed in one row in close proximity. The setup for the M4PP measurements with the employed Keyence digital microscope and Kleindiek micromanipulator is shown in Fig. 3.3. All M4PP measurements were performed with probes from CAPRES which are displayed in Fig. 3.4. The probes are four flat, 25 µm long, 1 µthick and 3 µm wide, gold coated silicon cantilevers with a typical spring constant of 5 N/m. They are mounted on a silicon chip in a center to center distance of 5 µm [39]. These probes require a ZnO grain diameter of at least 8 µm

for investigations of the grain boundaries [40]. Fig 3.5 shows an exemplary ZnO grain boundary measurement in a) and a ZnO to electrode measurement in b) with a scheme of the electric circuit. The probes were placed in a way that the grain boundary under investigation was between the two inner probes. The outer probes were placed within the same grain as the corresponding inner probe. To measure the electrode-to-ZnO interface, the inner probe 3 was placed on the electrode and the neighboring outer probe was externally short circuited with the varistor electrodes.

Special attention has to be paid to the handling of the probes and their positioning on the sample surface. The procedure of probe mounting and approaching the surface is described in the following. Gloves have to be worn during all manual handling of the probes and the micromanipulator. A force of 2 N is the maximum allowable force acting on the bearings of the micromanipulator. To mount the probe holder in the micromanipulator, the probes are gripped with pliers on the ceramic part and the probe-holder is held with two fingers. Care has to be taken to not touch the wiring on the lower side of the probe-holder. The pliers are equipped with a heat-shrink tubing at the tips to avoid a damage of the ceramic pad. After mounting, the probes have to be horizontally aligned with the L-shaped metal part.

The probes have to be placed under the microscope on top of the sample surface. This requires a microscope with at least one centimeter working distance between the microscope lens and the sample. At first, the microscope should be focused on the desired sample area. The light-spot of the microscope helps also in the coarse positioning of the probes. Then, the probes are moved first with coarse and then with fine movements over the desired sample area. A movement with the telescopic arm causes a twist of the probe and might make an iterative process of positioning and horizontal alignment necessary. Approaching the probes to the sample surface requires attention and patience since no automatic feedback exists and the distance between probes and surface has to be estimated from the optical image. When the probes are close to the sample surface, diffraction fringes appear at the ends of the probes. Finally, the probes should bend slightly to ensure a stable electrical contact. A relay allows to change the connections between probe 1 and 3. This allows to apply voltages between neighboring electrodes to check the contact properties between probe and sample surface without current flow across the investigated GB.

A home built interface box was used as link between the CAPRES system and the Keithley connectors. The connection between the Keithley and the box was realized with home-made triax-to-coax cables.

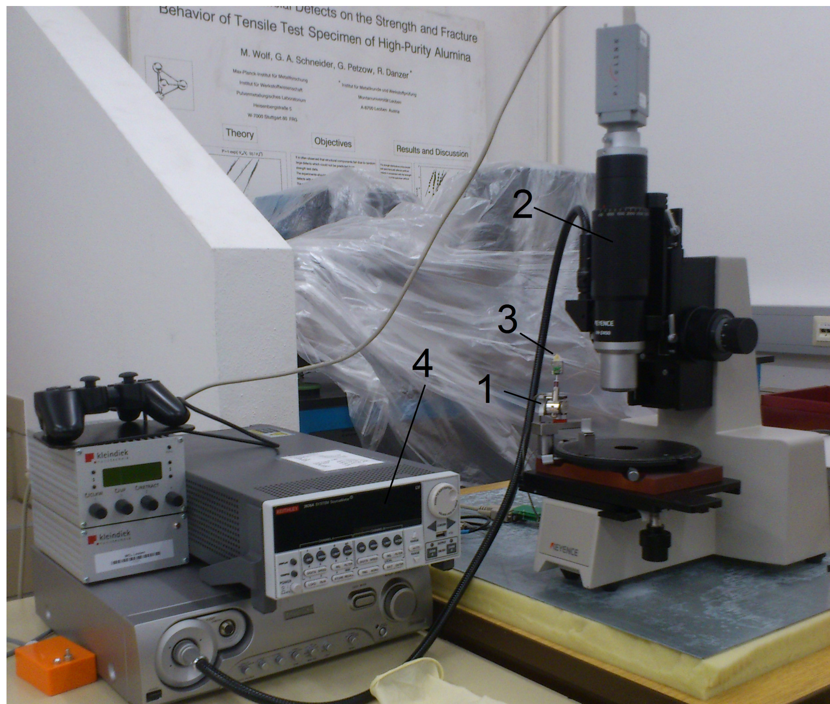

Figure 3.3: M4PP setup; 1: Kleindiek micromanipulator, 2: Keyence digital microscope, 3: CAPRES four-point probes, 4: Keithley 2636A dual source meter;

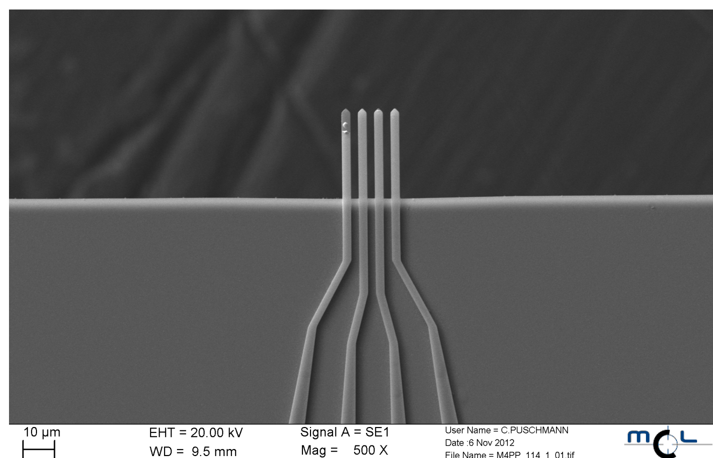

Figure 3.4: Scanning electron microscope image of a used micro four-point probe.

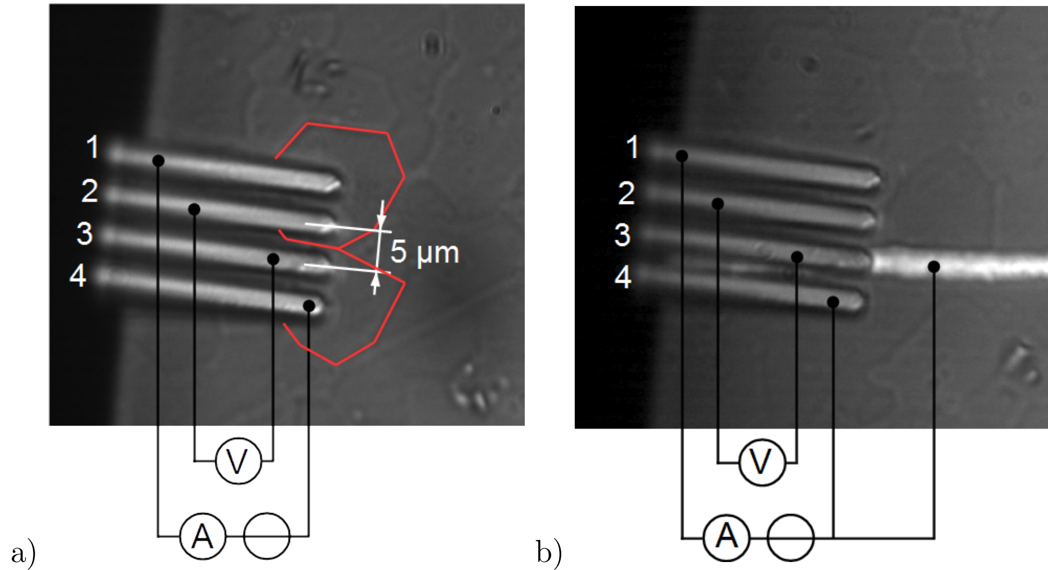

Figure 3.5: M4PP probes; a) setup for the measurement of ZnO grain boundaries; b) setup for the measurement of the ZnO - MLV electrode interface

3.5 Electron backscatter diffraction

The EBSD measurements were done on a Zeiss Auriga system at the MCL and a LEO 1525 system at the ESI. Both systems were equipped with an EDAX EBSD detector.

The electron beam in a scanning electron microscope causes a deposition of carbon on the sample surface. This carbon forms a conductive layer on the surface which spoils all electrical measurements like C-AFM and M4PP and also surface workfunction sensitive techniques like KPFM and SSPM. Therefore, EBSD has to be employed as last technique, after all AFM and M4PP measurements are finished. A gentle polishing after EBSD can be done to removes the carbon layer, but also some of the sample surface material is removed which might change the appearance of the grains at the surface.

Most of the presented samples were embedded in a non-conductive resin. The large volume of the resin cylinder gets electrostatically charged and is heated up under the electron beam of the SEM. The electrostatic charge causes a deflection of the electron beam and the temperature change causes thermal drift of the sample. These effects can strongly distort the measured orientation map. Therefore, the resin block has to be properly shielded with silver paint and copper tape to reduce these effects. As alternative

to the resin, a warm embedding in an electrically conductive powder was tried. This yielded very good results but was not applicable for all samples (see section 3.1).

3.6 Lock-in thermography

All lock-in thermography measurements were performed by M. Hofstätter at the Institut für Struktur- und Funktionskeramik, Leoben. For lock-in thermography a Cedip FLIR MW3 camera with an indium-antimony detector was used. The detector is sensitive to radiation from 3.6 µm - 5.1 µm wavelength. The camera resolution of 320 x 240 pixel in a distance of 30 µm results together with a six-fold magnifying lens system in an effective resolution of 5 µm x 5 µm per image pixel. The camera allows to capture up to 150 frames per second.

The analysis was performed with cross-sectioned samples on printed circuit boards, prepared as described in section 3.1. The applied voltages were in a range that only a few grain boundaries shifted to the conductive state and preferred current paths in the sample were formed. An iterative process of grinding and thermography imaging allowed to produce cross sections of the preferred current path. Several careful grinding steps are necessary because the phase imaging in lock-in thermography allows only an estimation of the depth of the heat source under the sample surface. The lock-in frequency has to be chosen high enough to reduce the temperature increase of the entire sample and sufficiently low to allow a reliable measurement with the camera.

4 Results

Here, results from investigations on Praseodymium and Bismuth doped samples are presented. The Praseodymium system was investigated with AFM based techniques and the M4PP. On the Bismuth system only AFM investigations were made.

4.1 Praseodymium system, AFM based investigations

As AFM based techniques conductive atomic force microscopy (C-AFM), Kelvin probe force microscopy (KPFM), scanning surface potential microscopy (SSPM), and scanning impedance microscopy (SIM) were employed. Sets of samples with 5 µm and 8 µm average grain diameter were used.

4.1.1 C-AFM investigations

Aim of the C-AFM investigations was to measure the local electrical properties via areal current scans with applied constant voltages and additional local I-V curves.

The C-AFM scan in Fig. 4.1 a) is an example for a measurement on a 5 µm grain size sample with an applied voltage of +8 V. The electrodes and individual grains are clearly visible. The electrodes are the vertical bright stripes. The ZnO grains appear as areas with constant current signal, whereas the grains close to the electrodes show the highest current signal and the current level drops at the grain boundaries with distance to the electrodes. For the first row of grains next to the electrode, currents up to the limit of the amplifier of 10 nA were measured. However to improve the visibility of the other grains, the color scale was set from 0 nA to 1 nA. The drops at the GBs confirm the high conductivity of the grain interior and the high resistivity at the grain boundaries.

The C-AFM scans on Pr-system samples exhibited no non-conductive other phases in the microstructure as expected for this system.

The I-V curve presented in Fig. 4.1 b) was measured at the grain marked by a green X in the current image and the EBSD map. This curve is similar to others measured at the first row of ZnO grains next to the electrode. It shows an asymmetric, non linear behavior for positive and negative applied voltages. The breakdown voltage for applied positive voltages is nearly 10 V and −5 V for negative voltages. Consecutive measurements of I-V curves at the same point yielded deviating breakdown characteristics and runaway values. This indicates uncontrollable electrical changes and unstable mechanical contact properties during the measurements. A general problem in all C-AFM measurements was the non Ohmic contact resistance between the AFM tip and the sample [34]. The EBSD measurement in Fig. 4.1 c) was performed to illustrate the individual ZnO grains. The electrodes can be recognized as black stripes in the EBSD map.

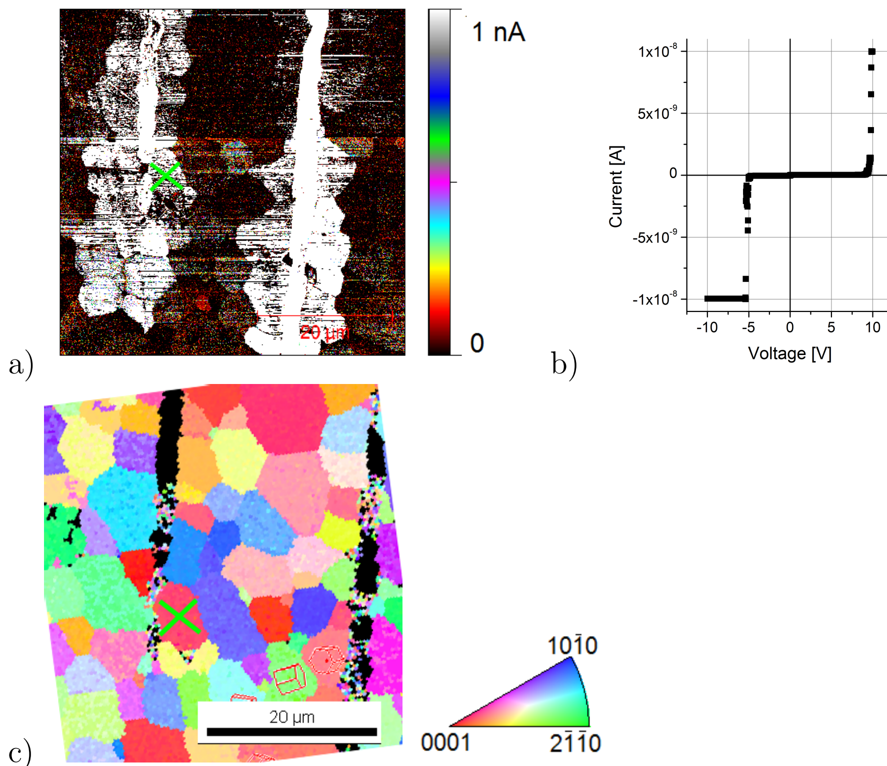

Figure 4.1: Polished MLV cross section of a sample with 5 µm grain size, a) C-AFM current image measured at 8 V, The maximum current at the electrodes is 10 nA, but to increase the visibility of the ZnO grains the maximum of the color scale was set to 1 nA; b)I-V curve, measured at the grain marked with X. c) EBSD image of the center area.

Wedge

In a normal cross section, the current is flowing from the AFM tip on top of the ZnO grain to the metallic electrode which is on the side of the grain. Since the crystallographic orientation is might influencing the electrical properties, a setup is required where only one crystallographic orientation is contributing. Therefore, a structure was realized where the ZnO is on top of the conductive electrode and the current goes straight through the ZnO.

The 5 µm grain size sample, presented in Fig. 4.2, was prepared in a way that the cross sectioning by grinding and polishing was made parallel to the MLV electrode plane. This resulted a single grain thin wedge of ZnO ceramic material with one of the electrodes underneath. The individual grains are clearly visible in the height image in Fig. 4.2 a). The current image (Fig. 4.2 b)) was measured at a bias of +8 V. Several areas in the image appear as stripes where no current was measured. The conductive and non conductive areas cannot be correlated with the topographic features in the height image. This effect might have been caused by an additional layer of ZnO grains underneath or by a very thin film of residuals from polishing on the sample surface.

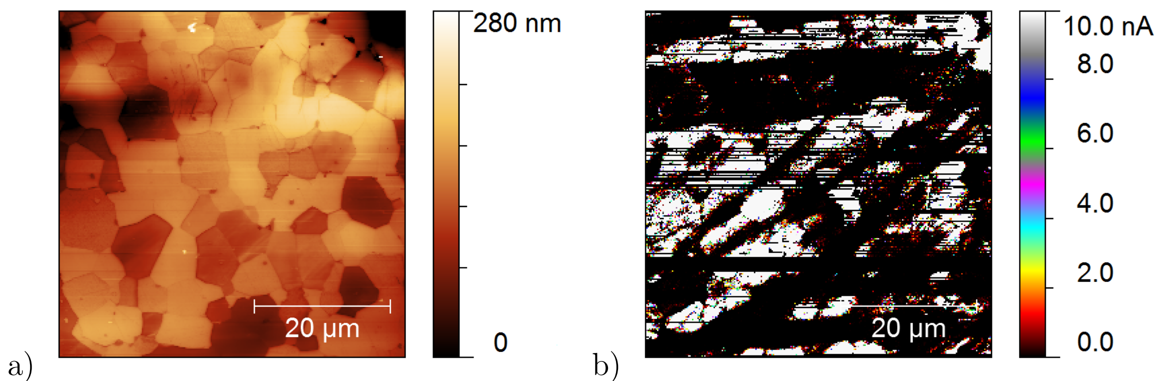

Figure 4.2: Polished MLV cross section parallel to the electrode plane; a) Height image; b) C-AFM current image measured at +8 V.

Long time test

To determine a change in the electrical properties of prepared sample surfaces over time, a set of grains on one polished sample was chosen. I-V curve measurements on these grains were repeated for four days. Fig. 4.3 shows a current map of the investigated area

in a) and the curves for the spot marked with X recorded at four subsequent days in b). The measured curves showed no significant changes after the period of four days. The observed changes in the curves can not be related to the time period.

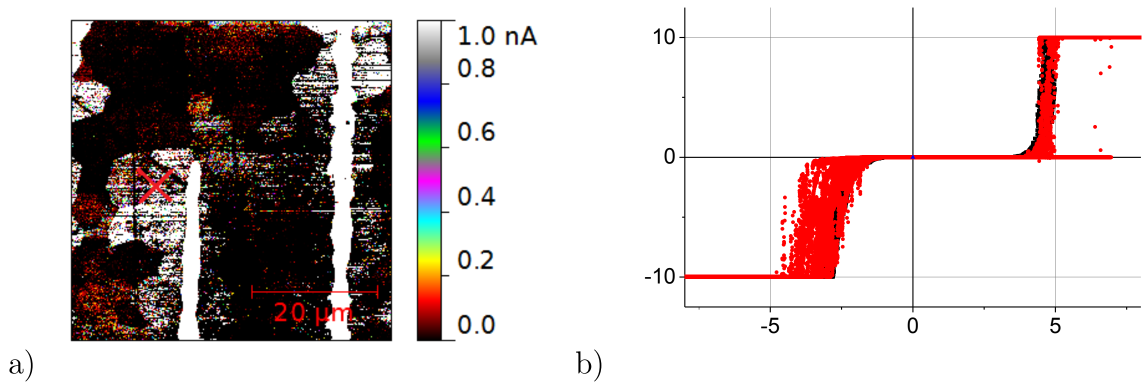

Figure 4.3: CAFM images of an 5 µm grain size specimen for long time test; a) current image at 5 V; b) I-V curve, measurement point marked with X.

Platinum deposition by focused ion beam

The previously presented C-AFM investigations showed instable and asymmetric contact properties. The deposition of platinum structures was made as an approach to increase the contact stability and to achieve Ohmic contacts between the AFM tip and the ZnO surface. The SEM image of a MLV cross section with deposited Pt pads is shown in Fig. 4.4 a). The Pt was deposited with a focused ion beam system by cracking a metallorganic gas under the ion beam. The system allowed a precise positioning of the pads within chosen ZnO grains. Fig. 4.4 b) shows an AFM height image. The white rectangles along lines 1 and 2 represent successfully deposited Pt pads. Whereas the black rectangles on the lines 3 and 4 are holes which were burnt into the sample surface by the ion beam because of improper ion acceleration voltages and currents. From the cross sections in Fig. 4.4 c) and d), a height of the dots between 200 nm and 300 nm and a depth of the holes of about 250 nm can be seen. Drawback of the deposition via a focused ion beam method is the deposition of a thin carbon film on the specimen, as it happened after all scanning electron microscopy investigations. This makes the entire surface conductive and prohibits meaningful electrical measurements. Therefore this approach was not further pursued.

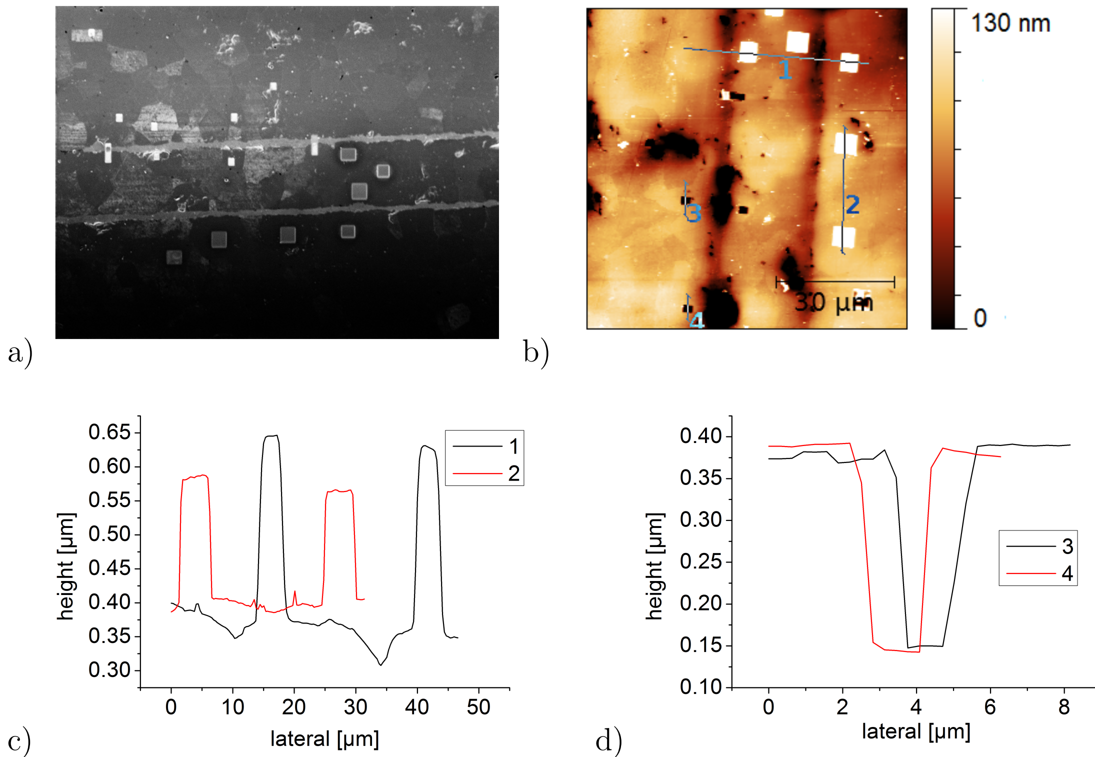

Figure 4.4: Image of an 8 µm grain size specimen with FIB deposited Pt-Dots; a) SEM image; b) AC-mode height image; c) cross sections 1 and 2 across Pt-Dots; d) cross sections 3 and 4 across pits

C-AFM measurements with the Keithley 2636A dual source meter

In the following, electrical measurements performed with the Keithley 2636A dual source meter will be reported. This device allows to apply and measure currents in a wider range than the original AFM current to voltage amplifier (Orca-Module) (see section 3.2). Moreover it enables measurements over longer timescales. The image in Fig. 4.5 a) shows a height image of a MLV specimen which was measured with a diamond coated DCP11 probe in AC mode to reduce wear of the tip and to prove the possibility of AC mode imaging with subsequent local electrical measurements. After the height imaging several I-V curves were measured by placing the tip on one spot and switching the system to contact mode. The diagram in Fig. 4.5 b) is a current-over-time plot with a constant voltage of 50 mV applied to the probe. Two curves were measured at one spot on an Ag/Pd electrode with two different deflection setpoints of 0.5 V and 5 V. The deflection setpoint determines the applied force between probe and sample. A setpoint of 0.5 V represents a usual value for contact mode measurements with the employed DCP11

probes, whereas a setpoint of 5 V is very high and would cause dramatic wear and damage of the tip and the sample if used for scanning.

The effective electrical contact area A_{eff} can be estimated as [32]:

$$A_{eff} = \pi r_{cont}^2, \tag{4.1}$$

$$r_{cont}^3 = \frac{3}{4}(k_1 + k_2) F_{ts} R_{tip}, \tag{4.2}$$

$$k_i = \frac{1 - \nu_i}{E_i}, \tag{4.3}$$

where r_{cont} is the effective contact radius, ν_i is the Poissons ratio and E_i the Youngs modulus for the tip material and the sample material respectively, F_{ts} is the force between tip and sample, R_{tip} is the effective tip radius.

Forming the ratio between two contact areas at different forces allows to cancel the material properties $k1$ and $k2$ and the radius of the AFM tip R_{tip} which leads to:

$$\frac{A_{eff}(F_{ts1})}{A_{eff}(F_{ts2})} = \left(\frac{F_{ts1}}{F_{ts2}}\right)^{2/3}. \tag{4.4}$$

Equation 4.4 states that an increase in force by a factor of 10 increases the effective contact area roughly five times. The experiment shows that an increase in force by ten times halves the measured resistance. This contradiction is caused by the high resistance of the probe and the nanocrystallinity of the diamond coated tip [11].

The measurement with a deflection setpoint of 0.5 V shows a noise in the range of 0.5 nA to 1 nA and fluctuations on a longer timescale of the average value of 2 nA. Also the curve measured with a high deflection setpoint shows noise and a decay of the measured signal over time. But, the stability of the measurement increases with a higher applied force.

It has to be noted that only a few tens atoms create the contact between the AFM tip and the sample surface. Therefore, these changes are contributed to a change in the atomic contact properties due to a temperature increase in the contact area and to thermal drift of the sample.

The third curve was measurement with a 10 MΩ resistor which was clamped in the AFM chip holder instead of the probe. The other contact was made with the triax to alligator clips cable which was also used for connection with the MLV specimen. This measurement was performed to test the electric noise inside the AFM box. Also, the piezoelectric actuators of the AFM were active during this measurement. The measured signal showed no noise caused by local electric fields which means an excellent shielding of the AFM and no influence of the AFM electronics on the measured signal.

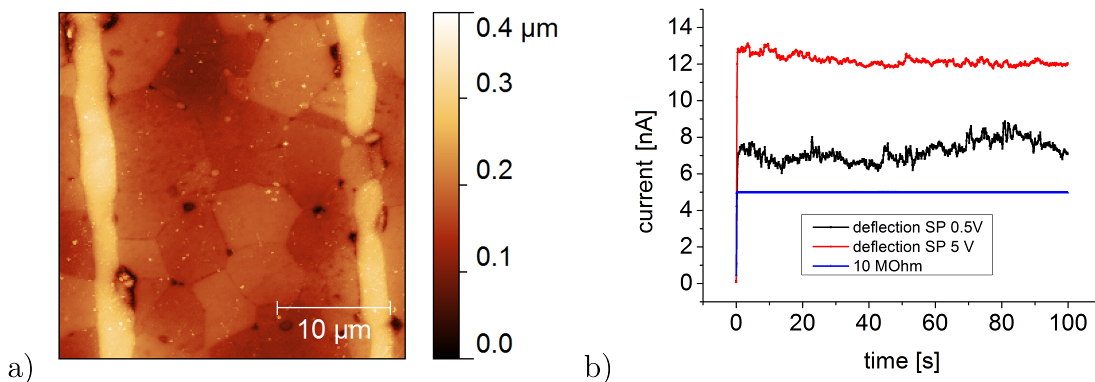

Figure 4.5: Polished MLV cross section; a) AC-mode height image; b) current over time plot at a constant voltage of 50 mV, measured on the electrode with the Keithley 2636A dual source meter.

4.1.2 KPFM and SSPM investigations

KPFM and SSPM investigation of an hot spot area

The macroscopic behavior of a set of low switching voltage MLV samples with a grain size of 8 µm and one pair of electrodes in a distance of 20 µm was investigated. From this set, a specimen with pronounced asymmetric macroscopic I-V characteristics was chosen for further investigation. The I-V curve of this sample is displayed in a double logarithmic plot in Fig. 4.6. FWD, which means forward direction and BWD, which means backward direction, are arbitrary notations for the direction of current flow. In

this measurement always a positive voltage was applied to one of the electrodes, the other one was grounded. To change the direction the electrodes were changed. The FWD and BWD curves do not deviate much in their switching voltage, but the current in the leakage region for the BWD curve is significantly higher. Assumption for this behavior was the formation of a preferred current path for one direction of the applied bias and therefore an asymmetric behavior. To detect this current path, an iterative process of grinding and subsequent lock-in thermography were employed. In lock-in thermography two hot spots, one for every bias direction, were found. Finally, one of the hot spots was located at the sample surface. One phase image of the thermography measurement with insets from the amplitude image is shown in Fig. 4.7. The white arrows in the image indicate the direction of current flow. Unfortunately, the hot spot on the left, for BWD direction, was lost for further investigation during polishing. The area of the right hot spot was further investigated with KPFM, SSPM, and EBSD [20, 41].

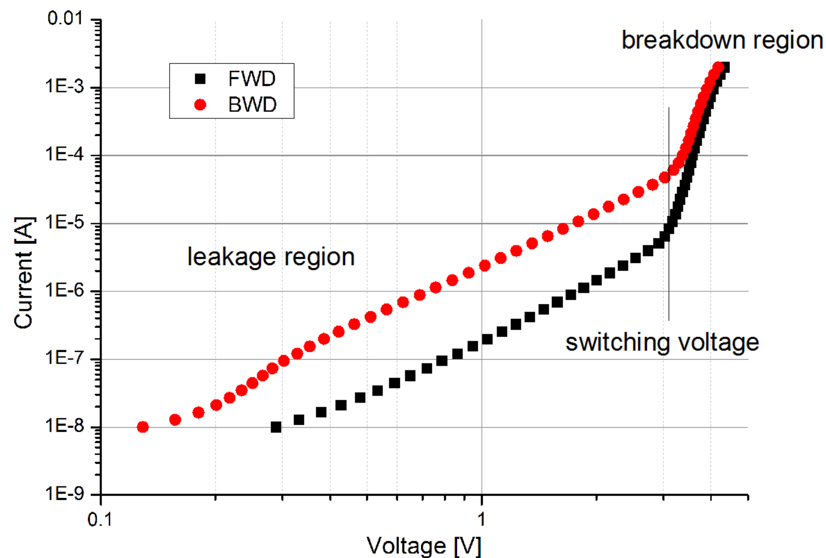

Figure 4.6: Macroscopic I-V curve of a MLV device with pronounced asymmetric behavior, measured at the ISFK; Note the switching voltage of ~3.3 V, the leakage and the breakdown region.

The results of the KPFM and EBSD investigations of the hot spot area can be seen in Fig. 4.8. The electrodes are visible as vertical stripes in all three images. The height image (Fig. 4.8 a)) reveals the individual ZnO grains which differ in their abrasion behavior during polishing. For the ZnO grains a height variation of about 20 nm and a lowering relative to the electrodes was found. The microstructure shows only the ZnO phase and some pores at the grain boundaries and triple junctions, as expected for a

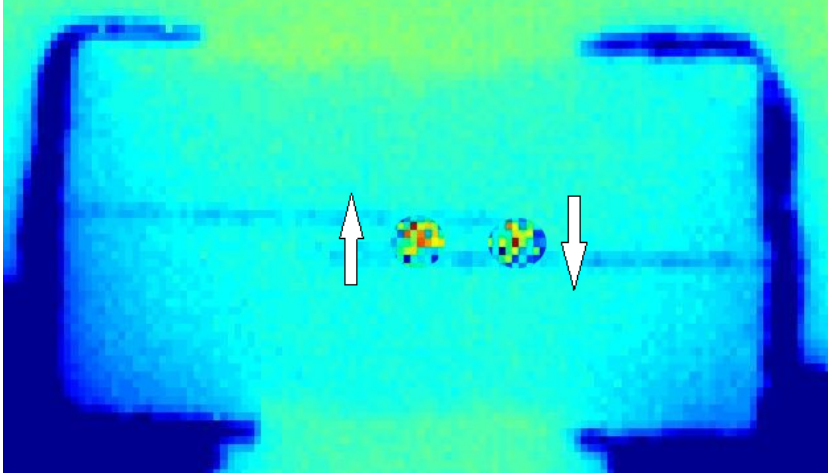

Figure 4.7: Thermography phase image of the sample with asymmetric behavior: The hot-spots are marked with insets from the amplitude image. Arrows indicate the current direction according to the corresponding hot spot.

Pr-system ZnO varistor ceramic. The individual ZnO grains differ also clearly in their work function which is shown in the CPD image (Fig. 4.8 b)). The difference in CPD is due to the different crystallographic orientation of the ZnO grains. An estimated workfunction of 5 eV [38]. for the TiN coated probe results in a workfunction of 4.6 eV for the Ag-Pd electrodes (Ag: 4.26 eV; Pd 5.4 eV) and between 4.85 eV and almost 5 eV for the ZnO grains. The investigated area was subsequently investigated with EBSD to reveal the crystallographic orientation of the individual grains (Fig. 4.8 c)).

The images in Fig. 4.9 a) and b) present an SSPM investigation of the same area as in Fig. 4.8. This sample features only one pair of electrodes, where the left electrode was grounded, to reduce the electrostatic influence of the applied voltage on the cantilever which is coming from the left side. The bias voltages of -1 V (in Fig. 4.9 a)) and $+1$ V (in Fig. 4.9 b)) were applied to the right electrode. The measured SSPM signal is the sum of the surface potential distribution and the CPD. The ZnO grains show across the entire grain an almost constant potential and the voltage changes occur mainly at the grain boundaries. This illustrates the much higher conductivity of the bulk material compared to the grain boundaries. The difference between the electrodes and the adjacent ZnO grains is contributed mainly by the CPD difference. As already reported by Hirose et al. [25], almost the entire voltage drops at the ZnO-ZnO grain boundaries (indicated by arrows) and only a small fraction appears at the ZnO-Ag/Pd electrode junctions.

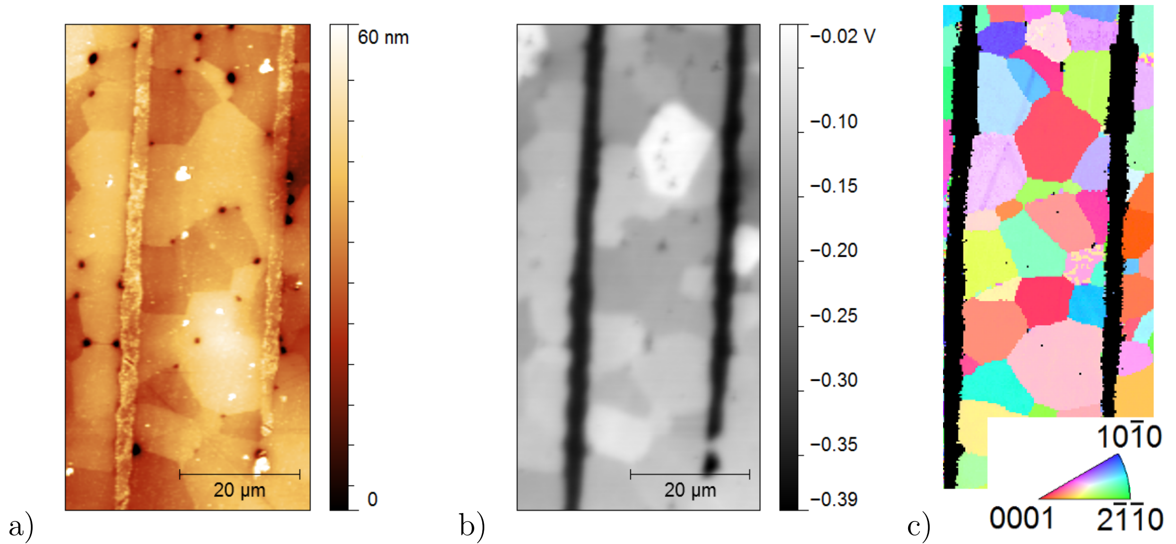

Figure 4.8: Polished MLV cross section of the hot spot area, a) AFM height image, b) CPD image, c) EBSD image.

In order to obtain quantitative data, it is worthwhile to analyze cross sections of the SSPM data. The potential profiles in Fig. 4.9 c) - f) are taken along the lines 1 - 4 in Figs. 4.9 a) and b). The lines 1 and 2 are taken in an area with only one ZnO-to-ZnO grain boundary between the electrodes. Both lines share the larger grain on the right side. The profiles with an applied voltage of −1 V (Fig. 4.9 c)) overlap besides a small difference caused by the different CPD. Remarkable are the curves with +1 V bias (Fig. 4.9 d)), which show a clear difference of 0.15 V in potential of the two left grains which can not be explained by the difference in CPD. This means that the barrier between ZnO and the electrode material becomes more pronounced. From this fact it is assumed that the ZnO-ZnO grain boundary along line 2 has a decreased resistance for one bias direction. This lowered resistance causes the formation of a preferred current path in one direction and therefore the hot spot.

The cross sections 3 and 4 in Fig. 4.9 e) and f) are taken in areas with two ZnO-ZnO grain boundaries between the electrodes. The overall voltage drop is again the externally applied bias of ±1 V. Whereas the individual drops or steps show different values. The voltage drops in cross section 3, (Fig. 4.9 e)), show a clear deviation for positive and negative applied bias. Remarkable is especially the left ZnO grain, adjacent to the grounded electrode, where the lines do not overlap. Cross section 4 (Fig. 4.9 f) is an example where the voltage drops show less asymmetry and the grain adjacent to the electrode has nearly the same potential for both applied biases. This means that -

even at current paths with more than one involved ZnO GB - pronounced asymmetric behavior can be found.

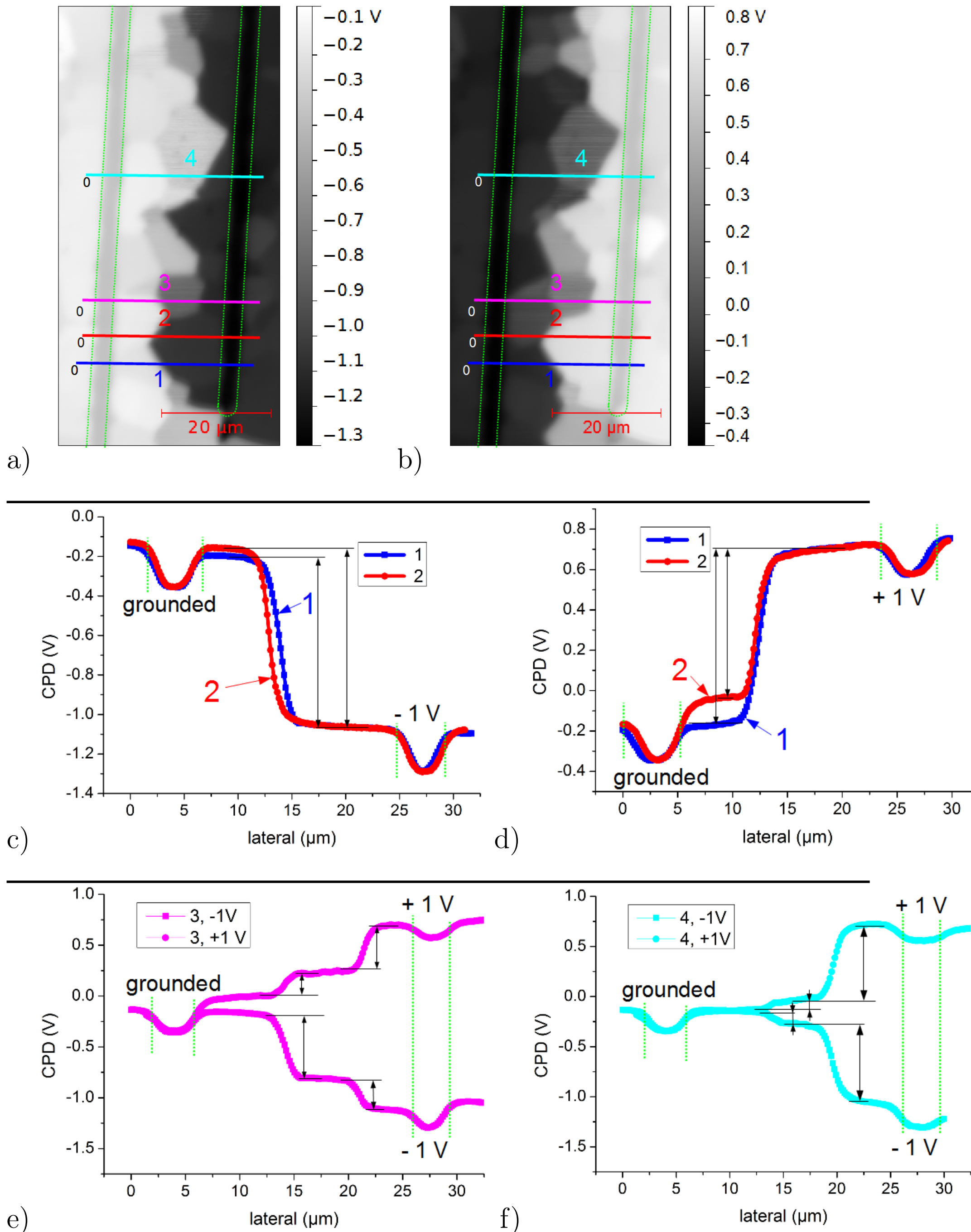

Figure 4.9: SSPM investigation of the hot spot area; a) SSPM image with −1 V bias applied; b) SSPM image with +1 V bias applied; c) cross sections at lines 1 and 2 at −1 V; d) cross sections at lines 1 and 2 at +1 V; e) cross sections at line 3, both directions; f) cross sections at line 4, both directions.

5 µm grain size sample

The sample presented in Fig. 4.10 is an example for a combined KPFM and SSPM investigation on a 5 µm grain size system. The height and CPD images are depicted in Fig. 4.10 a) and b). It was possible to apply a bias of 8 V between the MLV electrodes due to the smaller grain diameter without risking a damage of the sample. The resulting SSPM map is depicted in Fig. 4.10 c). A 3D graph was chosen to illustrate the typical terrace like potential levels.

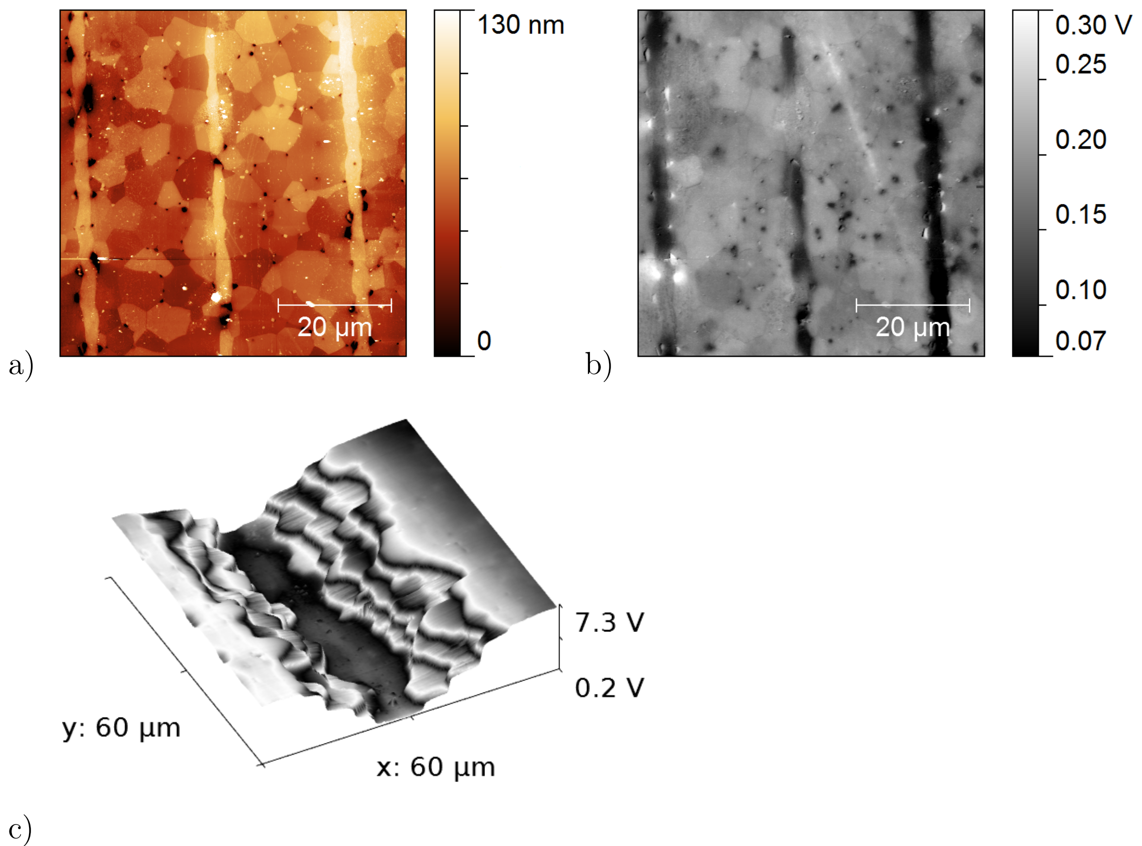

Figure 4.10: KPFM and SSPM study of a sample with 5 µm grain size; a) Height image; b) CPD map; 3D SSPM profile at + 8 V applied

4.1.3 SIM investigations

The aim of the scanning impedance microscopy (SIM) measurements was to obtain frequency dependent electrical properties of individual varistor grain boundaries. Such frequency dependent properties are the charging of the GB and thus the capacity, the movement of ions in the electric field, the width of the depletion layer, and the charge carrier mobility. Additional to the frequency dependence, varistor GBs show a highly non-linear current-voltage behavior which means that the conductivity is also depending on the magnitude of the applied voltage. The SIM measurements were performed during a stay at the Center for Nanophase Materials Science (CNMS), at the Oak Ridge National Lab (ORNL), Tennessee, USA. The model employed for analysis and data interpretation that has been tried to use here was proposed by S. Kalinin for SIM investigations of ferroelectric $BiFeO_3$ [33]. In this model every ZnO GB is assumed as a parallel circuit of a resistor (R_{GB}) and a capacitor (C_{GB}) as depicted in Fig. 4.11. The resistances of the grain interiors (R_{GI} and R_{GII}) are not included in the considerations due to their small contribution to the device behavior.

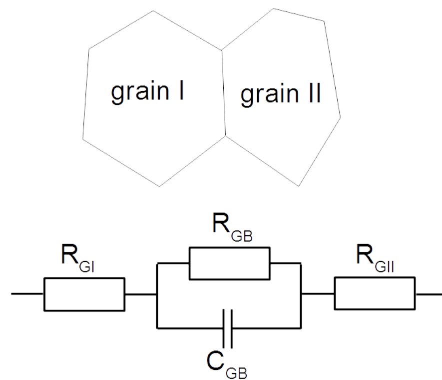

Figure 4.11: Equivalent circuit model of a grain boundary.

Equation 4.5 describes the impedance or complex resistance at the grain boundary between the two grains i and j:

$$Z_{GB\,i-j}(V_{DC},\omega) = \frac{1}{\frac{1}{R_{GB\,i-j}(V_{DC})} + i\omega C_{GB\,i-j}(V_{DC},\omega)} \tag{4.5}$$

where $Z_{GB\,i-j}(V_{DC},\omega$ is the impedance, $R_{GB\,i-j}(V_{DC})$ is the Ohmic resistance of the GB, $C_{GB\,i-j}(V_{DC},\omega)$ is the GB's capacitance and ω the frequency of the applied AC voltage.

The link between the SIM measurement and the grain boundary impedance is made in equation 4.6:

$$\frac{V_{ACloc\,i}}{V_{ACloc\,j}} = \left|\frac{Z_{right}}{Z_{left}}\right| \tag{4.6}$$

where $V_{ACloc\,i}$ and $V_{ACloc\,j}$ are the local AC voltages. Z_{left} is the summed impedance between the considered grain boundary and the left electrode, Z_{right} is the summed impedance between the considered grain boundary and the right electrode (see Fig. 4.13).

The values for $V_{ACloc\,i}$ can be calculated from measured values as described in equation 4.7:

$$V_{ACloc\,i}(V_{DC},\omega) = \frac{A_{loc\,i} * (V_{DCtip} - V_{DCref}) * V_{ACref}}{A_{ref} * V_{DCtip} - V_{DCloc}} \tag{4.7}$$

The value $A_{loc\,i}$ is the local amplitude at grain i, which was obtained by averaging the values within a defined rectangle inside every individual ZnO grain. V_{DCtip} is a voltage of 4 V which was constantly applied to the tip to increase the signal quality. V_{DCref} and V_{ACref} are the effective DC and AC voltage which were applied to the varistor device, according to table 4.1. A_{ref} is the reference amplitude at the biased MLV electrode and obtained by averaging the values within a defined rectangle inside the biased electrode. V_{DCloc} is the local DC voltage and was extrapolated from SSPM measurements at +1 V and −1 V performed at the same area (see Fig. 4.14).

To obtain results from a wide range of voltage levels and frequencies, a series of measurements with varying DC voltages and AC frequencies was performed. A compilation of all obtained SIM images is shown in Fig. 4.12. The externally applied DC voltages were varied between −12 V to +12 V. The AC voltage had an amplitude of 1 V and was applied with varying frequencies from 20 kHz to 200 kHz.

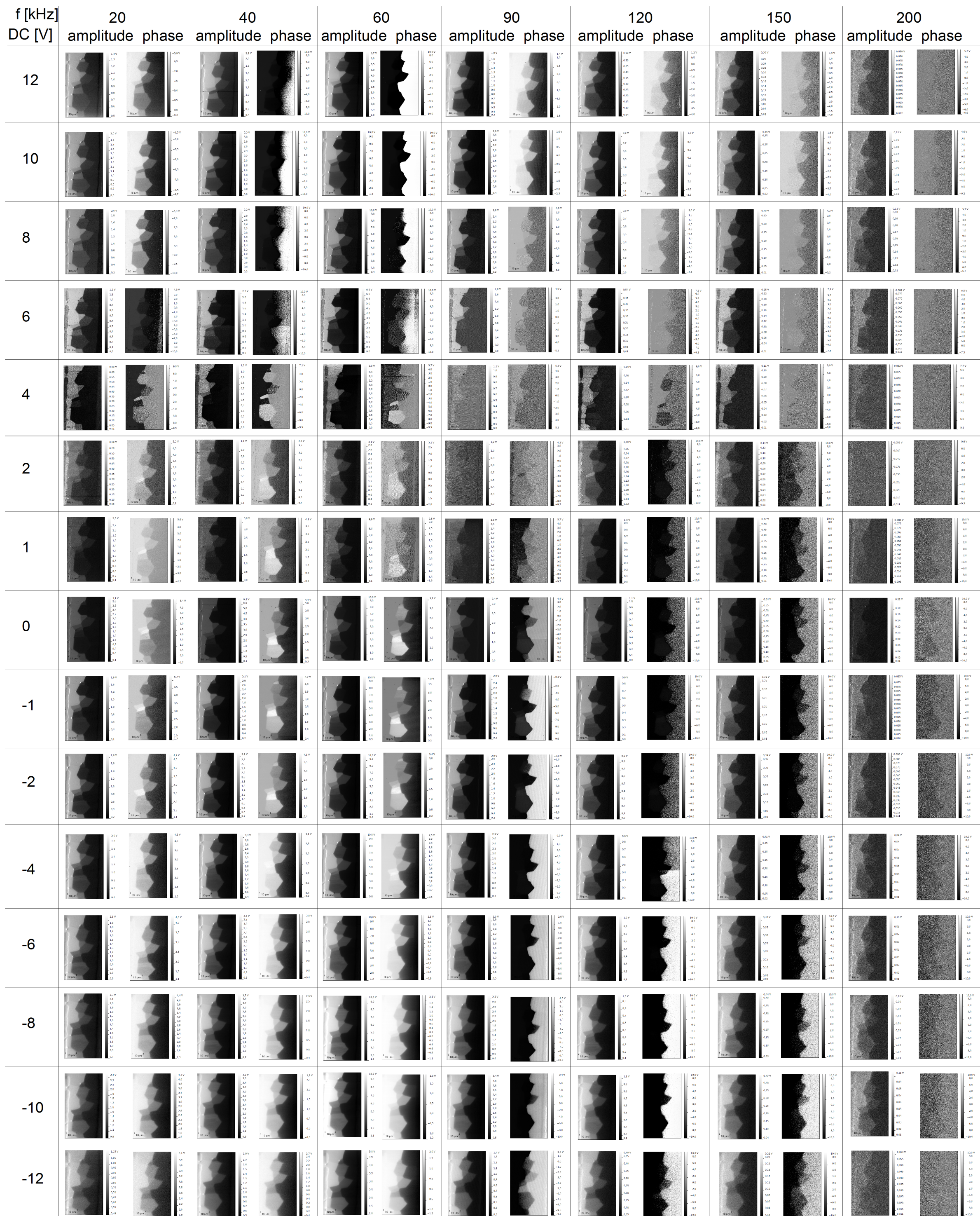

Figure 4.12: Compilation of SIM measurements with frequencies and external nominally applied voltages.

To protect the setup from high currents, a 1 MΩ resistor was connected in series to the varistor. This reduced the effective applied voltage at the varistor device. The effective bias voltages at the varistor were calculated using the current measured during the SIM investigations (see Tab. 4.1). The measured current showed no dependence on the frequency of the AC voltage. A comparison of the resistance calculated that way with a macroscopic measurement of the device showed a very good congruence of the values.

external DC voltage [V]	current [μA]	DC voltage at varistor (V_{DCref}) [V] calc.	AC voltage at varistor (V_{ACref}) [V] calc.
-12	-9.1	-2.9	0.24
-10	-7.9	-2.1	0.21
-8	-6.2	-1.8	0.23
-6	-4.6	-1.4	0.23
-4	-2.9	-1.0	0.26
-2	-1.5	0.5	0.27
-1	-0.9	0.14	0.14
0	0	0	0.14
1	0.9	0.14	0.14
2	1.5	0.5	0.26
4	2.9	1.1	0.29
6	4.5	1.5	0.26
8	6.2	1.8	0.22
10	8.1	1.9	0.19
12	9.5	2.5	0.21

Table 4.1: External applied voltage, measured currents and calculated bias at the varistor.

Fig. 4.13 depicts the SIM investigated area of a Pr doped ZnO varistor. The investigated grains are indicated by numbers. The height image in Fig. 4.13 a) shows the electrodes as higher and therefore bright stripes on the vertical edges of the image. The individual grains are again clearly visible due to their different abrasion behavior.

The SIM amplitude image in Fig. 4.13 b) and the SIM phase image in Fig. 4.13 c) show the output of the lock-in amplifier for the amplitude and respectively the phase signal. The output of the lock-in amplifier is read-in and recorded as a voltage in the AFM controler. Therefore, the values in volts for amplitude and phase are arbitrary units.

The AFM images presented here were taken from the measurement with a DC bias of 0 V and a AC frequency of 20 kHz. Fig. 4.13 d) is an EBSD map of the same area.

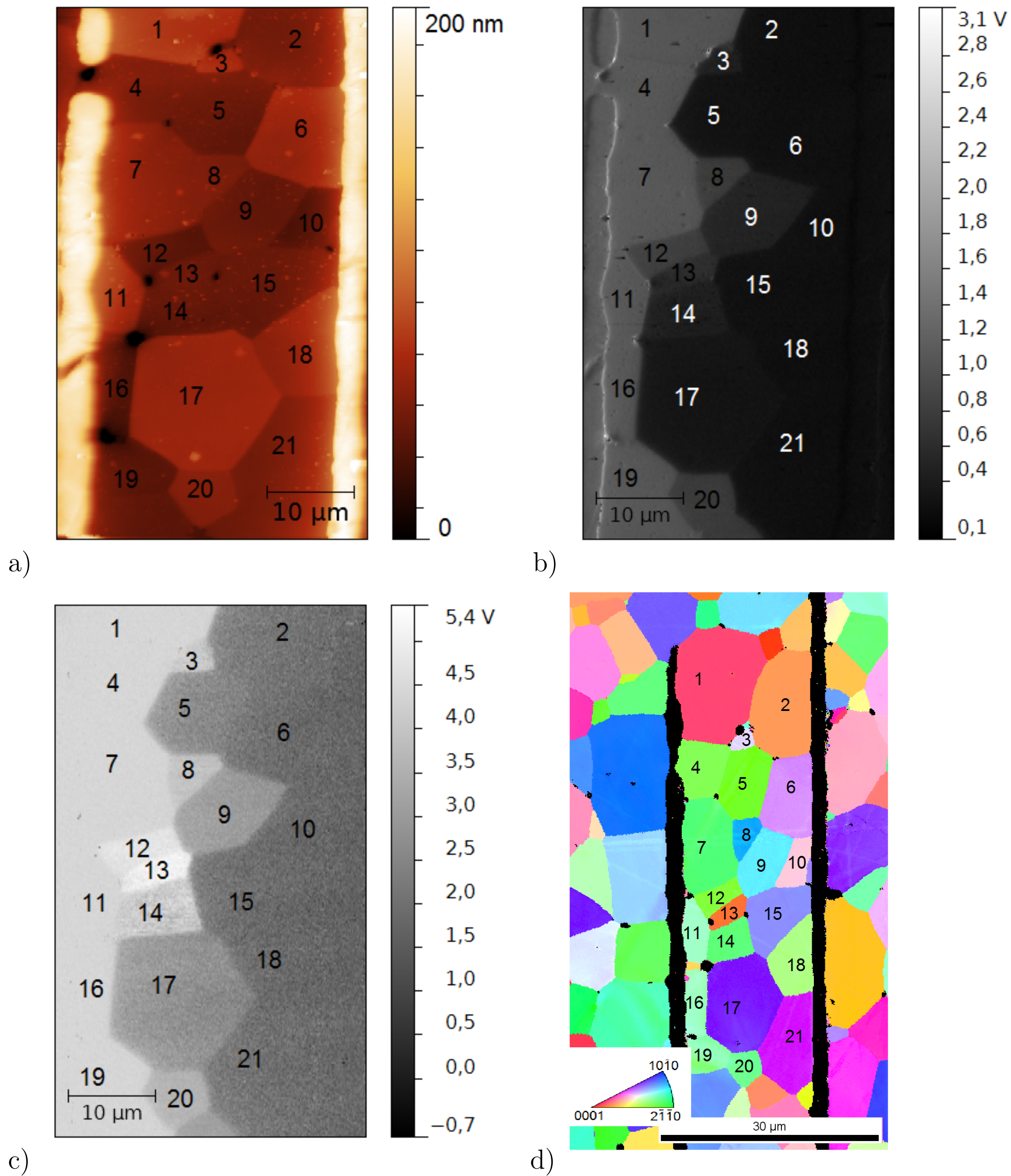

Figure 4.13: SIM measurements at 0V, 20 kHz; a) heigt image; b) SIM amplitude; c) SIM phase; d) EBSD map of the same area; The numbers indicate the investigated ZnO grains.

The same are was also investigated by SSPM (see Fig. 4.14) to obtain the local DC potential V_{DCloc}.

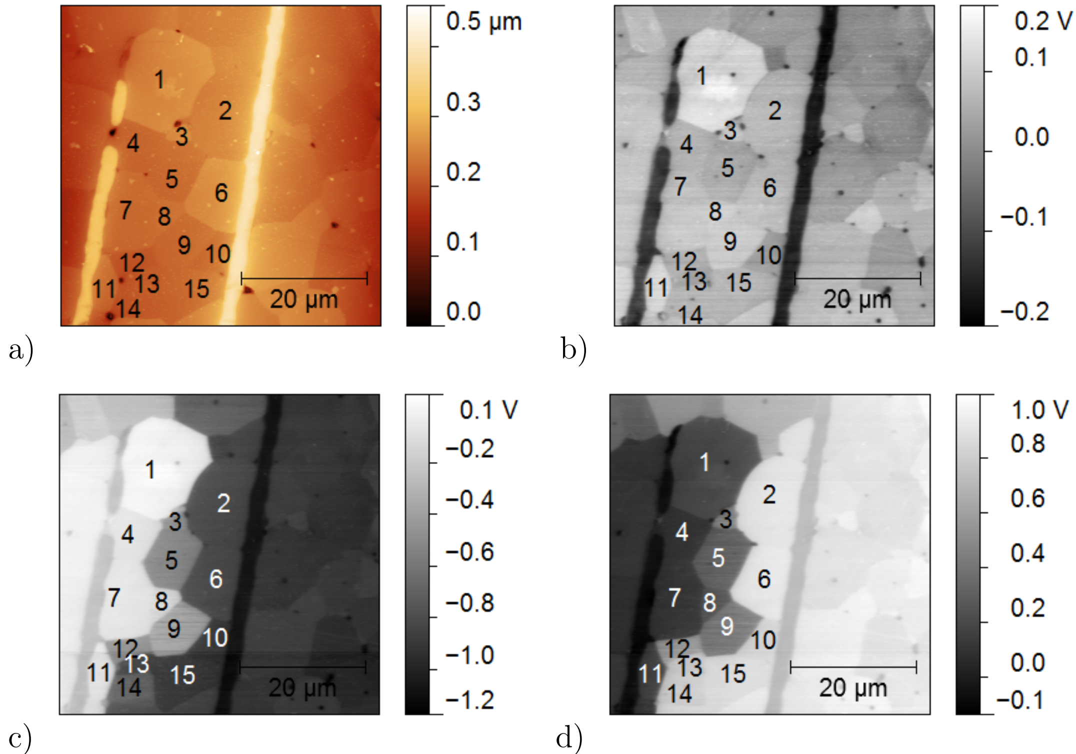

Figure 4.14: SSPM measurements of the area which was investigated by SIM with indicated ZnO grains; a) height image; b) CDP map; c) SSPM measurement at −1 V; d) SSPM measurement at +1 V;

For further analysis, especially the ZnO grains nr. 13 and 14 are considered, because these two grains share grain 11 as closest connection to the left electrode and grain 15 as closest connection to the right electrode. This makes a difference between these two grains independent from the properties of their neighboring grains. In Fig. 4.15 the local SIM amplitudes over external DC voltage and AC frequency are plotted for the grains 11, 13, 14, and 15. A strong increase of the measured amplitude at 60 kHz was observed for all measurements.

This significant increase is most likely caused by an measurement error. The resonance frequency of the employed AFM cantilever was at 70 kHz and thus the signal is strongly amplified close to that frequency. Additional, topography and SIM signal were measured in our first attempt applying single pass technique and not in a two pass mode which has been proposed in the literature [17, 18].

The values calculated after equation 4.7 for V_{ACloc} for the grains 13 and 14 are depicted in Fig. 4.16 a) and b). The maximum values for the local AC voltages appear for both grains at -4 V external bias which yields -1 V applied to the varistor. This means that the local AC voltage mainly depends on the DC bias and less on the AC frequency and the influence of the mechanical resonance frequency of the cantilever on the amplitude signal is compensated by the calculation of V_{ACloc}.

The maximum values calculated for V_{ACloc} are ~3 V which is more than the externally applied bias of 1 V. The exact origin of this anomaly is not yet known, but is addressed to capacitive effects and the mechanic interaction.

In Fig. 4.16 c), the difference in V_{ACloc} for grain 13 and 14 is plotted. The maximal values in difference are found at 60 kHz and 120 kHz at -4 V, i.e. at values where also the values for the individual grains show their maximum.

An attempt was made to develop a set of equations from equations 4.6 and 4.5 to calculate the values for R_{GB} and C_{GB}. Knowing the current through the particular grain boundary would allow to calculate the values for R_{GB} from the SSPM investigations and further to calculate C_{GB}. Since the volume of the varistor and the exact number of grain boundaries involved are not known, estimated current values are used strongly influencing the result. Furthermore, the investigated varistor has possible current paths with only one ZnO grain boundary between the electrodes and thus one or more preferred current paths may evolve and the current distribution in the volume becomes very erratic. The limitations due to the unknown current and current distribution could be overcome by the preparation of a varistor with a thickness of only one layer of ZnO grains. Then the entire volume of the varistor is accessible for investigations by AFM. Until now, it was not possible to produce such a thin specimen out of a MLV due to mechanical destruction of the sample during grinding.

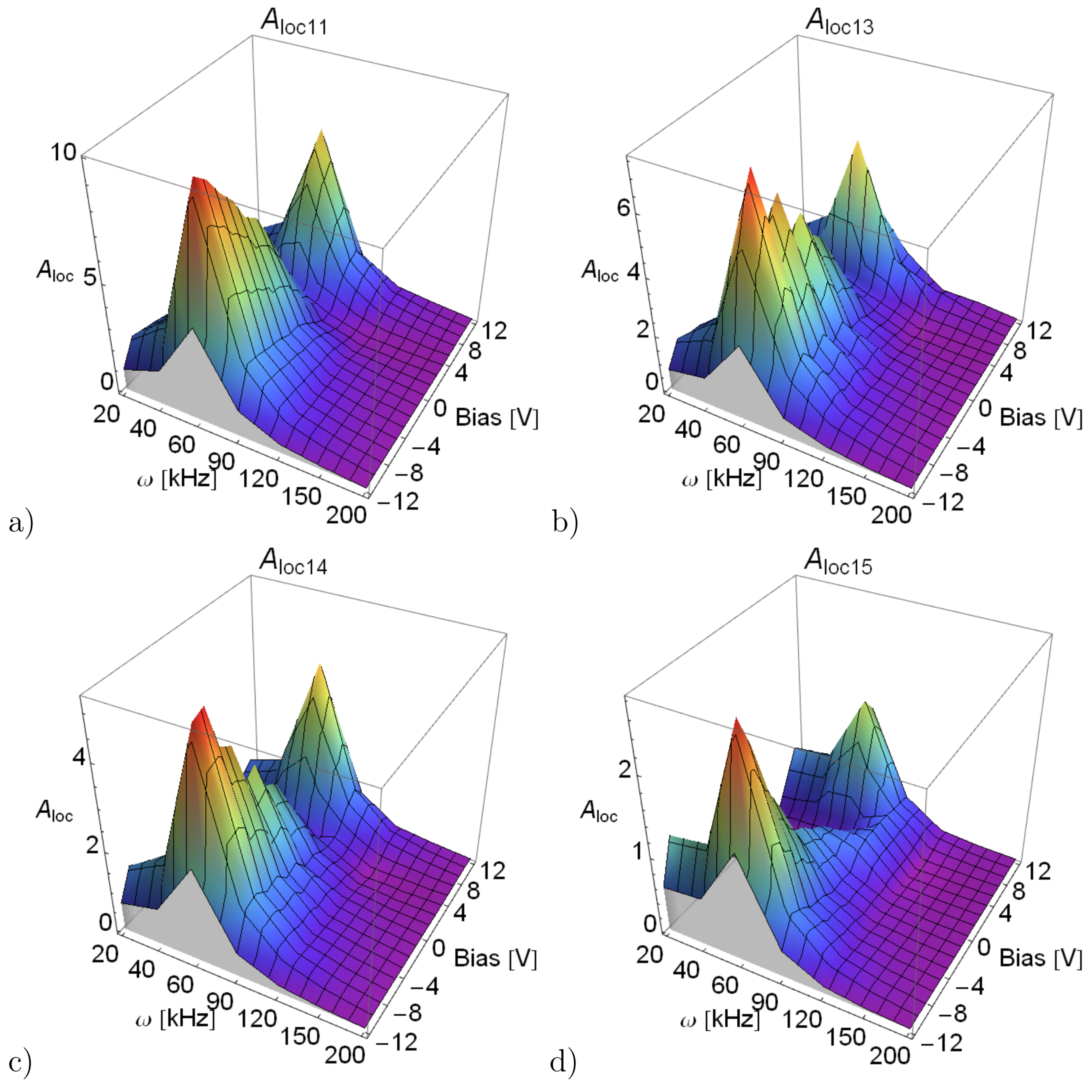

Figure 4.15: Local SIM amplitudes as function of frequency (ω) and DC bias; a) grain 11; b) grain 13; c) grain 14; d) grain 15.

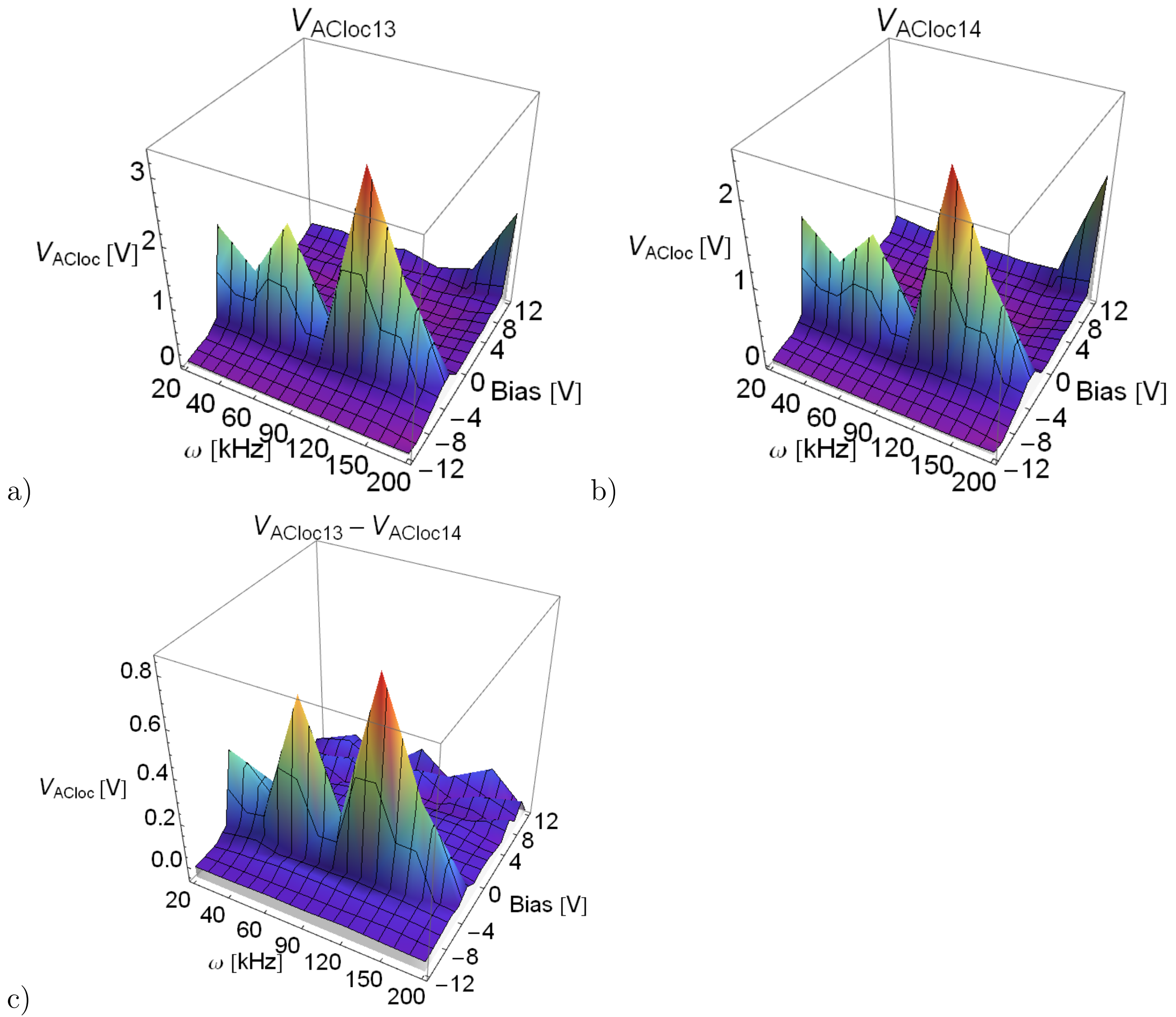

Figure 4.16: V_{ACloc} plotted over external DC bias and AC frequency; a) V_{ACloc} grain 13; b) V_{ACloc} grain 14; c) V_{ACloc} difference between grains 13 and 14.

4.2 Praseodymium system, Micro four-point probe investigations

To measure the electric properties of a grain boundary in a microstructure, the two grains forming the GB have to be electrically contacted. To avoid the influence of contact properties between the probe and the sample surface a four-point probe setup was used (see section 3.4). In this section the results of a M4PP measurement of the Praseodymium system are presented and discussed. In the micro four-point probe measurements, a bias is applied between two neighboring grains and the overall current flow and the potential difference between the grains is measured. Since the surrounding microstructure forms a network of parallel varistors, only a part of the overall current flows through the grain boundary under investigation. Therefore, a simulation of a measurement is first presented to estimate the effect of the surrounding microstructure.

4.2.1 Simulation

In order to show the effect of the expected current flow through the surrounding bulk material, a simulation based on a three-dimensional network model with a realistic microstructure [42] was performed by Michael Hofstätter at the ISFK. The microstructure is generated with the software MBuilder and starts from an array of dense-packed spheres with a given size distribution. The final microstructure is obtained by a cellular automaton and a Monte-Carlo Potts-model [43]. This model utilizes Ostwald ripening, where larger grains are growing on the expense of smaller ones, to result a realistic microstructure. The microstructure used in this simulation consists of 186 grains with an average diameter of 10 µm. In the employed model all GBs are approximated to have the same electrical properties and differ only in their grain boundary contact area.

This characteristic is modeled with an approach similar to that of M. Bartkowiak et al. [44]:

$$j(V) = V\frac{A}{\rho}\left(1+\left(\frac{|V|}{V_{BD}}\right)^{\alpha}\right) , \tag{4.8}$$

where j is the local grain boundary current which is depending on the potential difference V between two neighboring grains. A is the corresponding grain boundary contact area, $\rho = 0.1\,\Omega\mathrm{m}^2$ the specific areal resistance, $V_{BD} = 3\,\mathrm{V}$ the breakdown voltage and $\alpha = 50$ is the non-linear exponent.

For the calculation of the current distribution, a highly non-linear equation system, determined by the first Kirchhoff's law:

$$\sum_{k=1}^{NN} j(V_i - V_k) = 0 \qquad i \,\forall \text{ grains}, \tag{4.9}$$

has to be solved. Eq. 4.9 states that the sum of the currents over all nearest neighbors NN in one grain has to be zero. This condition has to be fulfilled simultaneously for all grains in the system.

The result of the simulation is presented in Fig. 4.17. The color scales in a) and b) illustrate the current flow through the grain volume. The voltage is applied to the two neighboring grains with the GB under investigation in between them. Fig. 4.17 a) shows the current flow with a bias voltage of 2.2 V where the investigated grain boundary is in the high resistance region below the breakdown of the Schottky barrier. In this case, the microstructure acts like a network of parallel and serial Ohmic resistors and a significant current flow through the surrounding grains is clearly visible. The same volume in the switching regime at 3.4 V bias is depicted in Fig. 4.17 b). Here, the GB under investigation shows far less resistivity and the surrounding grains contribute to a much lesser extent to the overall current flow. However, the overall current flow is one hundred times higher than in the first case. The simulated current - voltage characteristics of the investigated GB in comparison to the integral current is displayed in a double logarithmic plot in Fig. 4.17 c). As clearly visible in the plot, the simulated model predicts for the low-voltage region that only one fifth of the entire current flows across the investigated GB. Above the Schottky barrier breakdown of the investigated GB, the relative contribution of the current flow through the surrounding bulk material becomes minor. From this finding it can be stated that the exponential factor α, which is determined from the slope in the high voltage region, is not significantly influenced by the surrounding.

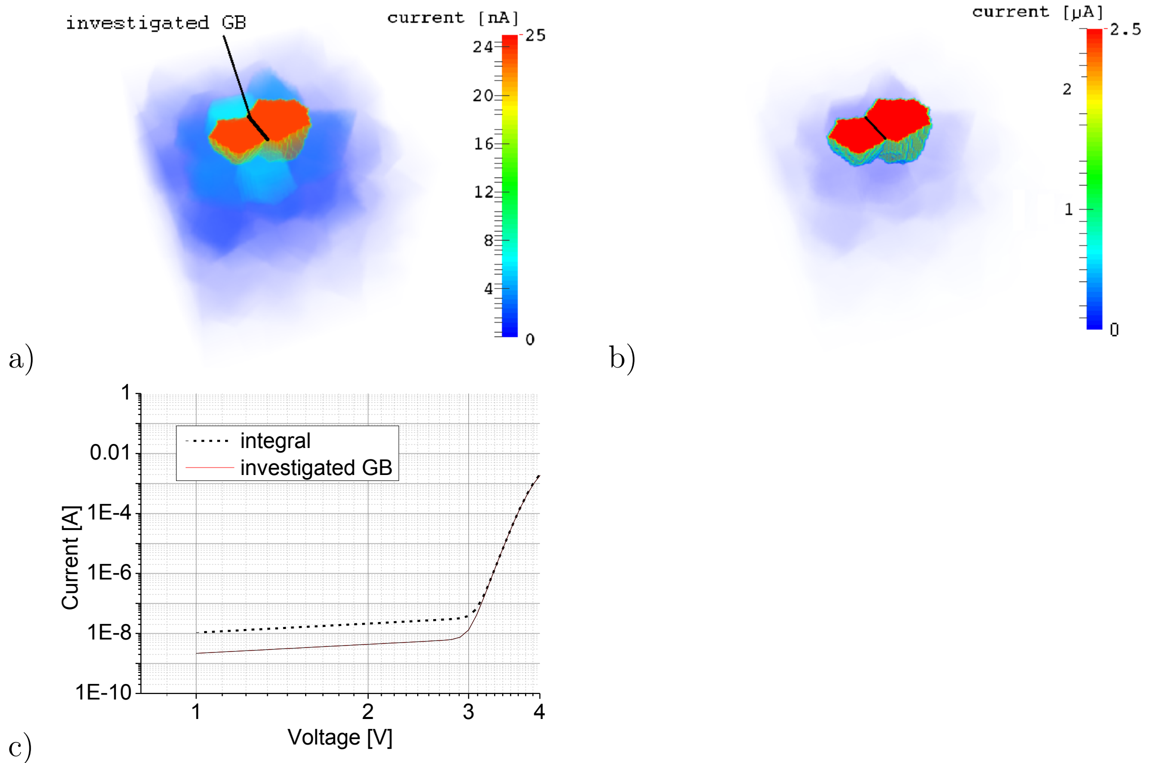

Figure 4.17: Simulated M4PP measurement; a) relative current flow at 2.2 V; b) relative current flow at 3.4 V; c) simulated I-V characteristics for the investigated GB and the entire ensemble in a double logarithmic plot.

4.2.2 Experimental results

In the following, the results of M4PP measurements of individual ZnO grain boundaries and of individual ZnO grain - MLV electrode interfaces are presented. As convention, forward direction (FWD) means a positive voltage applied to probe 1, backward direction (BWD) means a negative voltage applied to probe 1. The samples were taken from the series with 8 μm grain size and only one pair of electrodes.

ZnO-ZnO grain boundary properties

For the ZnO grain boundary measurements, the varistor electrodes were grounded to prevent electrostatic charging of the samples, and only the inactive area (not between the MLV electrodes) with at least two grain boundaries distance from the electrodes was investigated to avoid current flow through the varistor electrodes.

In Fig. 4.18, the optical microscopy image and the EBSD map of one of the samples are displayed. The white numbers in the optical micrograph and the black encircled numbers in the EBSD map denote three exemplary GBs whose corresponding M4PP measurement curves in FWD and BWD are presented in Fig. 4.19 in a double logarithmic plot.

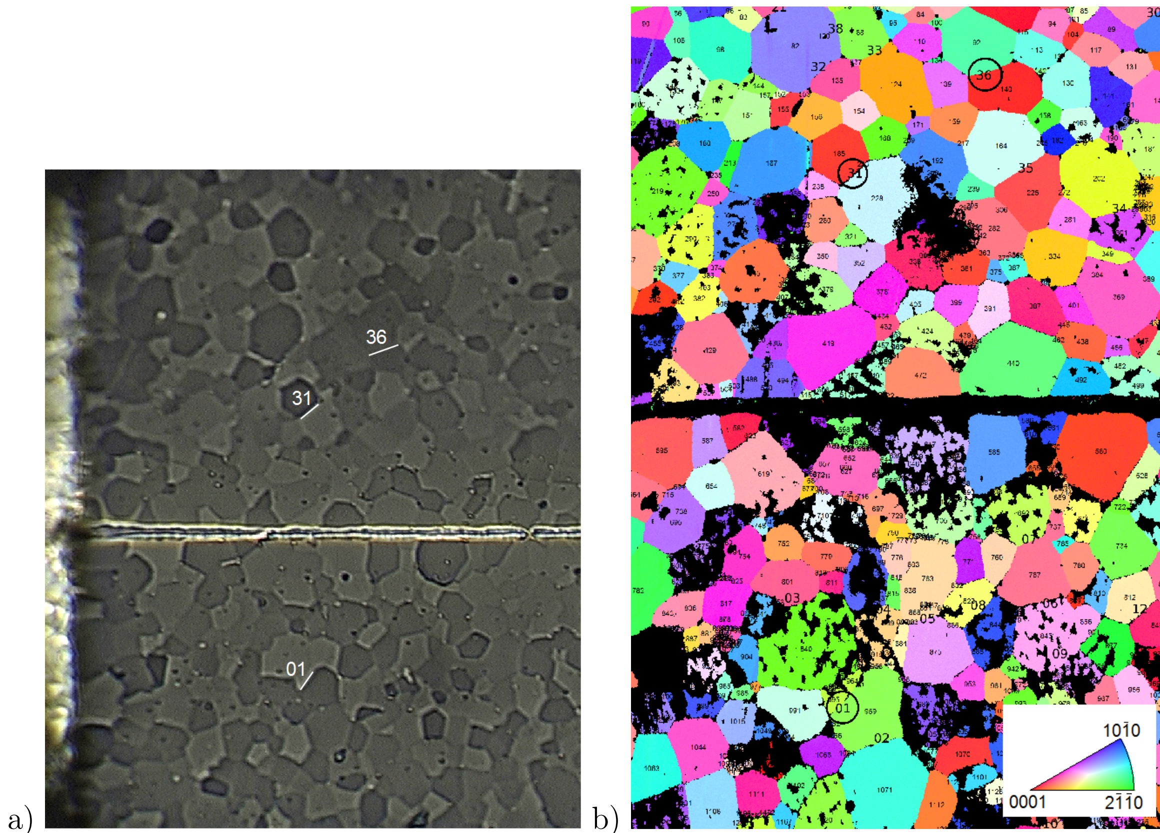

Figure 4.18: One of the samples used for the M4PP investigation; a) Stitched optical micrograph with a termination on the left end and a horizontal electrode in the middle; b) EBSD map of the same area. The locations of three particular grain boundaries are indicated.

To fit the logarithmic data of each individual measurement, a piecewise defined function using the software MATLAB was employed. This continuous fit function consists of three linear parts, where the slopes and the transition constants are fitting parameters. Every grain boundary was measured several times to prove the stability and reproducibility of the measurement. The data showed low noise and a high reproducibility. Thus no averaging was necessary and only one curve per GB analysis was used for analysis.

The exemplary curves presented in Fig. 4.19 allow to define basically three electrical regions. Region one is the high voltage regime above the level of Schottky barrier

breakdown. The regions two and three are in the high resistive leakage region below this point.

The reader is reminded that at even higher voltages and currents, i. e. above region I, the varistor GBs is expected to show again Ohmic behavior due to the resistivity of the ZnO bulk material [2]. But, due to the necessary high voltages and currents which might destroy the sample and the probes, this regime was not investigated in this study.

In Fig. 4.19 a) the characteristic parameters for a detailed and a statistical analysis of the three electrical regimes are introduced and indicated. As common in literature, the slope in region I is denoted as α. Consequently, β and γ are used for the slopes in regions II and III. The point between regions I and II is the Schottky barrier breakdown and indicates the breakdown voltage V_{BD} and the current at breakdown I_{BD}. At the kink between region II and III, the values $V_{\beta-\gamma}$ for the voltage and $I_{\beta-\gamma}$ for current are defined. In the following, different possible GB characteristics, which are illustrated by the three curves in Fig. 4.19, are discussed. The curve in Fig. 4.19 a) is an example for a rather symmetrical behavior without a pronounced difference in breakdown voltage for FWD and BWD. But it exhibits a significant difference for the current at breakdown I_{BD}. Both curves show the same trend in region II and III, nevertheless, the slopes β and γ and the values for $V_{\beta-\gamma}$ and $I_{\beta-\gamma}$ are different. The majority of the measured curves (65 out of 82) showed a similar characteristic. Fig. 4.19 b) presents an example for a GB measurement with a clear deviation in forward and backward direction. Especially the slopes β and γ and the values at the kink $V_{\beta-\gamma}$ and $I_{\beta-\gamma}$ differ clearly. An inflection point like the kink in the FWD curve, measured in Fig. 4.19 b), was found on seven GBs, one GB showed a negative inflection in both directions. Finally, the measurement presented in Fig. 4.19 c) is an example for sub-Ohmic behavior in region II in one direction, as it was found at six GBs. Three GBs showed even sub-Ohmic behavior in both directions. This grain boundary behavior can not be explained sufficiently by the standard double Schottky barrier model. Therefore, effects like strong barrier pinning and the contribution of deep donor levels have to be considered in the description of semiconductor GB behavior [45]. Also, one has to note that the curve presented in Fig. 4.19 c) possesses no pronounced inflection between region II and III for the BWD. The fitting procedure resulted for all curves without pronounced inflection point in a value between 1 V and 2 V for $V_{\beta-\gamma}$ where these curves showed indeed a slight inflection.

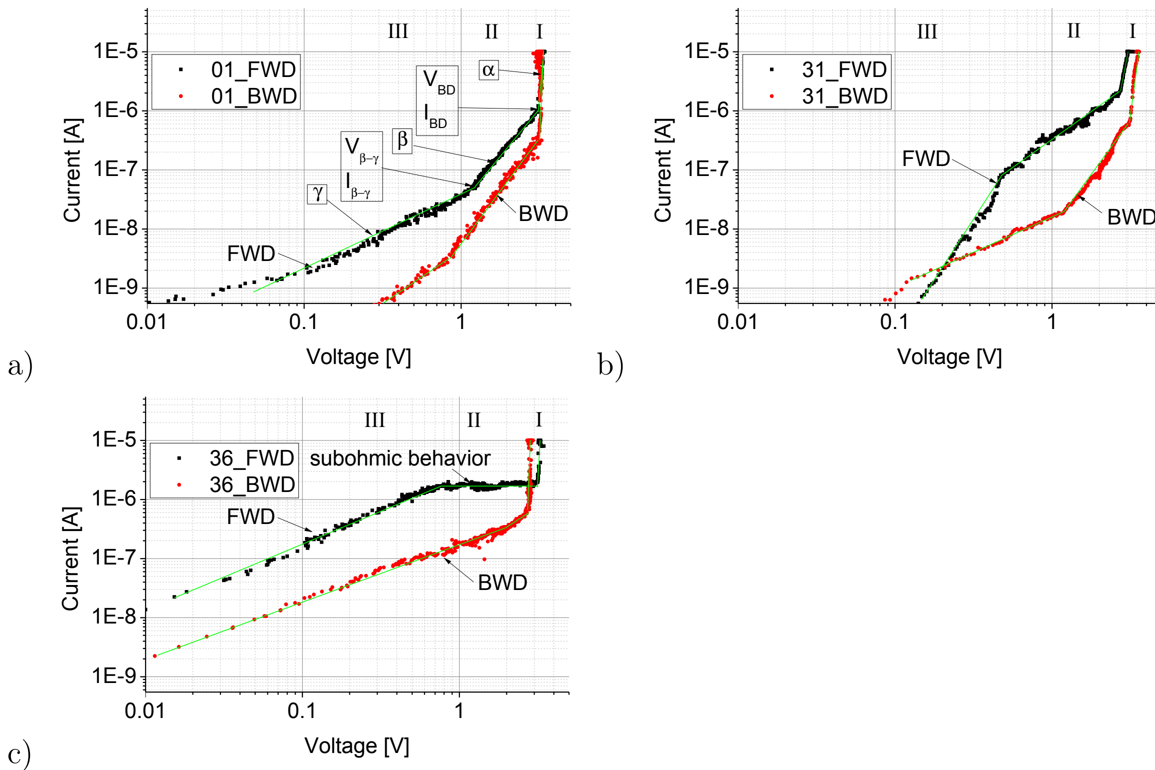

Figure 4.19: M4PP measured I-V curves of the three exemplary grain boundaries, indicated in Fig. 4.18: a) GB 01 with indication of the parameters for the statistical analysis; b) GB 31; c) GB 36.

For a statistical overview on the electrical behavior of the GBs, histograms and plots of the before defined electrical parameters from 41 GBs (resulting in 82 curves in FWD and BWD direction) are provided in the following.

The most important characterization parameters for varistor ceramics are the nonlinearity value α and the breakdown voltage V_{BD} [5]. The value for α is not significantly influenced by current flow through the surrounding microstructure, as demonstrated by the simulation. A histogram of the α values, obtained in this study, is presented in Fig. 4.20. A spread of α-values from below 10 up to 150 with a maximum around 20 was found. In the literature values between 35 and 100 [5, 3] but also values below 10 [28] are reported.

The V_{BD} values for individual GBs measured in this study are only slightly influenced by the surrounding and range from 2.3 V to 3.6 V, with the highest number of counts between 3 V and 3.4 V, as depicted in the histogram in Fig. 4.21 a). This is in good

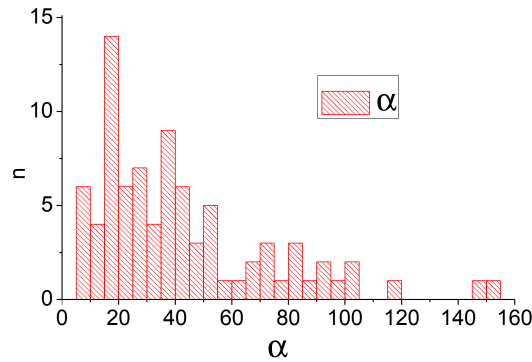

Figure 4.20: Histogram of slopes in region I (41 GBs ⇒ 82 curves).

agreement with data from the literature where V_{BD} values from 3 V to 3.5 V are reported [2, 46]. As the simulation demonstrated, the value for the current at switching and the values in the low voltage regime are strongly influenced by the surrounding. Despite this, the full range of the obtained data is considered because the investigated GBs differ significantly even below the point of barrier breakdown. The current at barrier breakdown, I_{BD} is strongly influenced by the surrounding, and only about one fifth of the current flows across the GB under investigation. Therefore, an averaging effect of the alternative current paths through the surrounding grains can be expected. Nevertheless, as the histogram in Fig. 4.21 b) shows, a wide range of values from $\sim 0.05\,\mu$A to a few μA was found. Fig. 4.21 c) is a semilogarithmic plot of I_{BD} over V_{BD} to depict a possible relation between these two values. But no significant relation was found.

The histograms in Fig. 4.22 a) and b) are depicting the values for voltage and current at the first kink ($V_{\beta-\gamma}$, $I_{\beta-\gamma}$). For the majority of curves an $I_{\beta-\gamma}$ current below 0.1 μA was recorded, but occasionally also values in the μA range were measured. The values for $V_{\beta-\gamma}$ lie around 1 V, several values reach up to 2 V and one value was found to be 2.5 V. In Fig. 4.23 histograms of the slopes in region II and III (β, γ) of the I-V curves are shown. The exponent in region II is in the range between $<$1 and 6, with one curve showing a β value of 11. γ ranges from $<$1 up to $\sim$8.

All the values obtained from M4PP measurements indicate a wide spread of electrical properties for the individual grain boundaries. In normal operation mode of a varistor device with applied voltages below the breakdown voltage, the values in region II and III determine the leakage current and thus the power loss due to the varistor device. Therefore, low values for $I_{\beta-\gamma}$ and I_{BD} are desired. The breakdown voltage V_{BD} and

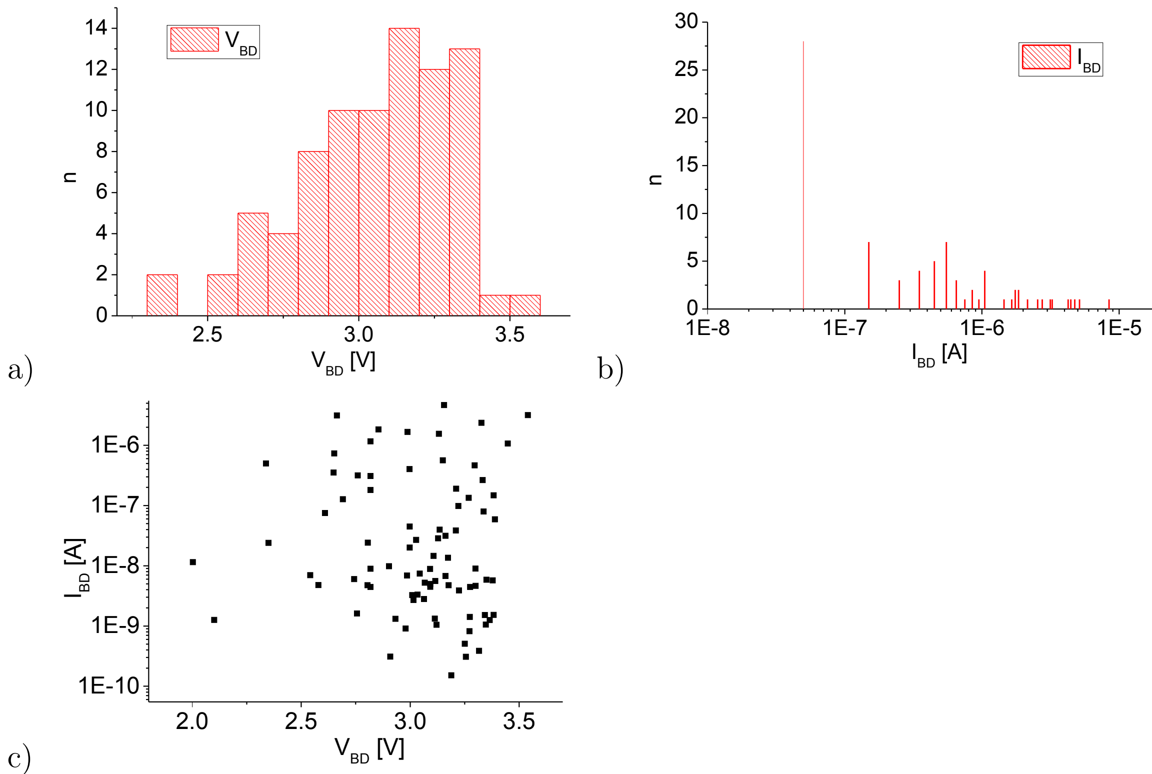

Figure 4.21: Plots of the values at the point of breakdown: a) Histogram of the breakdown voltage V_{BD}; b) Histogram of the current at breakdown I_{BD}; c) Current at breakdown I_{BD} over breakdown voltage V_{BD} (current scales are logarithmic).

the nonlinearity exponent α are the most crucial design parameters. The exponent α indicates the ability of a varistor to transport currents from overvoltages, and therefore high α values are desired. For V_{BD}, a low spread in values is favorable since a wide spread enforces the formation of preferred current paths in the varistor device. These current paths may cause local hot spots which can destroy the device [20, 41].

It was tried to correlate the electrical properties of individual GBs with the crystallographic orientation of the polar ZnO axis (c-axis) relative to the grain boundary (see the EBSD image in Fig. 4.18 b). Therefore, the angle between the polar axis and the grain boundary normal was calculated. The GB normal was constructed as line through the center of masses of the two adjacent grains. For this calculation, the grain boundary normal was assumed to be parallel to the sample surface. The drawback of EBSD is that it yields only a two-dimensional information of the crystallographic orientation of the grains at the surface. But, the GBs are propagating down in the bulk in any arbitrary

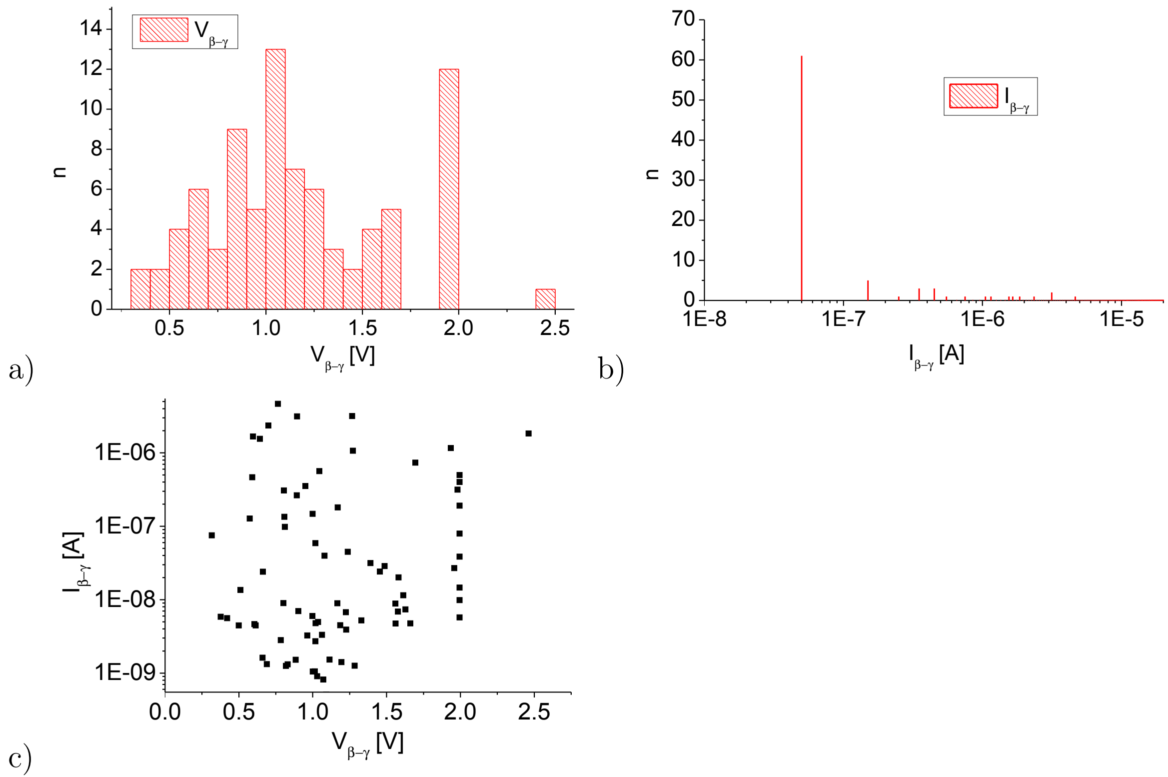

Figure 4.22: Plots of the values at the first kink: a) Histogram of the voltage $V_{\beta-\gamma}$; b) Histogram of the current $I_{\beta-\gamma}$; c) Current $I_{\beta-\gamma}$ over voltage $V_{\beta-\gamma}$ (current plotted in logarithmic scale).

direction. Therefore it is not possible to determine the real orientation of the GBs and the facets forming the grain boundaries. Measuring a three-dimensional crystallographic profile to obtain the real GB orientation, would need time consuming EBSD measurements in combination with subsequent ablation of the surface e.g. by a focused ion beam.

ZnO-electrode contact properties

The ZnO-electrode interfaces were investigated since they form - as semiconductor-metal junctions - also Schottky barriers. For this investigations, the varistor electrodes were externally connected to probe four, because the electrodes were too thin to place probe three and four on them. Two examples out of 20 measured ZnO-to-Ag/Pd electrode interfaces are presented in Fig. 4.24. As can be seen in the two curves, the ZnO-electrode interfaces show a much higher conductivity than the ZnO-to-ZnO grain boundaries.

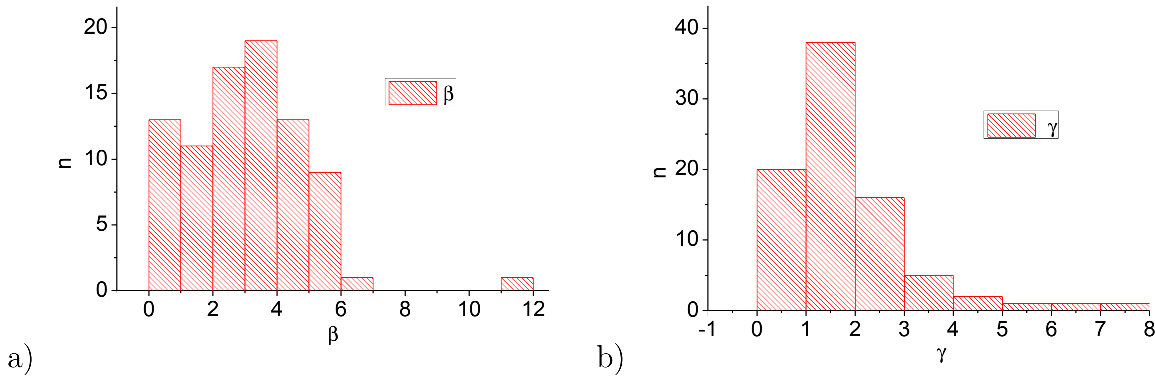

Figure 4.23: Histogram of slopes extracted from the two linear regions in the log-log plots (high resistive regime); a) region II; b) region III (41 GBs).

This means that the formation of GBs with varistor effect requires two semiconductor materials and the ZnO-electrode interfaces contribute less to the device behavior than the grain boundaries. This is also in agreement with the results of the SSPM investigations (see section 4.1.2) where no pronounced barrier between the electrodes and the adjacent ZnO grains was found. Nevertheless, a spread in properties from Ohmic and nearly symmetric behavior, as in Fig. 4.24 a), to nonlinear and asymmetric characteristics, as in Fig. 4.24 b), was found. This spread in properties might fortify the formation of preferred current paths in devices with low switching voltages (see section 4.1.2).

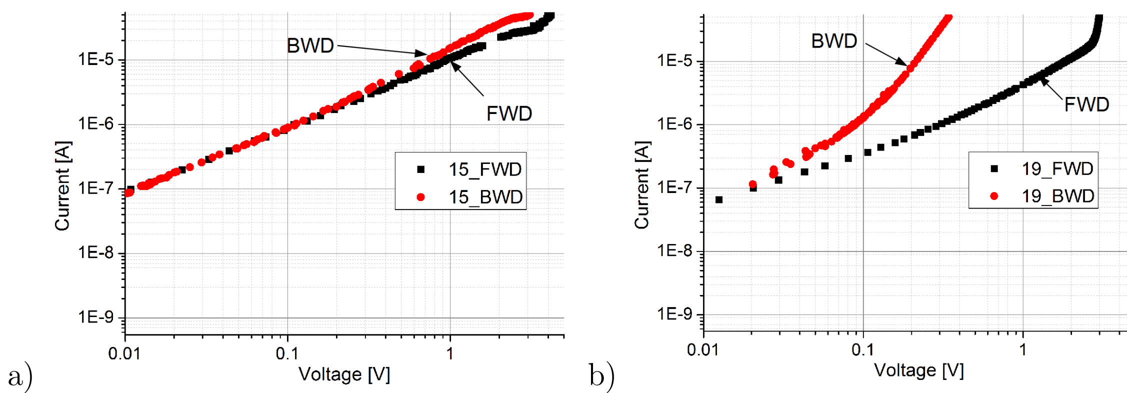

Figure 4.24: I - V curves of two exemplary ZnO to MLV electrode interfaces; a) Ohmic and symmetric behavior; b) nonlinear and asymmetric behavior.

4.3 Bismuth system, AFM based investigations

4.3.1 C-AFM investigations

A C-AFM investigation of a Bismuth doped sample is presented in Fig. 4.25. The heigt image in a) shows ZnO grains and other phases like spinel eclusions and the grain boundary phase as described in section 2.2.3. The electrode can be clearly seen in the current image Fig. 4.25 b). As already seen for the Pr system, the ZnO grains represent areas with constant current signal. The highest current is found in grains close to the electrodes and is decreasing with distance to the electrode. Nonconductive phases appear in the current image as dark areas mainly between the conductive ZnO grains. In the current image a diagonal eight to nine µm wide stripe, which shows no current signal can be seen. This stripe is assumed to origin from a thin film of residuals from the sample preparation. To increase the visibility of grains with a lower current the color scale was set from 0 to 1 nA whereas the maximum current of the white areas is 10 nA.

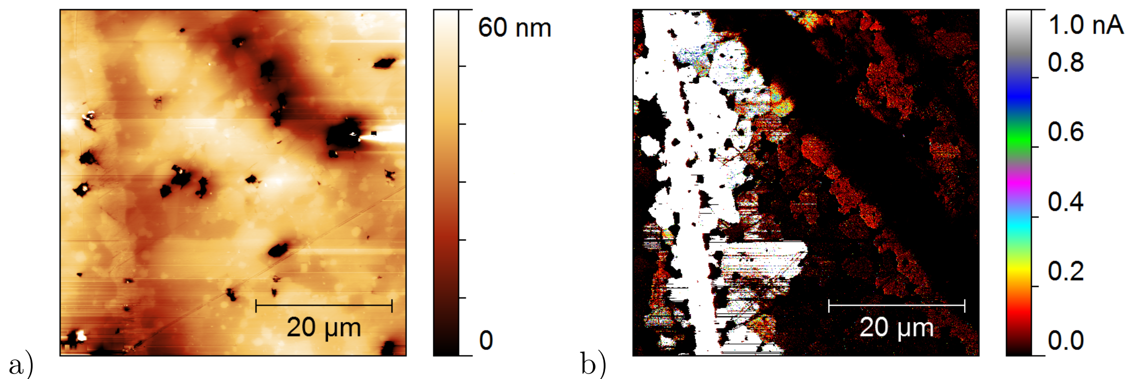

Figure 4.25: C-AFM investigation of a Bi system sample; a) height image; b) current image at +8 V.

Photolithographic deposition of silver dots

In order to establish Ohmic contacts between the AFM tip and the sample surface, Ag dots were deposited with a photolithographic process on a Bi system sample by J. Fleig, TU Wien. The sample with dots is displayed in an optical micrograph in Fig. 4.26 a) and in an AC mode height image in Fig. 4.26 b). The Ag dots are circular with a diameter of 5 µm and a height of ~50 nm. The white debris with a height of ~0.6 µm

above the dots is regarded as residual from the photolithographic process. The density of the deposited dots caused short circuits over ZnO grain boundaries and the residuals from the photolithographic process were covering the AFM tip. Therefore meaningful electrical measurement were not possible and this method was not further pursued.

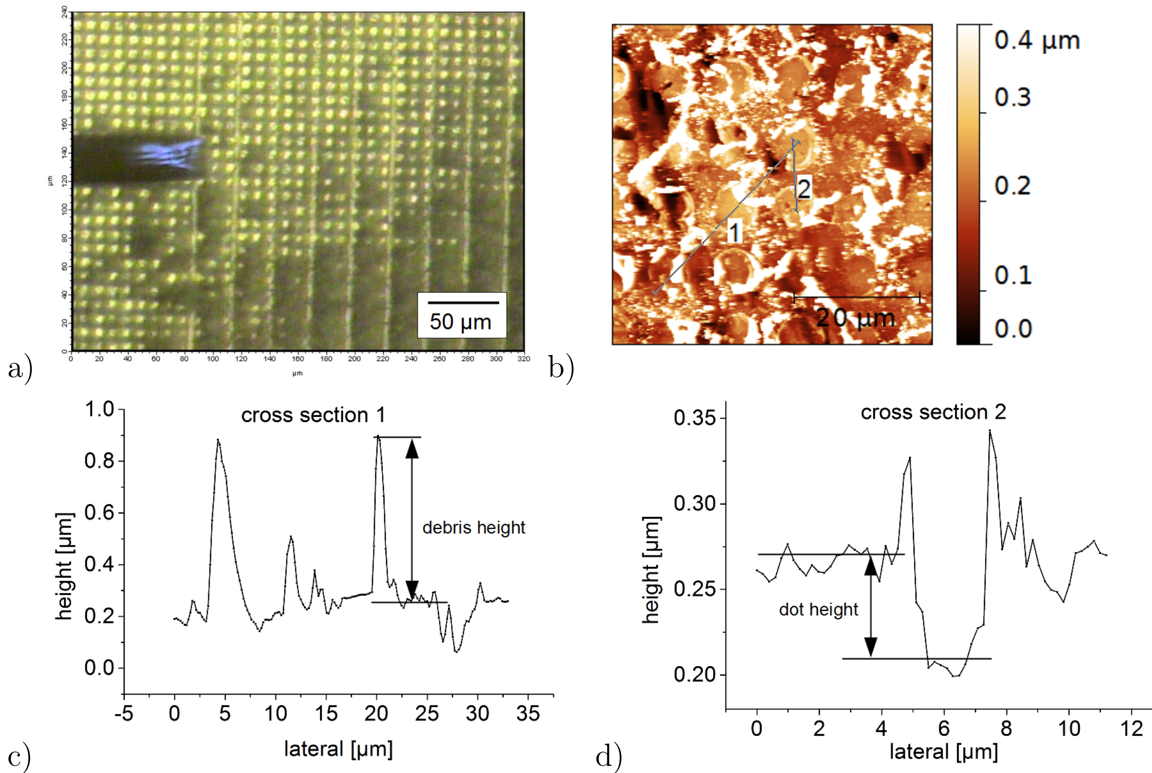

Figure 4.26: Photolithographic deposited Ag-dots; a) optical microscopy image; b) height image; c) cross section 1; d) cross section 2.

4.3.2 KPFM and SSPM investigations

The results of a KPFM and SSPM investigation of a Bi system sample are displayed in Fig. 4.27. For this investigation, a specimen with an average grain size of 5 µm and an electrode distance of approximately 30 µm was used. The typical microstructure of a Bi system (see section 2.2.3) can be seen in the height image, Fig. 4.27 a) and in the CPD image Fig. 4.27 b). The spinel phases with a diameter of less than 1 µm are found at the grain interior. The Bi-rich phase at the grain boundary and especially at the grain triple junctions is strongly visible as bright areas in the CPD image. Also, several holes with a diameter up to 5 µm can be seen in the microstructure. These holes are pores from

sintering or breakouts from polishing. Fig. 4.27 c) and d) are SSPM scans wit a bias of −8 V and +8 V applied. The red marked cross sections are displayed in Fig. 4.27 e). A terrace like structure can be seen as in the Pr system samples. The spinel phases are not visible in the SSPM images since they are at the same potential as the surrounding grain.

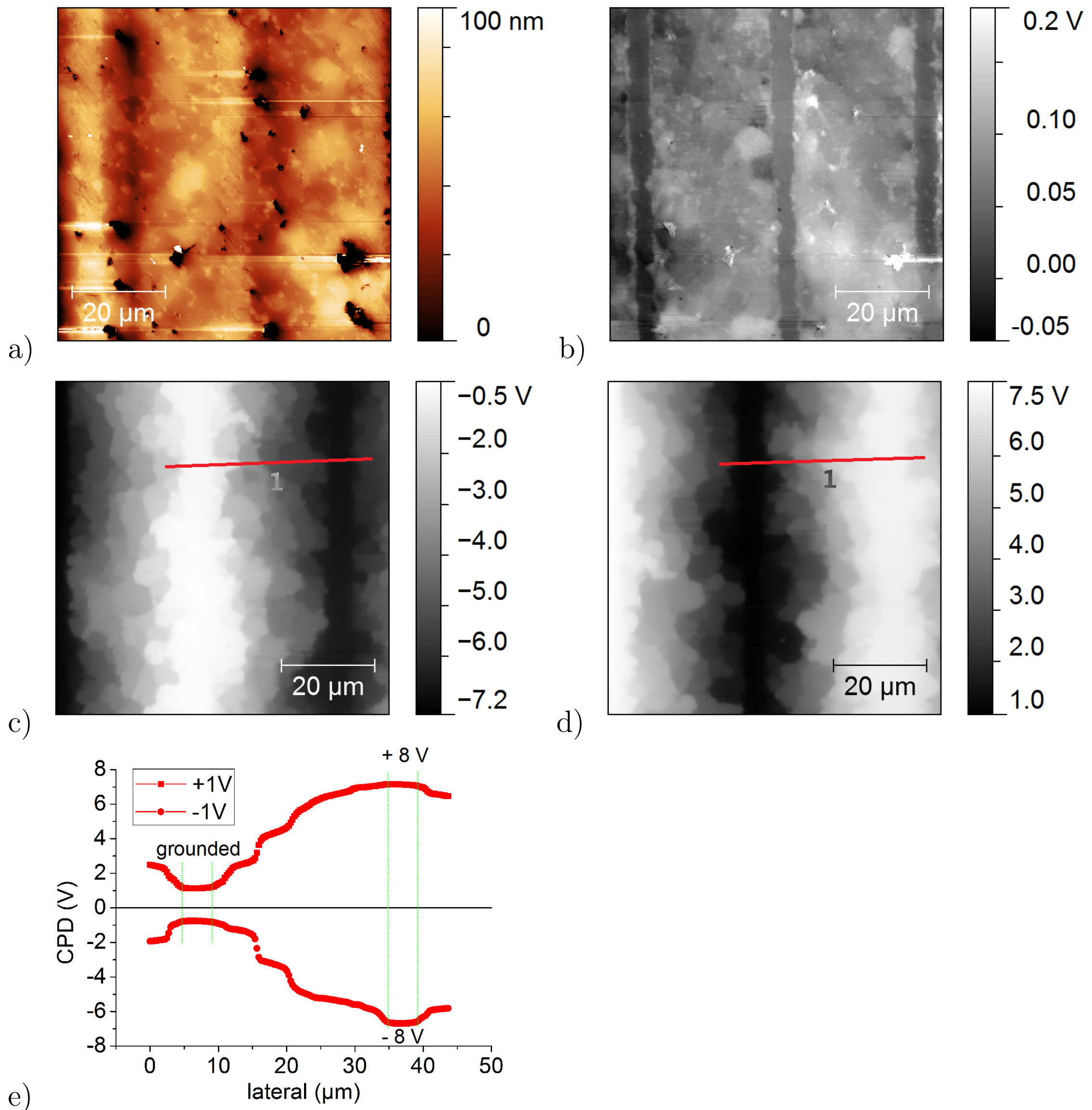

Figure 4.27: KPFM and SSPM investigation of an Bi doped specimen; a) height image; b) CPD map; c) SSPM map at −8 V; d) SSPM map at +8 V; e) cross sections from c) and d)

5 Summary and Outlook

In this work, the electrical properties of grain boundaries in ZnO based varistor ceramics were investigated by conductive probe based techniques. The focus of investigation was set on Pr doped ZnO varistor ceramics but also Bi doped systems were studied.

On the one hand, the microstructure was investigated with AFM based methods like C-AFM, KPFM, SSPM, and SIM. On the other hand, the electrical properties of individual grain boundaries were obtained with a micro four-point probe setup, which was set up during this work. The AFM based techniques proved the high conductivity of the grain interior and the high resistivity at the grain boundary. With C-AFM it was possible to perform areal current scans which showed uniform current levels within one grain and a high resistivity at the grain boundaries. It was also possible to measure the local electric properties with I-V curves on selected points. But, these measurements were strongly influenced by the nonlinear and unstable contact properties between the AFM tip and the sample surface. With KPFM it was demonstrated that different ZnO surfaces differ in their work function and therefore individual grains can be distinguished by the CPD. SSPM proved the result of C-AFM with a high conductivity of the grain interior and voltage drops at the GB.

In a Pr doped sample with a small number of GBs between the electrodes, a preferred current path for one direction of the externally applied bias was found by lock-in thermography. By SSPM one specific grain boundary with reduced resistivity for one direction was identified which caused the preferred current path and the asymmetric I - V behavior of the entire device. In SSPM investigations also current paths across two GBs with asymmetric behavior were found.

SIM measurements were performed to measure the frequency dependent electrical properties of the grain boundaries. In these measurements a dependence of the local AC amplitude on the applied DC bias was found. The SIM measurements were performed

at the CNMS, Oak Ridge, Tennessee, USA. The at the CNMS obtained knowledge will be used to implement the possibility of SIM measurements in Leoben.

It was demonstrated that M4PP allows to measure the I-V properties of individual grain boundaries in a reliable way. In these measurements, an unexpected wide spread of the electrical properties was found. The non-linearity factor α showed values between 6 and 150 and for the voltage at barrier breakdown, V_{BD}, values between 2.3 V and 3.6 V, with the highest number of counts between 3 V and 3.4 V were found. A simulation showed that below the breakdown voltage only about 20% of the measured current flows through the grain boundary under investigation. But, despite this fact a wide spread in characteristics of the low voltage regime was found.

For the M4PP investigations, a grain size of at least 8 µm is necessary for the positioning of the probes. Therefore only one type of Pr doped multilayer varistors with sufficiently large grains was investigated. Further work could be performed on Bi doped high voltage varistors. Since ZnO is a piezoelectric material, mechanical stress is causing the development of a local electric field inside the ZnO grains. Stress depended electrical measurements of individual grain boundaries could reveal polarity and charge dependent electrical properties.

EBSD scans allowed to determine the crystallographic orientation of the ZnO grains. Since EBSD is measuring only the orientation at the surface of the sample it is not possible to determine the orientation of the grain boundaries which are propagating down in the bulk. An iterative process of EBSD measurement and ablation of the sample surface with a focused ion beam would allow to generate a three-dimensional model of the microstructure and therefore determine the orientation and the area of the grain boundaries.

A limiting factor in all investigations was the unknown active sample volume and the unknown distribution of the current flow through the specimen. Some effort was taken to fabricate samples with only one layer of grains in thickness by mechanical grinding and polishing. But, until now all samples were lost due to mechanical destruction during polishing. Further experiments in this field will be done by varying the employed resin to fix the samples. Also experiments with alternative sample preparation methods like ion beam milling will be performed.

Bibliography

[1] F. Greuter, R.S. Perkins, and M. Holzer. MO-Varistors: State of the art and actual trends. *Cigre*, 2012.

[2] David R. Clarke. Varistor ceramics. *J. Am. Ceram. Soc.*, 82:485–502, 1999.

[3] Kazuo Eda. Zinc oxide varistors. *IEEE Electrical Insulation Magazine*, 5:28–35, 1989.

[4] K. Mukae, K. Tsuda, and I. Nagasawa. Capacitance-vs-voltage characteristics of ZnO varistors. *J. Appl. Phys.*, 50:4475–4476, 1979.

[5] K Gupta, Tapan. Application of zinc oxide varistors. *J. Am. Ceram. Soc.*, 73:1817–1840, 1990.

[6] G. Blatter and F. Greuter. Carrier transport through grain boundaries in semiconductors. *Phys. Rev. B*, 33:3952–3966, 1986.

[7] M. Piber and H. Gruenbichler. Varistorkeramik, Vielschichtbauelement umfassend die Varistorkeramik, Herstellungsverfahren für die Varistorkeramik. DE 10 2009 023 847 A1, 2010.

[8] M. Piber. Varistorkeramik, Vielschichtbauelement umfassend die Varistorkeramik, Herstellungsverfahren für die Varistorkeramik. DE 10 2009 023 846 A1, 2010.

[9] G. Binning, C.F. Quate, and Ch. Gerber. Atomic force microscope. *Phys. Rev. Lett.*, 56:930–933, 1986.

[10] A. Olbrich, B. Ebersberger, and C. Boit. Conducting atomic force microscopy for nanoscale electrical characterization of thin SiO_2. *App. Phys. Lett.*, 73:3114–316, 1998.

[11] C. Teichert and I. Beinik. *Scanning Probe Microscopy in Nanoscience and Nanotechnology*, volume 2, chapter Conductive Atomic Force Microscopy Investigation of Nanostructures in Microelectronics, pages 691–721. Springer-Verlag, Berlin, 2011.

[12] M. Nonnenmacher, M. P. O'Boyle, and H. K. Wickramasinghe. Kelvin probe force microscopy. *Appl. Phys. Lett.*, 58(25):2921–2923, 1991.

[13] S. Sadewasser and T. Glatzel, editors. *Kelvin Probe Force Microscopy.* Springer-Series in Surface Sciences, 2012.

[14] M. Fujihira. Kelvin probe force microscopy of molecular surfaces. *Ann. Rev. Mat. Sci.*, 29:353–380, 1999.

[15] B. D. Huey and D. A. Bonnell. Spatially localized dynamic properties of individual interfaces in semiconducting oxides. *Appl. Phys. Lett.*, 76:1012–1014, 2000.

[16] S. V. Kalinin and D. A. Bonnell. Local potential and polarization screening on ferroelectric surfaces. *Phys. Rev. B*, 63:125411, 2001.

[17] S. V. Kalinin and D. A. Bonnell. Scanning impedance microscopy of an active Schottky barrier diode. *J. Appl. Phys.*, 91(2):832–839, 2002.

[18] J. Shin, V. Meunier, A. P. Baddorf, and S. V. Kalinin. Nonlinear transport imaging by scanning impedance microscopy. *App. Phys. Lett.*, 85(18):4240–4242, 2004.

[19] F. J. Humphreys. Grain and subgrain characterisation by electron backscatter diffraction. *J. Mat. Sci.*, 36:3833–3854, 2001.

[20] A. Nevosad, M. Hofstaetter, M. Wiessner, P. Supancic, and C. Teichert. C-AFM and KPFM approach to investigate the electrical properties of single grain boundaries in ZnO varistor devices. *Proc. of SPIE*, 8626:862618 1–8, 2013.

[21] M. Hofstätter. *Modellieruung des elektrischen Verhaltens von Varistoren.* PhD thesis, Montanuniversitaet Leoben, 2013.

[22] Ü. Özgür, Ya. I. Alivov, C. Liu, A. Teke, M. A. Reshchikov, S. Doğan, V. Avrutin, S.-J. Cho, and H. Morkoç. A comprehensive review of ZnO materials and devices. *J. Appl. Phys.*, 98(4):041301, 2005.

[23] C. Klingshirn, J. Fallert, H. Zhou, J. Sartor, C. Thiele, F. Maier-Flaig, D. Schneider, and H. Kalt. 65 years of ZnO research - old and very recent results. *physica status solidi (b)*, 247(6):1424–1447, 2010.

[24] Y. Sato and T. Yamamoto. Atomic Structures and Electrical Properties of ZnO Grain Boundaries. *J. Am. Ceram. Soc.*, 90:337–357, 2007.

[25] S. Hirose, Y. Yamamoto, and H. Niimi. Effect of local electrical properties on the electrostatic discharge withstand capability of multilayered chip ZnO varistors. *J. of Appl. Phys.*, 104(1):013701, 2008.

[26] G. Blatter and F. Greuter. Electrical breakdown at semiconductor grain boundaries. *Phys. Rev. B*, 34(12):8555–8572, Dec 1986.

[27] K. Mukae. Electrical properties of grain boundaries in ceramic semiconducters. *Key Eng. Mat.*, 125-126:317–330, 1997.

[28] K. Mukae and A. Tanaka. Electronic characterization of single grain boundary in ZnO:Pr varistors . *Ceramics International*, 26(6):645 – 650, 2000.

[29] M. A. Alim, S. Li, F. Liu, and P. Cheng. Electrical barriers in the ZnO varistor grain boundaries. *phys. stat. sol*, 203:410–427, 2006.

[30] G. Blatter and D. Baeriswyl. High-field transport phenomenology: Hot-electron generation at semiconductor interfaces. *Phys. Rev. B*, 36(12):6446–6464, Oct 1987.

[31] Lionel M. Levinson and H. R. Philipp. The physics of metal oxide varistors. *Journal of Applied Physics*, 46(3):1332–1341, 1975.

[32] D. Sarid. *Exploring scanning probe microscopy with MATHEMATICA*. Wiley-VCH Weinheim, 2001.

[33] S. V. Kalinin, M. R. Suchomel, P. K. Davies, and D. A. Bonnell. Potential and Impedance Imaging of Polycrystalline $BiFeO_3$ Ceramics. *J. Am. Ceram. Soc.*, 85:3011–3017, 2002.

[34] L. J. Brillson and Y. Lu. ZnO Schottky barriers and Ohmic contacts. *J. Appl. Phy.*, 109:121301, 2011.

[35] M. v. Heimendahl. *Einführung in die Elektronenmikroskopie*. Vieweg-Verlag, Braunschweig, 1970.

[36] L. Reimer and G. Pfefferkorn. *Raster- Elektronenmikroskopie*. Springer-Verlag Berlin Heidelberg New York, 1973.

[37] Keithley. *Series 2600A System SourceMeter User's Manual*, September 2008.

[38] K. Choi. Growth mechanism of TiN film on dielectric films and the effects on the work function. *Thin Solid Films*, 486:141–144, 2005.

[39] CAPRES A/S. *Micro Four-Point Probe General Application Note.*

[40] T. Ansbæk, D. H. Petersen, O. Hansen, J. B. Larsen, T. M. Hansen, and P. Bøggild. Fundamental size limitations of micro four-point probes. *Microelectron. Eng.*, 86:987 – 990, 2009.

[41] M. Hofstätter, A. Nevosad, C. Teichert, P. Supancic, and R. Danzer. Voltage Polarity Dependent Current Paths through Polycrystalline ZnO Varistors. *J. Eur. Ceram. Soc.*, 33:3473–3476, 2013.

[42] M. Hofstätter and P. Supancic. 3D Netzwerksimulationen von Varistoren mit verschiedenen Korngrößenverteilungen. *Berg- und Hüttenmännische Monatshefte*, 158:206–210, 2013.

[43] D. M Saylor, J. Fridy, B. S El-Dasher, K. Jung, and A. D. Rollett. Statistically Representative Three-Dimensional Microstructures Based on Orthogonal Observation Sections. *Metall. Mater. Trans. A*, 35:1969–1979, 2004.

[44] M. Bartkowiak, G. D. Mahan, F. A. Modine, M. A. Alim, R. Lauf, and A. McMillan. Voronoi network model of ZnO varistors with different types of grain boundaries. *J. Appl. Phys.*, 80(11):6516–6522, 1996.

[45] D. Fernandez-Hevia, J. de Frutos, A. C. Caballero, and J. F. Fernandez. Mott-Schottky behavior of strongly pinned double Schottky barriers and characterization of ceramic varistors. *J. Appl. Phys.*, 92:2890–2898, 2002.

[46] K. Eda, A. Iga, and M. Matsuoka. Degradation mechanism of non-ohmic zinc oxide ceramics. *J. Appl. Phys.*, 51:2678–2684, 1980.

List of Figures

2.1 Wurtzite structure of ZnO with unit cell, tertraeder bonds and lattice parameters. . . . 3
2.2 I-V curve of a MLV device; Note the switching voltage of ∼3.3 V, the leakage and the breakdown region. . . . 4
2.3 Scheme of the multilayer varistor production process after [1, 25]. . . . 5
2.4 Optical micrograph of a cross sectioned and polished MLV specimen. . . 6
2.5 Grain boundary; a) thought experiment when not in contact; b) Barrier formation; c) Barrier with an applied voltage; Φ_B: Barrier height, E_V: Valence band energy, E_C: Conduction band energy, E_{FGB}: Fermi energy at the grain boundary, E_{FG}: Fermi energy of the ZnO grains, d: Depletion layer width, n_t: Trapped electrons; redrawn after [2]. . . . 8
2.6 Scanning electron microscopy images of ZnO varistors; a) Bismuth system (image taken at the ESI); b) Praseodymium system (image taken at the MCL). . . . 9
2.7 Scheme of the conductive AFM setup with an MLV specimen (topography map). . . . 11
2.8 Scheme of the band structure of two different materials to explain the work function ϕ and the contact potential difference (CPD); a) separated materials; b) both materials in contact; c) with an applied bias. . . . 12
2.9 Scheme for the Kelvin probe force microscopy (KPFM) and scanning surface potential microscopy (SSPM) measurement setup. Indicated are the two scan passes and a scheme of the electrical circuit. . . . 13
2.10 Scheme of the scanning impedance microscopy measurement setup. Indicated are two scan passes and a scheme of the electrical circuit. . . . 14
2.11 Scheme of a four-point probe measurement circuit, R_{Sample} is the resistance under investigation, $R_{contact+cable}$ are the cable and contact resistances. 15
2.12 Scheme of an EBSD setup after [19]. . . . 16

3.1 Specimen embedded in resin with the home-made AFM sample holder on the right. 18

3.2 SIM setup at the CNMS; 1: DC source, 2: Frequency generator, 3: Lock-in amplifier, 4: Summing amplifier, 5: Nanonis AFM controler; 21

3.3 M4PP setup; 1: Kleindiek micromanipulator, 2: Keyence digital microscope, 3: CAPRES four-point probes, 4: Keithley 2636A dual source meter; 23

3.4 Scanning electron microscope image of a used micro four-point probe. . . 23

3.5 M4PP probes; a) setup for the measurement of ZnO grain boundaries; b) setup for the measurement of the ZnO - MLV electrode interface 24

4.1 Polished MLV cross section of a sample with 5 μm grain size, a) C-AFM current image measured at 8 V, The maximum current at the electrodes is 10 nA, but to increase the visibility of the ZnO grains the maximum of the color scale was set to 1 nA; b)I-V curve, measured at the grain marked with X. c) EBSD image of the center area. 28

4.2 Polished MLV cross section parallel to the electrode plane; a) Height image; b) C-AFM current image measured at +8 V. 29

4.3 CAFM images of an 5 μm grain size specimen for long time test; a) current image at 5 V; b) I-V curve, measurement point marked with X. 30

4.4 Image of an 8 μm grain size specimen with FIB deposited Pt-Dots; a) SEM image; b) AC-mode height image; c) cross sections 1 and 2 across Pt-Dots; d) cross sections 3 and 4 across pits 31

4.5 Polished MLV cross section; a) AC-mode height image; b) current over time plot at a constant voltage of 50 mV, measured on the electrode with the Keithley 2636A dual source meter. 33

4.6 Macroscopic I-V curve of a MLV device with pronounced asymmetric behavior, measured at the ISFK; Note the switching voltage of $\sim$3.3 V, the leakage and the breakdown region. 34

4.7 Thermography phase image of the sample with asymmetric behavior: The hot-spots are marked with insets from the amplitude image. Arrows indicate the current direction according to the corresponding hot spot. . . . 35

4.8 Polished MLV cross section of the hot spot area, a) AFM height image, b) CPD image, c) EBSD image. 36

4.9 SSPM investigation of the hot spot area; a) SSPM image with −1 V bias applied; b) SSPM image with +1 V bias applied; c) cross sections at lines 1 and 2 at −1 V; d) cross sections at lines 1 and 2 at +1 V; e) cross sections at line 3, both directions; f) cross sections at line 4, both directions. . . . 37

4.10 KPFM and SSPM study of a sample with 5 µm grain size; a) Height image; b) CPD map; 3D SSPM profile at + 8 V applied 38

4.11 Equivalent circuit model of a grain boundary. 39

4.12 Compilation of SIM measurements with frequencies and external nominally applied voltages. 41

4.13 SIM measurements at 0V, 20 kHz; a) heigt image; b) SIM amplitude; c) SIM phase; d) EBSD map of the same area; The numbers indicate the investigated ZnO grains. 43

4.14 SSPM measurements of the area which was investigated by SIM with indicated ZnO grains; a) height image; b) CDP map; c) SSPM measurement at −1 V; d) SSPM measurement at +1 V; 44

4.15 Local SIM amplitudes as function of frequency (ω) and DC bias; a) grain 11; b) grain 13; c) grain 14; d) grain 15. 46

4.16 V_{ACloc} plotted over external DC bias and AC frequency; a) V_{ACloc} grain 13; b) V_{ACloc} grain 14; c) V_{ACloc} difference between grains 13 and 14. . . . 47

4.17 Simulated M4PP measurement; a) relative current flow at 2.2 V; b) relative current flow at 3.4 V; c) simulated I-V characteristics for the investigated GB and the entire ensemble in a double logarithmic plot. 50

4.18 One of the samples used for the M4PP investigation; a) Stitched optical micrograph with a termination on the left end and a horizontal electrode in the middle; b) EBSD map of the same area. The locations of three particular grain boundaries are indicated. 51

4.19 M4PP measured I-V curves of the three exemplary grain boundaries, indicated in Fig. 4.18: a) GB 01 with indication of the parameters for the statistical analysis; b) GB 31; c) GB 36. 53

4.20 Histogram of slopes in region I (41 GBs ⇒ 82 curves). 54

4.21 Plots of the values at the point of breakdown: a) Histogram of the breakdown voltage V_{BD}; b) Histogram of the current at breakdown I_{BD}; c) Current at breakdown I_{BD} over breakdown voltage V_{BD} (current scales are logarithmic). 55

4.22 Plots of the values at the first kink: a) Histogram of the voltage $V_{\beta-\gamma}$; b) Histogram of the current $I_{\beta-\gamma}$; c) Current $I_{\beta-\gamma}$ over voltage $V_{\beta-\gamma}$ (current plotted in logarithmic scale). 56
4.23 Histogram of slopes extracted from the two linear regions in the log-log plots (high resistive regime); a) region II; b) region III (41 GBs). 57
4.24 I - V curves of two exemplary ZnO to MLV electrode interfaces; a) Ohmic and symmetric behavior; b) nonlinear and asymmetric behavior. 57
4.25 C-AFM investigation of a Bi system sample; a) height image; b) current image at $+8$ V. 58
4.26 Photolithographic deposited Ag-dots; a) optical microscopy image; b) height image; c) cross section 1; d) cross section 2. 59
4.27 KPFM and SSPM investigation of an Bi doped specimen; a) height image; b) CPD map; c) SSPM map at -8 V; d) SSPM map at $+8$ V; e) cross sections from c) and d) 60

List of Tables

3.1 Limits of the Keithley 2636A dual source meter [37]; 18

4.1 External applied voltage, measured currents and calculated bias at the varistor. 42

List of abbreviations

AFM	atomic force microscopy
Bi	bismuth
C-AFM	conductive atomic force microscopy
CPD	contact potential difference
EBSD	electron backscatter difffraction
ESI	Erich Schmidt Institut, Leoben
FIB	focused ion beam
GB	grain boundary
I_{BD}	current at barrier breakdown
$I_{\beta-\gamma}$	current at point between region two and three
ISFK	Institut für Struktur- und Funktionskeramik, Leoben
I-V	current-to-voltage
KPFM	Kelvin probe force microscopy
M4PP	micro four-point probe
MCL	Materials Center Leoben
MLV	multy layer varistor
Pr	praseodymium
SEM	scanning electron microscopy
SIM	scanning impedance microscopy
SSPM	scanning surface potential microscopy
V_{BD}	voltage at barrier breakdown
$V_{\beta-\gamma}$	voltage at point between region two and three
ZnO	zinc oxide

Acknowledgements

I am very grateful to my supervisor **Prof. Christian Teichert** for providing me the possibility to work on this thesis and his great support during the last three years.

I would like to express my very great appreciation to all the people from whom I received a lot of help in different needs throughout my work on this thesis.

Special thanks to:

Dr. Markus Kratzer for his support with knowledge and expertise in many concerns and for being a pleasant office-mate during all the time. Also **Dipl. Ing. Christian Ganser**, **Dipl. Ing. Quan Shen**, **Dipl. Ing. Stefan Lorbek**, **Dr. Igor Beinik**, **Dr. Franz Schmied**, **Mgr inz. Monika Mirkovska** and the other staff of the physics departement for friendship and help;

Heide Kirchberger and **Magdalena Ottrin** for helping me in all administrative matters and other needs;

Ing. Heinz Pirker and **Peter Moharitsch** for their expertise in many technical problems;

The other project members from ISFK, the project leader **Prof. Peter Supancic**, my co-PhD-student **Dipl. Ing. Michael Hofstätter** and **Prof. Robert Danzer** for their great support;

The staff of the Institut für Struktur- und Funktionskeramik with special thank to **Dipl. Ing. Irirna Karelova** for her support in sample preparation;

Dr. Manfred Wießner and **Dipl. Ing. Tamara Teppernegg** for EBSD measurements;

Dr. Sergej Kalinin and **Dr. Evgheni Strelcov** and the other staff of the CNMS in Tennessee, USA, for the opportunity to visit their institute and support during the stay;

Prof. Antonin Fejfar and **Dr. Aliaksei Vetushka** for their kind hospitality and support during my stays at the Institute of Physics, Academy of Sciences, Prague Czech Republic;

The members of EPCOS Deutschlandsberg with special thanks to **Dr. Christoph Auer**, **Dr. Monika Piber** and **Dr. Andreas Bürgermeister** for their input and provision with samples and knowledge;

And finally the Austrian FFG for financially supporting this work under bridge project # 24890 "Zusammenhang zwischen dem Mikrogefüge und den makroskopischen, elektrischen Eigenschaften von Zinkoxid-Varistoren".

List of Publications

T. Griesser, S. V. Radl, T. Koepplmayr, A. Wolfberger, M. Edler, **A. Pavitschitz**, M. Kratzer, C. Teichert, T. Rath, G. Trimmel, G. Schwabegger, C. Simbrunner, H. Sitter, W. Kern. UV-induced modulation of the conductivity of polyaniline : towards a photo-patternable charge injection layer for structured organic light emitting diodes. *J. Mater. Chem.*, 22:2922-2928, 2012

B. Vasić, M. Kratzer, A. Matković, **A. Nevosad**, U. Ralević, D. Jovanović, C. Ganser, C. Teichert, R. Gajić. Atomic force microscopy based manipulation of graphene using dynamic plowing lithography. *Nanotechnology*, 24:015303, 2013

A. Nevosad, M. Hofstätter, M. Wiessner, P. Supancic, C. Teichert. C-AFM and KPFM approach to investigate the electrical properties of single grain boundaries in ZnO varistor devices. *Proc. of SPIE*, 8626:862618 1-8, 2013

M. Hofstätter, **A. Nevosad**, C. Teichert, P. Supancic, R. Danzer. Voltage Polarity Depended Current Paths through Polycrystalline ZnO Varistors. *J. Eur. Ceram. Soc.*, 33:3473-3476, 2013

2.2 ZnO varistor ceramics

A varistor is a passive electronic device with a highly nonlinear current-voltage (I-V) behavior. The I-V characteristics can be described by a power law:

$$I = \left(\frac{V}{C}\right)^{\alpha} \tag{2.1}$$

where I is the current through the device, V the applied voltage, C a constant, and α the nonlinearity exponent. A value of $\alpha = 1$ would result in an Ohmic resistor and $\alpha = \infty$ would result in an ideal varistor.

Fig. 2.2 shows the I-V behavior of a MLV device with a small number of GBs between the electrodes. The switching voltage at $\sim$3 V, the leakage region below switching, and the breakdown region at higher voltages are marked. The highly nonlinear effect in varistor ceramics is caused by the formation of electrical barriers at the ZnO grain boundaries. The nature of these barriers is described in section 2.2.2. The formation of these barriers is triggered by specific dopants. The two important ZnO varistor systems are distinguished by their main doping element, which are on the one hand Bismuth (Bi) doped systems and Praseodymium (Pr) doped systems on the other. The effects of these elements and other dopants which are important for technical varistor ceramics are described in section 2.2.3.

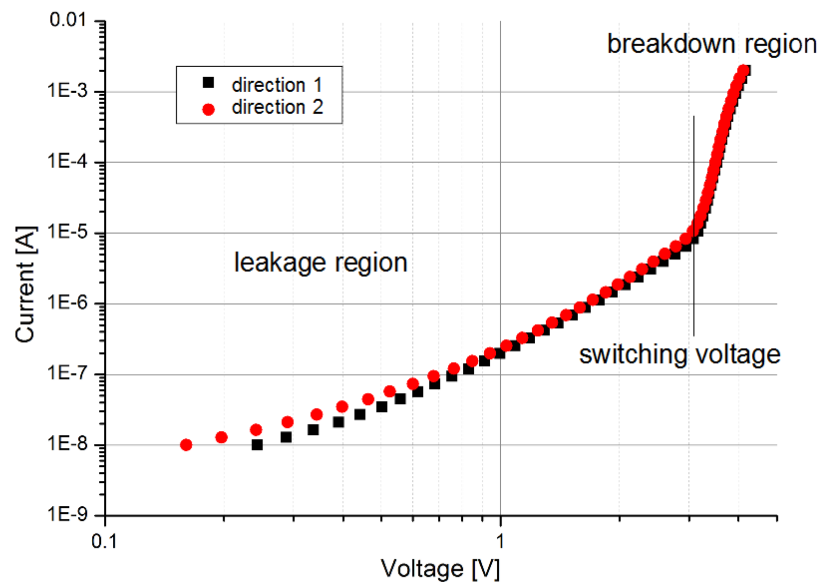

Figure 2.2: I-V curve of a MLV device; Note the switching voltage of $\sim$3.3 V, the leakage and the breakdown region.

lead to varistor behavior [24]. The Pr systems form a uniform microstructure without pronounced additional phases or twinning, as can be seen in Fig. 2.6 b). Varistors containing Pr_6O_{11} show a higher capability to withstand electrostatic discharges whereas those with Bi_2O_3 better handle constant surges [25]. The fabrication of varistor devices with highly non-ohmic behavior requires further dopants or additives.

Other dopants are transition elements like cobalt and manganese which go into solution in the ZnO and increase the achievable α exponent by the formation of interface states and deep bulk traps. Aluminum increases the grain conductivity as it acts as a donor in ZnO. Antimony and silicon are grain growth inhibitors in Bi systems through the formation of spinel and pyrochlore phases [5]. Antimony further improves the I-V characteristics and the stability against electrical stress. Sb also promotes the formation of twins in the ZnO grains which are unit cell thick layers of the n-type semiconductor zinc antimonate spinel ($Zn_7Sb_2O_{12}$). On the other hand, TiO_2 and BeO promote the grain growth. Additionally, dopants which mainly control the grain growth also affect the potential barrier formation at the GB [2, 3].

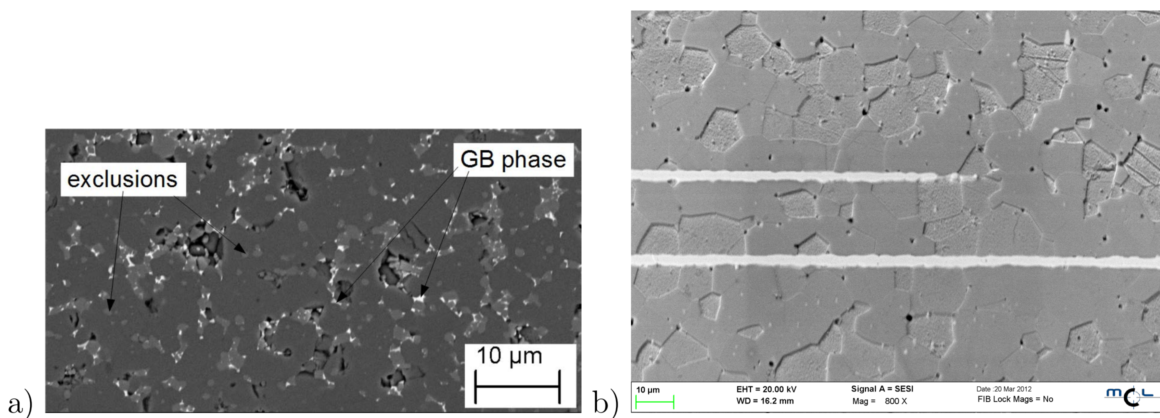

Figure 2.6: Scanning electron microscopy images of ZnO varistors; a) Bismuth system (image taken at the ESI); b) Praseodymium system (image taken at the MCL).

The electrical properties of single spots can be investigated by keeping the AFM-tip on a certain position and applying a voltage ramp to measure a local current-voltage (I - V) curve. Since C-AFM requires a constant electrical contact between the AFM tip and the specimen surface, electrically conductive AFM probes and scanning in contact mode are necessary.

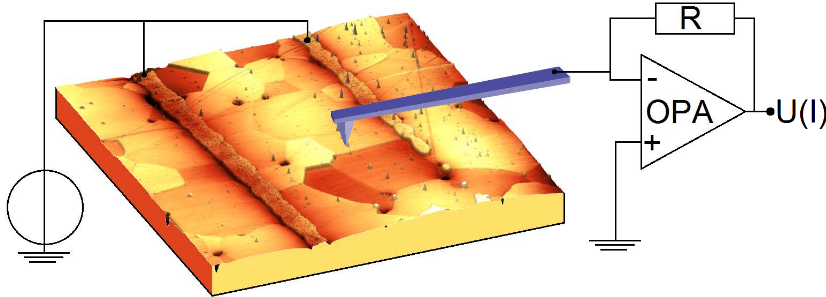

Figure 2.7: Scheme of the conductive AFM setup with an MLV specimen (topography map).

2.3.2 Kelvin probe force microscopy and scanning surface potential microscopy

Kelvin probe force microscopy (KPFM) is a method to map the local contact potential difference (CPD) [12]. The CPD is the difference in work function between two materials. The physical principle of the CPD between two materials is illustrated in Fig. 2.8. One material is considered as that of the tip with the Fermi energy E_{F_Tip} and the work function ϕ_{Tip} the other one represents that of the sample with the Fermi energy E_{F_S} and the work function ϕ_S. E_{Vac} is the local vacuum energy level. In the first image the two materials are in distance without any interaction. In contact (second scheme) the Fermi energies E_{F_Tip} and E_{F_S} align by charge transfer and the local vacuum energy E_{Vac} is shifted by the potential V_{CPD}. Due to the charge transfer an electrostatic filed is established between the two materials which also causes an electrostatic force. In the third image a voltage with the value of the CPD is applied between tip and sample. This compensates the electrostatic field and therefore also the electrostatic force.

This principle is used in KPFM for the measurement of the local contact potential difference between the conductive AFM tip and the sample surface [12]. A scheme for the measurement is displayed in Fig. 2.9. KPFM and SSPM require electrically

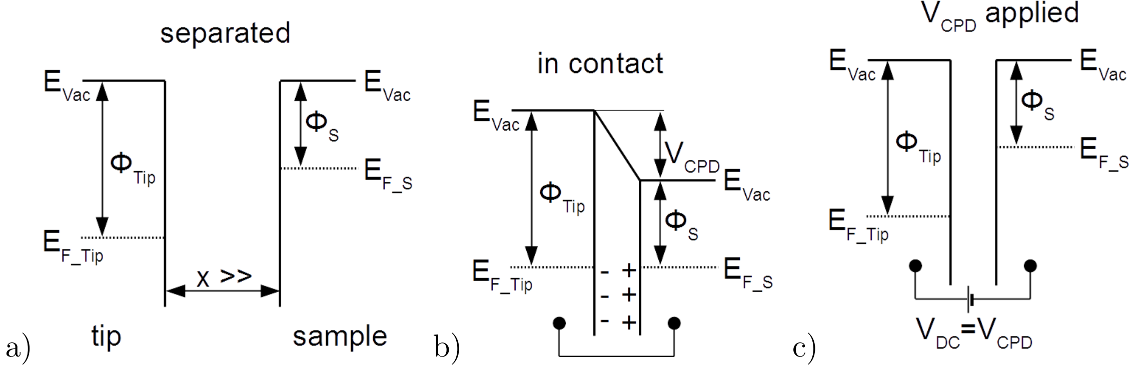

Figure 2.8: Scheme of the band structure of two different materials to explain the work function ϕ and the contact potential difference (CPD); a) separated materials; b) both materials in contact; c) with an applied bias.

conductive probes since a potential has to be applied to the tip. During the first pass the surface topography is measured in AC mode. In the second pass the tip follows the surface topography in close proximity ($\sim 5\,\mathrm{nm}$). During this second pass, an AC and a DC voltage is applied between tip and sample. This electric field excites the cantilever to oscillations via a force as is described in equation 2.7.

$$F = \frac{1}{2}\frac{dC}{dz}\left((V_{DC} - \Delta\Phi)^2 + 2(V_{DC} - \Delta\Phi)V_{AC} * cos(\omega t) + \frac{1}{2}V_{AC}^2 * cos(2\omega t)\right) \tag{2.7}$$

where V_{AC} is the AC voltage with a frequency close to the resonance frequency of the cantilever, V_{DC} is the externally applied DC voltage to suppress the cantilever oscillation, $\Delta\Phi$ is the CPD, and ω is the circular frequency of the cantilever oscillation.

In the second term of equation 2.7 it can be recognized that the first harmonic component of the electrostatic force, and therefore the oscillation of the cantilever, is nullified if the applied DC bias, V_{DC}, is equal to the CPD. A feedback loop adjusts the DC bias constantly to suppress the first order of cantilever oscillations and the DC voltage is recorded as the CPD signal [12, 13]. The CPD is mainly the difference in work-function between the tip and the sample material, but is also influenced by factors like the presence of a water film and the local surface roughness.

Scanning surface potential microscopy (SSPM) is a variant of KPFM where an additional bias is applied across the specimen. Measuring KPFM on a such biased sample results

in a map of the potential distribution on the surface plus the CPD. From the measured surface potential distribution, DC transport properties can be derived [33].

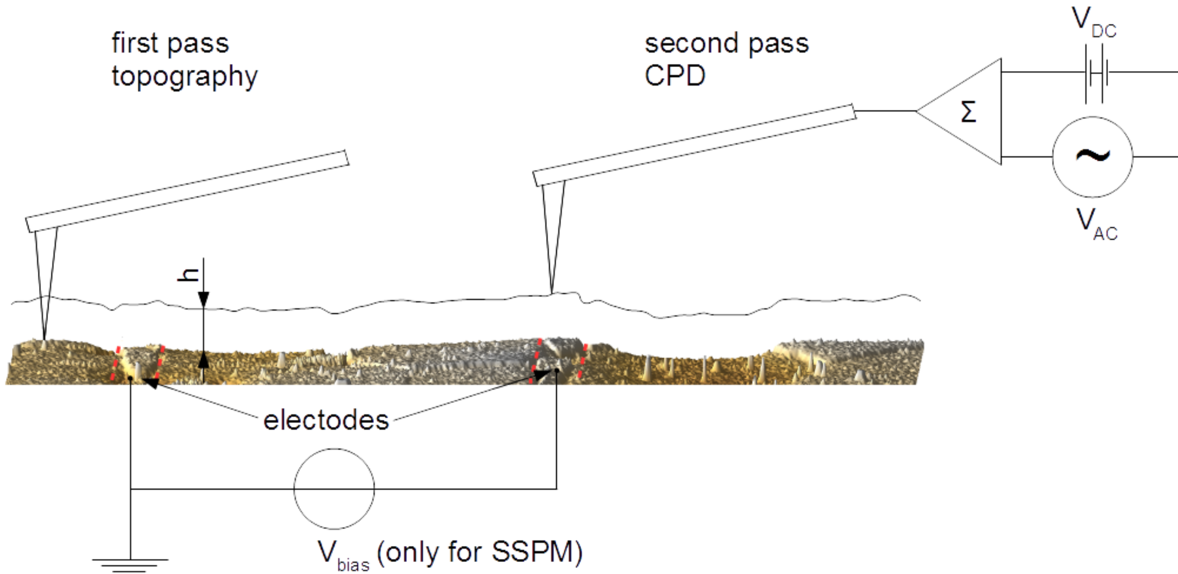

Figure 2.9: Scheme for the Kelvin probe force microscopy (KPFM) and scanning surface potential microscopy (SSPM) measurement setup. Indicated are the two scan passes and a scheme of the electrical circuit.

2.3.3 Scanning impedance microscopy

Scanning impedance microscopy (SIM) is a method similar to SSPM since it is also a two pass technique and voltages are applied to the AFM probe and across the sample as illustrated in Fig. 2.10 [16, 17]. SIM also requires conductive or with a conductive material coated AFM probes. Like in KPFM and SSPM the surface topography is mapped in the first pass of a scan-line. The main difference is that in SSPM a DC bias is applied across the sample and an AC + DC voltage is applied to the probe, whereas in SIM an AC + DC bias is applied across the specimen and a DC voltage to the AFM probe. The DC voltage at the probe is used to increase the electrostatic interaction between tip and sample and therefore the contrast of the image. In the second pass, the cantilever is excited to oscillations by the field between tip and sample surface with a force similar to the one described in Eq. 2.7. The amplitude of these oscillations is measured with a lock-in amplifier and allows to calculate the local AC voltage at

the sample surface. A set of measurements at different excitation frequencies allows to calculate local AC transport parameters [18, 33].

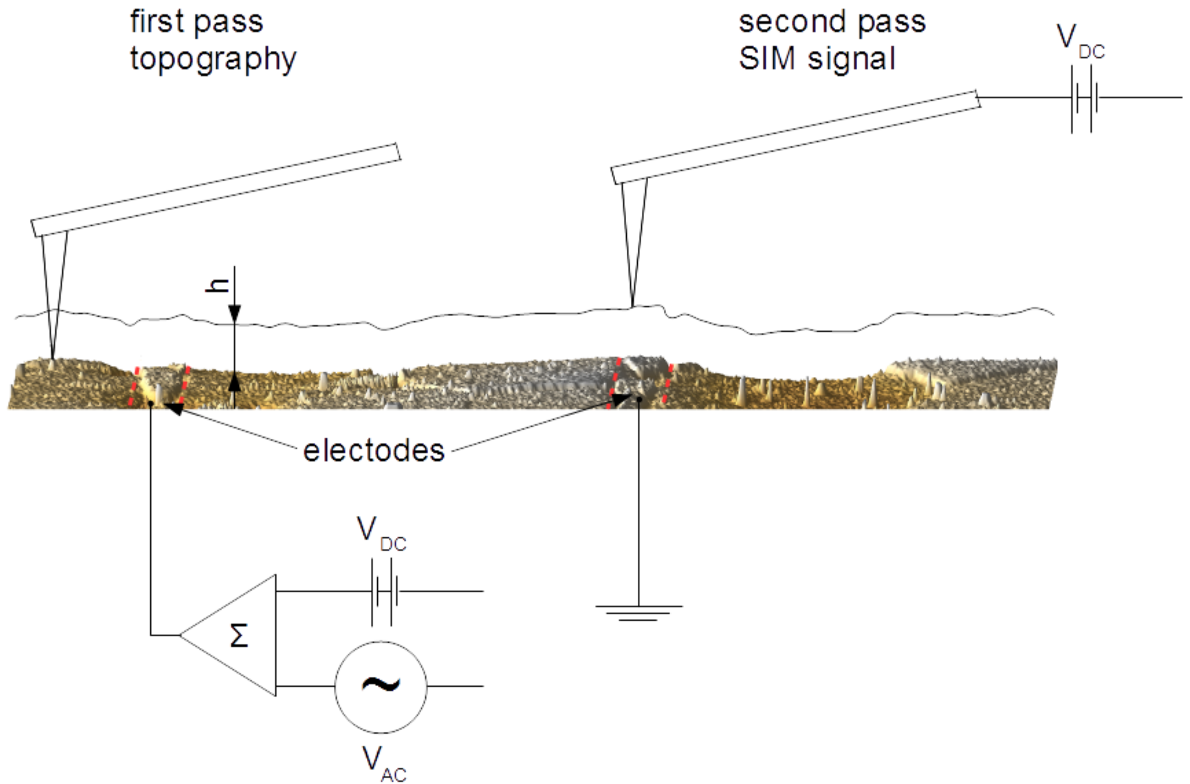

Figure 2.10: Scheme of the scanning impedance microscopy measurement setup. Indicated are two scan passes and a scheme of the electrical circuit.

2.4 Four-point probe

The measurement of resistances in a two-point setup is always influenced by the resistances of the cables and contact properties between the sample and the probe. Since semiconductor surfaces are forming Schottky barriers between a metallic probe and sample surface, they are strongly influencing the measured resistance [34]. A four-point measurement setup (see Fig. 2.11) can overcome these limitations by separating the measurement of current and potential. In four-point measurements, a voltage is applied and the current is measured, or a known current is applied between two probes and the voltage drop is measured current free between the two other probes. The current free

measurement makes the potential measurement independent of contact properties and cable resistances.

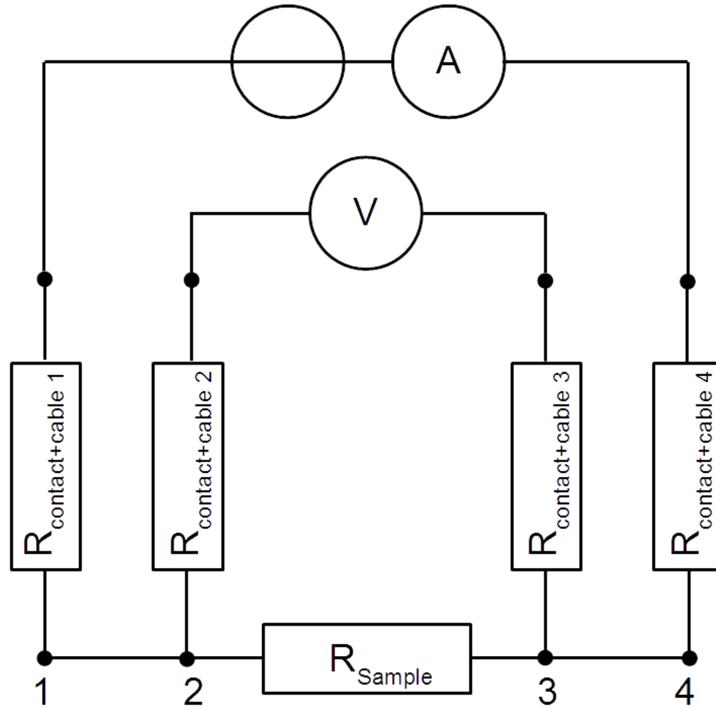

Figure 2.11: Scheme of a four-point probe measurement circuit, R_{Sample} is the resistance under investigation, $R_{\text{contact+cable}}$ are the cable and contact resistances.

Conventional four-point measurement setups use four independent macroscopic probes which are separately placed on the sample surface. This requires to manipulate four probes and a certain available area on the sample. A micro four-point probe, which is described in Sec. 3.4, allows to place all four probes at once on a limited space in a well defined distance in the micrometer range.

2.5 Electron backscatter diffraction

Electron backscatter diffraction (EBSD) is implemented in scanning electron microscopes (SEM) to map the crystallographic orientations at the sample surface. The principle of the EBSD measurement is depicted in Fig 2.12. The electrons of the primary beam propagate into the sample material and are inelastically scattered. This forms a cone of diffusely scattered electrons which are scattered at the lattice planes in the specimen if

as needed for M4PP. The vibro-polishing for the AFM images was done for 10 minutes without any load on the samples. All grinding and polishing have to be done as gentle as possible, since too much force will cause breakouts of the microstructure in the sample. The residuals from polishing have to be removed after every polishing step by thorough cleaning with a paper tissue under water. Finally the samples should be rinsed with distilled water.

The AFM specimen holder in Fig 3.1 on the right was manufactured from stainless steel to ensure a correct parallel alignment and stable fixation during AFM measurements. A similar holder was made for the M4PP investigations.

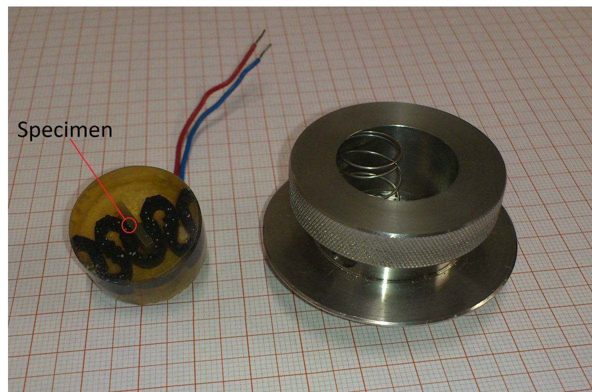

Figure 3.1: Specimen embedded in resin with the home-made AFM sample holder on the right.

3.2 Keithley 2636A dual source meter

All M4PP and some C-AFM measurements were performed employing a Keithley 2636A dual source meter. This instrument features two independent source and measuring units in one device. The parameters of the device are listed in Table 3.1.

Function	Capabilities
Source DC voltage	1 µV to 202 V
Source DC current	20 fA to 1.515 A
Measure DC current	1 µV to 204 V
Measure DC current	1 fA to 1.53 A

Table 3.1: Limits of the Keithley 2636A dual source meter [37];

A Photograph of the setup is displayed in Fig. 3.2. As lock-in amplifier, a Stanford research SR844 with a lock-in range from 25 kHz to 200 MHz was employed. For SIM measurements a AC plus a DC voltage have to be applied to the sample. The AC voltage was provided by the internal frequency generator, the DC voltage was taken from a National Instruments board and both voltages were added by a summing amplifier. The current through the sample was measured with a current to voltage amplifier and read out by a National Instruments board.

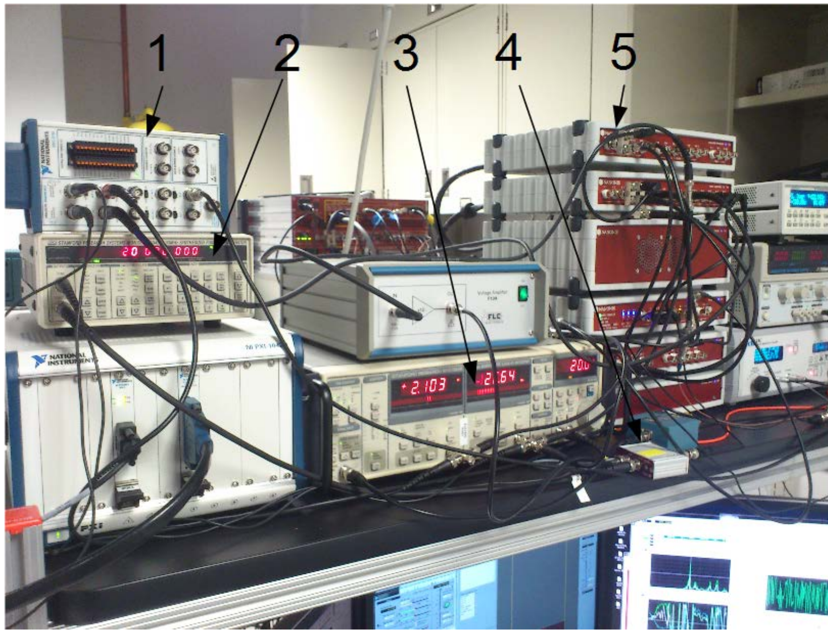

Figure 3.2: SIM setup at the CNMS; 1: DC source, 2: Frequency generator, 3: Lock-in amplifier, 4: Summing amplifier, 5: Nanonis AFM controler;

3.4 Micro four-point probe

Micro four-point probe (M4PP) allows to perform four-point probe investigations on micrometer sized structures with the probes placed in one row in close proximity. The setup for the M4PP measurements with the employed Keyence digital microscope and Kleindiek micromanipulator is shown in Fig. 3.3. All M4PP measurements were performed with probes from CAPRES which are displayed in Fig. 3.4. The probes are four flat, 25 µm long, 1 µthick and 3 µm wide, gold coated silicon cantilevers with a typical spring constant of 5 N/m. They are mounted on a silicon chip in a center to center distance of 5 µm [39]. These probes require a ZnO grain diameter of at least 8 µm

A home built interface box was used as link between the CAPRES system and the Keithley connectors. The connection between the Keithley and the box was realized with home-made triax-to-coax cables.

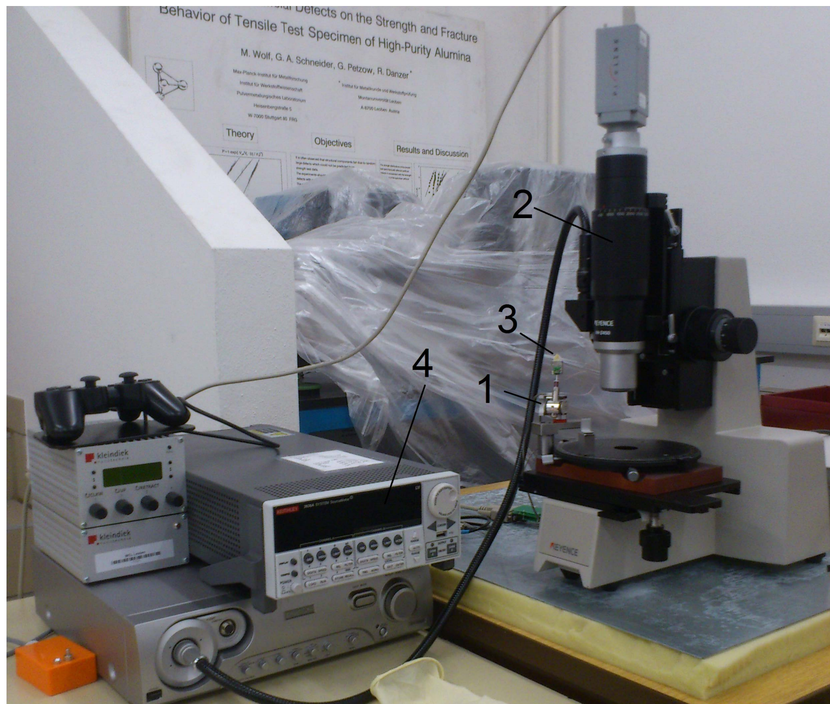

Figure 3.3: M4PP setup; 1: Kleindiek micromanipulator, 2: Keyence digital microscope, 3: CAPRES four-point probes, 4: Keithley 2636A dual source meter;

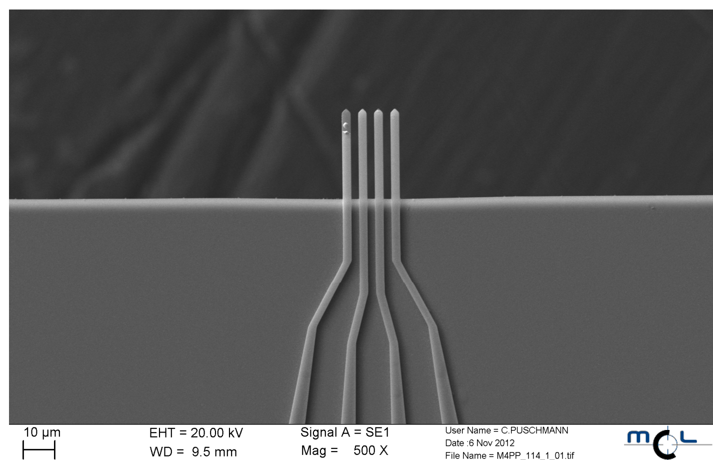

Figure 3.4: Scanning electron microscope image of a used micro four-point probe.

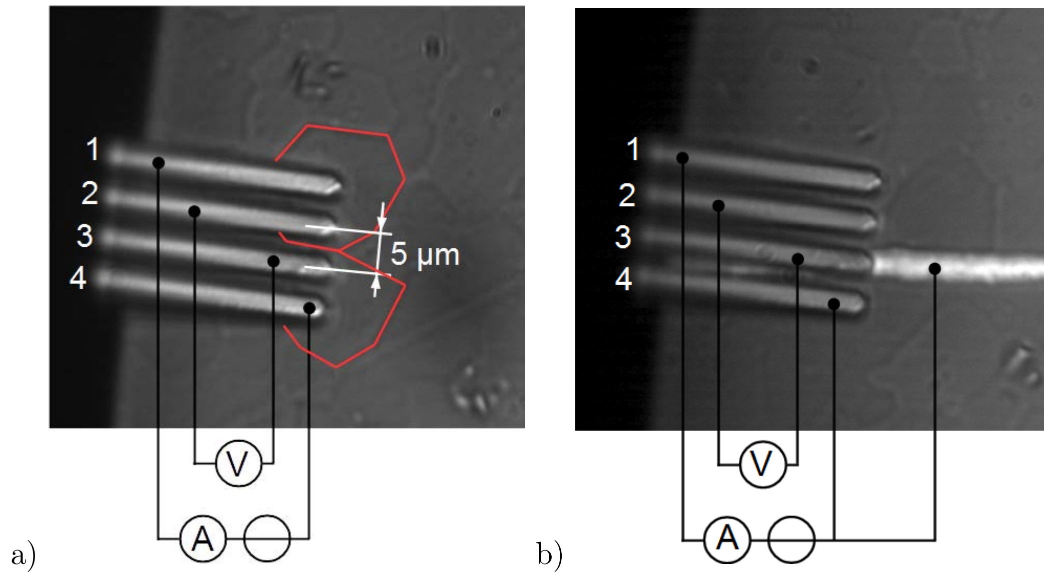

Figure 3.5: M4PP probes; a) setup for the measurement of ZnO grain boundaries; b) setup for the measurement of the ZnO - MLV electrode interface

3.5 Electron backscatter diffraction

The EBSD measurements were done on a Zeiss Auriga system at the MCL and a LEO 1525 system at the ESI. Both systems were equipped with an EDAX EBSD detector.

The electron beam in a scanning electron microscope causes a deposition of carbon on the sample surface. This carbon forms a conductive layer on the surface which spoils all electrical measurements like C-AFM and M4PP and also surface workfunction sensitive techniques like KPFM and SSPM. Therefore, EBSD has to be employed as last technique, after all AFM and M4PP measurements are finished. A gentle polishing after EBSD can be done to removes the carbon layer, but also some of the sample surface material is removed which might change the appearance of the grains at the surface.

Most of the presented samples were embedded in a non-conductive resin. The large volume of the resin cylinder gets electrostatically charged and is heated up under the electron beam of the SEM. The electrostatic charge causes a deflection of the electron beam and the temperature change causes thermal drift of the sample. These effects can strongly distort the measured orientation map. Therefore, the resin block has to be properly shielded with silver paint and copper tape to reduce these effects. As alternative

The C-AFM scans on Pr-system samples exhibited no non-conductive other phases in the microstructure as expected for this system.

The I-V curve presented in Fig. 4.1 b) was measured at the grain marked by a green X in the current image and the EBSD map. This curve is similar to others measured at the first row of ZnO grains next to the electrode. It shows an asymmetric, non linear behavior for positive and negative applied voltages. The breakdown voltage for applied positive voltages is nearly 10 V and −5 V for negative voltages. Consecutive measurements of I-V curves at the same point yielded deviating breakdown characteristics and runaway values. This indicates uncontrollable electrical changes and unstable mechanical contact properties during the measurements. A general problem in all C-AFM measurements was the non Ohmic contact resistance between the AFM tip and the sample [34]. The EBSD measurement in Fig. 4.1 c) was performed to illustrate the individual ZnO grains. The electrodes can be recognized as black stripes in the EBSD map.

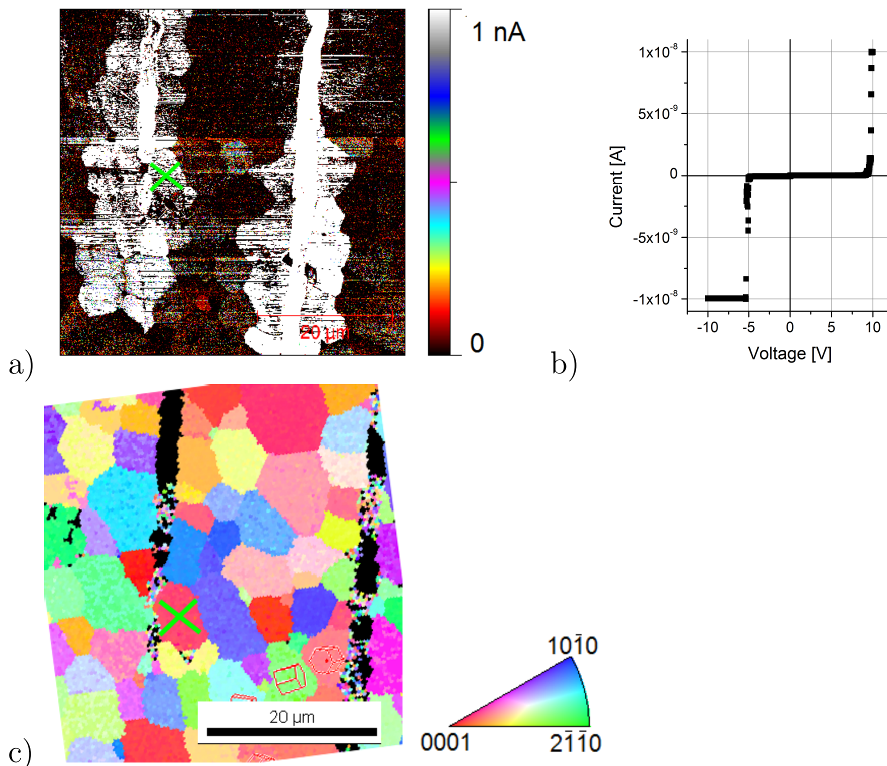

Figure 4.1: Polished MLV cross section of a sample with 5 µm grain size, a) C-AFM current image measured at 8 V, The maximum current at the electrodes is 10 nA, but to increase the visibility of the ZnO grains the maximum of the color scale was set to 1 nA; b)I-V curve, measured at the grain marked with X. c) EBSD image of the center area.

Wedge

In a normal cross section, the current is flowing from the AFM tip on top of the ZnO grain to the metallic electrode which is on the side of the grain. Since the crystallographic orientation is might influencing the electrical properties, a setup is required where only one crystallographic orientation is contributing. Therefore, a structure was realized where the ZnO is on top of the conductive electrode and the current goes straight through the ZnO.

The 5 µm grain size sample, presented in Fig. 4.2, was prepared in a way that the cross sectioning by grinding and polishing was made parallel to the MLV electrode plane. This resulted a single grain thin wedge of ZnO ceramic material with one of the electrodes underneath. The individual grains are clearly visible in the height image in Fig. 4.2 a). The current image (Fig. 4.2 b)) was measured at a bias of +8 V. Several areas in the image appear as stripes where no current was measured. The conductive and non conductive areas cannot be correlated with the topographic features in the height image. This effect might have been caused by an additional layer of ZnO grains underneath or by a very thin film of residuals from polishing on the sample surface.

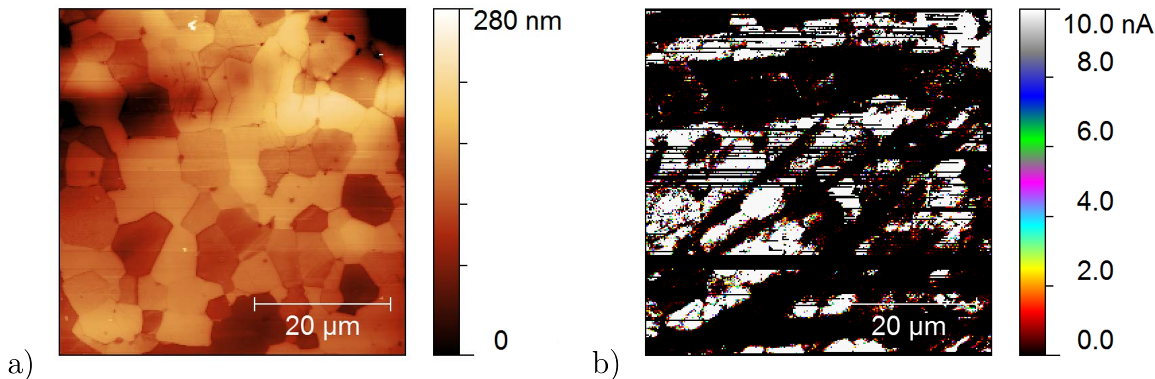

Figure 4.2: Polished MLV cross section parallel to the electrode plane; a) Height image; b) C-AFM current image measured at +8 V.

Long time test

To determine a change in the electrical properties of prepared sample surfaces over time, a set of grains on one polished sample was chosen. I-V curve measurements on these grains were repeated for four days. Fig. 4.3 shows a current map of the investigated area

in a) and the curves for the spot marked with X recorded at four subsequent days in b). The measured curves showed no significant changes after the period of four days. The observed changes in the curves can not be related to the time period.

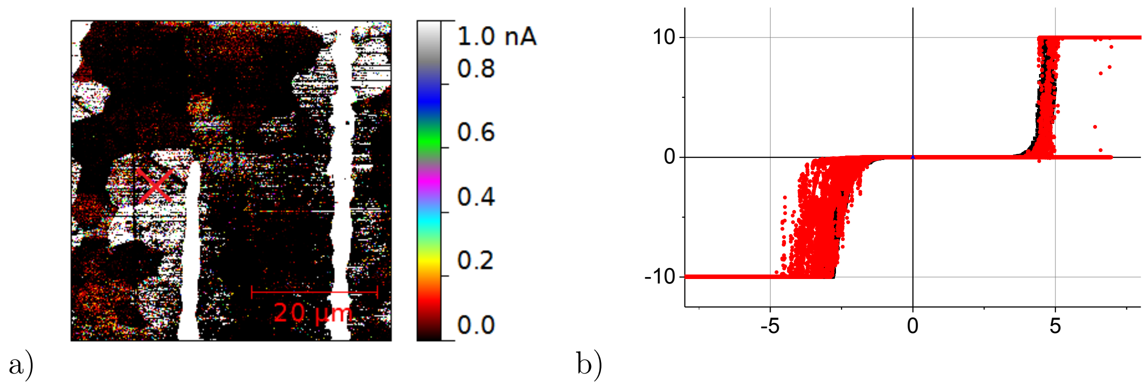

Figure 4.3: CAFM images of an 5 µm grain size specimen for long time test; a) current image at 5 V; b) I-V curve, measurement point marked with X.

Platinum deposition by focused ion beam

The previously presented C-AFM investigations showed instable and asymmetric contact properties. The deposition of platinum structures was made as an approach to increase the contact stability and to achieve Ohmic contacts between the AFM tip and the ZnO surface. The SEM image of a MLV cross section with deposited Pt pads is shown in Fig. 4.4 a). The Pt was deposited with a focused ion beam system by cracking a metallorganic gas under the ion beam. The system allowed a precise positioning of the pads within chosen ZnO grains. Fig. 4.4 b) shows an AFM height image. The white rectangles along lines 1 and 2 represent successfully deposited Pt pads. Whereas the black rectangles on the lines 3 and 4 are holes which were burnt into the sample surface by the ion beam because of improper ion acceleration voltages and currents. From the cross sections in Fig. 4.4 c) and d), a height of the dots between 200 nm and 300 nm and a depth of the holes of about 250 nm can be seen. Drawback of the deposition via a focused ion beam method is the deposition of a thin carbon film on the specimen, as it happened after all scanning electron microscopy investigations. This makes the entire surface conductive and prohibits meaningful electrical measurements. Therefore this approach was not further pursued.

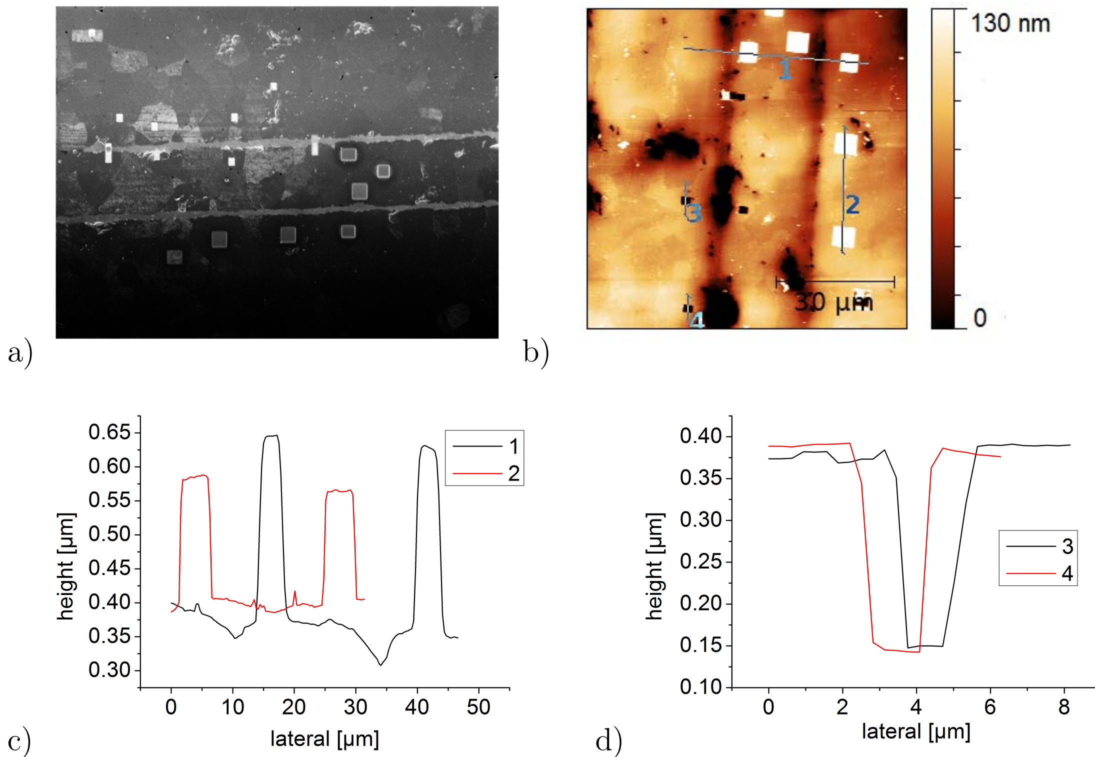

Figure 4.4: Image of an 8 µm grain size specimen with FIB deposited Pt-Dots; a) SEM image; b) AC-mode height image; c) cross sections 1 and 2 across Pt-Dots; d) cross sections 3 and 4 across pits

C-AFM measurements with the Keithley 2636A dual source meter

In the following, electrical measurements performed with the Keithley 2636A dual source meter will be reported. This device allows to apply and measure currents in a wider range than the original AFM current to voltage amplifier (Orca-Module) (see section 3.2). Moreover it enables measurements over longer timescales. The image in Fig. 4.5 a) shows a height image of a MLV specimen which was measured with a diamond coated DCP11 probe in AC mode to reduce wear of the tip and to prove the possibility of AC mode imaging with subsequent local electrical measurements. After the height imaging several I-V curves were measured by placing the tip on one spot and switching the system to contact mode. The diagram in Fig. 4.5 b) is a current-over-time plot with a constant voltage of 50 mV applied to the probe. Two curves were measured at one spot on an Ag/Pd electrode with two different deflection setpoints of 0.5 V and 5 V. The deflection setpoint determines the applied force between probe and sample. A setpoint of 0.5 V represents a usual value for contact mode measurements with the employed DCP11

It has to be noted that only a few tens atoms create the contact between the AFM tip and the sample surface. Therefore, these changes are contributed to a change in the atomic contact properties due to a temperature increase in the contact area and to thermal drift of the sample.

The third curve was measurement with a 10 MΩ resistor which was clamped in the AFM chip holder instead of the probe. The other contact was made with the triax to alligator clips cable which was also used for connection with the MLV specimen. This measurement was performed to test the electric noise inside the AFM box. Also, the piezoelectric actuators of the AFM were active during this measurement. The measured signal showed no noise caused by local electric fields which means an excellent shielding of the AFM and no influence of the AFM electronics on the measured signal.

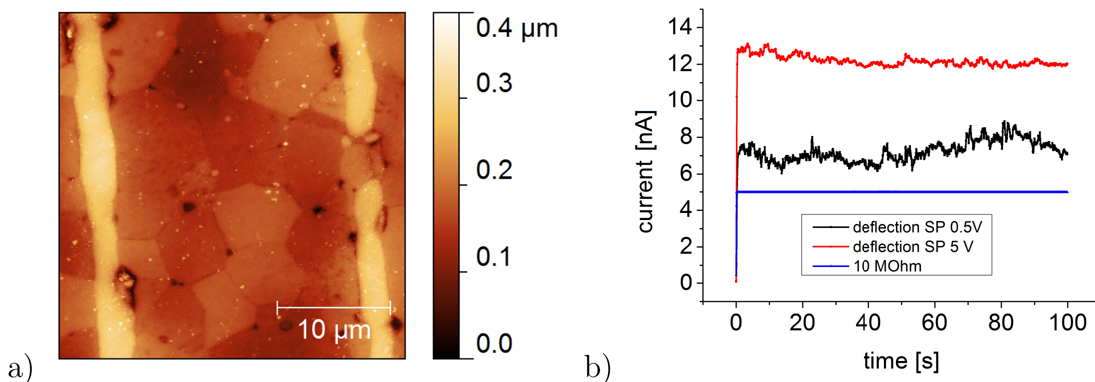

Figure 4.5: Polished MLV cross section; a) AC-mode height image; b) current over time plot at a constant voltage of 50 mV, measured on the electrode with the Keithley 2636A dual source meter.

4.1.2 KPFM and SSPM investigations

KPFM and SSPM investigation of an hot spot area

The macroscopic behavior of a set of low switching voltage MLV samples with a grain size of 8 µm and one pair of electrodes in a distance of 20 µm was investigated. From this set, a specimen with pronounced asymmetric macroscopic I-V characteristics was chosen for further investigation. The I-V curve of this sample is displayed in a double logarithmic plot in Fig. 4.6. FWD, which means forward direction and BWD, which means backward direction, are arbitrary notations for the direction of current flow. In

this measurement always a positive voltage was applied to one of the electrodes, the other one was grounded. To change the direction the electrodes were changed. The FWD and BWD curves do not deviate much in their switching voltage, but the current in the leakage region for the BWD curve is significantly higher. Assumption for this behavior was the formation of a preferred current path for one direction of the applied bias and therefore an asymmetric behavior. To detect this current path, an iterative process of grinding and subsequent lock-in thermography were employed. In lock-in thermography two hot spots, one for every bias direction, were found. Finally, one of the hot spots was located at the sample surface. One phase image of the thermography measurement with insets from the amplitude image is shown in Fig. 4.7. The white arrows in the image indicate the direction of current flow. Unfortunately, the hot spot on the left, for BWD direction, was lost for further investigation during polishing. The area of the right hot spot was further investigated with KPFM, SSPM, and EBSD [20, 41].

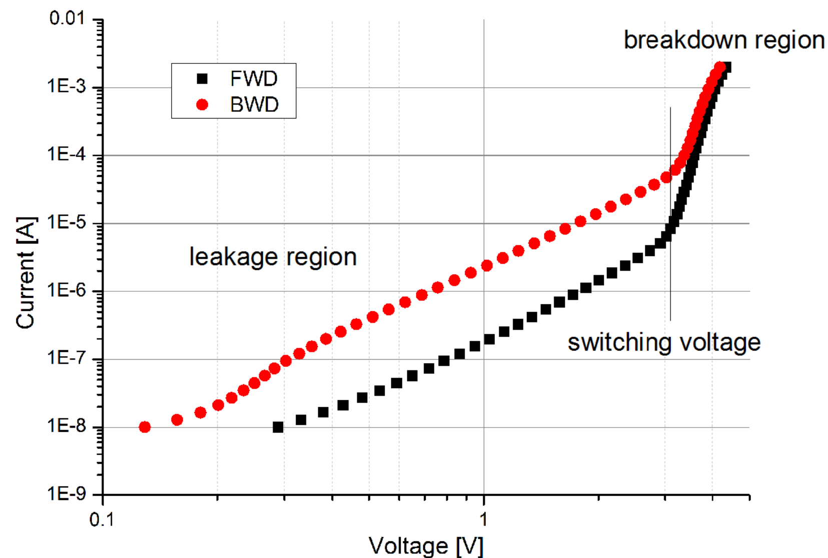

Figure 4.6: Macroscopic I-V curve of a MLV device with pronounced asymmetric behavior, measured at the ISFK; Note the switching voltage of $\sim 3.3\,\mathrm{V}$, the leakage and the breakdown region.

The results of the KPFM and EBSD investigations of the hot spot area can be seen in Fig. 4.8. The electrodes are visible as vertical stripes in all three images. The height image (Fig. 4.8 a)) reveals the individual ZnO grains which differ in their abrasion behavior during polishing. For the ZnO grains a height variation of about 20 nm and a lowering relative to the electrodes was found. The microstructure shows only the ZnO phase and some pores at the grain boundaries and triple junctions, as expected for a

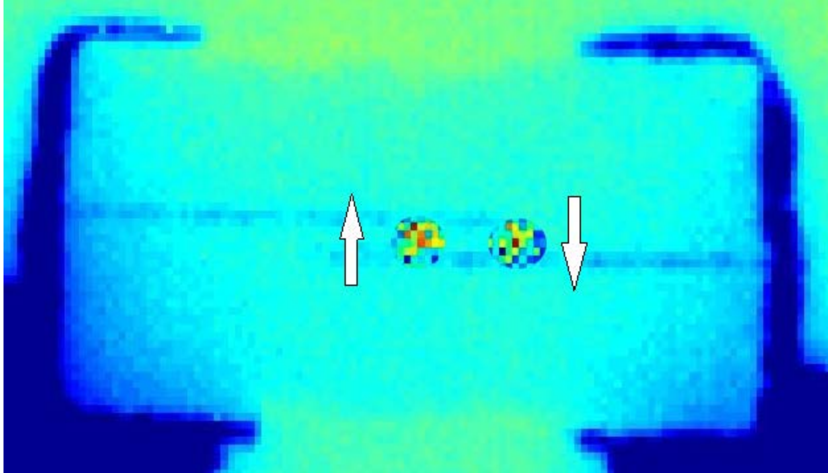

Figure 4.7: Thermography phase image of the sample with asymmetric behavior: The hot-spots are marked with insets from the amplitude image. Arrows indicate the current direction according to the corresponding hot spot.

Pr-system ZnO varistor ceramic. The individual ZnO grains differ also clearly in their work function which is shown in the CPD image (Fig. 4.8 b)). The difference in CPD is due to the different crystallographic orientation of the ZnO grains. An estimated workfunction of 5 eV [38]. for the TiN coated probe results in a workfunction of 4.6 eV for the Ag-Pd electrodes (Ag: 4.26 eV; Pd 5.4 eV) and between 4.85 eV and almost 5 eV for the ZnO grains. The investigated area was subsequently investigated with EBSD to reveal the crystallographic orientation of the individual grains (Fig. 4.8 c)).

The images in Fig. 4.9 a) and b) present an SSPM investigation of the same area as in Fig. 4.8. This sample features only one pair of electrodes, where the left electrode was grounded, to reduce the electrostatic influence of the applied voltage on the cantilever which is coming from the left side. The bias voltages of -1 V (in Fig. 4.9 a)) and $+1$ V (in Fig. 4.9 b)) were applied to the right electrode. The measured SSPM signal is the sum of the surface potential distribution and the CPD. The ZnO grains show across the entire grain an almost constant potential and the voltage changes occur mainly at the grain boundaries. This illustrates the much higher conductivity of the bulk material compared to the grain boundaries. The difference between the electrodes and the adjacent ZnO grains is contributed mainly by the CPD difference. As already reported by Hirose et al. [25], almost the entire voltage drops at the ZnO-ZnO grain boundaries (indicated by arrows) and only a small fraction appears at the ZnO-Ag/Pd electrode junctions.

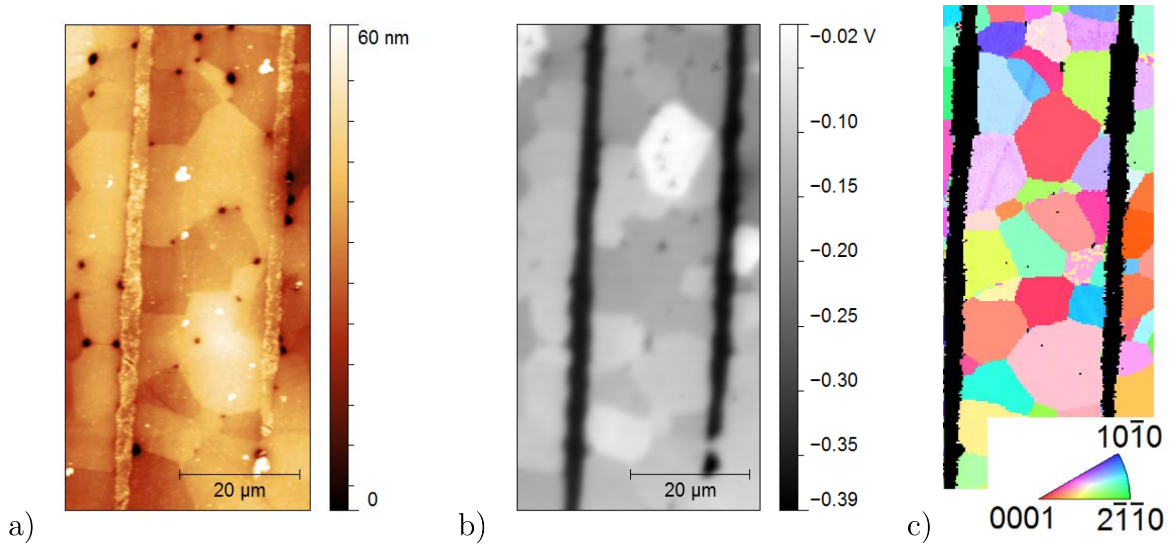

Figure 4.8: Polished MLV cross section of the hot spot area, a) AFM height image, b) CPD image, c) EBSD image.

In order to obtain quantitative data, it is worthwhile to analyze cross sections of the SSPM data. The potential profiles in Fig. 4.9 c) - f) are taken along the lines 1 - 4 in Figs. 4.9 a) and b). The lines 1 and 2 are taken in an area with only one ZnO-to-ZnO grain boundary between the electrodes. Both lines share the larger grain on the right side. The profiles with an applied voltage of $-1\,\mathrm{V}$ (Fig. 4.9 c)) overlap besides a small difference caused by the different CPD. Remarkable are the curves with $+1\,\mathrm{V}$ bias (Fig. 4.9 d)), which show a clear difference of $0.15\,\mathrm{V}$ in potential of the two left grains which can not be explained by the difference in CPD. This means that the barrier between ZnO and the electrode material becomes more pronounced. From this fact it is assumed that the ZnO-ZnO grain boundary along line 2 has a decreased resistance for one bias direction. This lowered resistance causes the formation of a preferred current path in one direction and therefore the hot spot.

The cross sections 3 and 4 in Fig. 4.9 e) and f) are taken in areas with two ZnO-ZnO grain boundaries between the electrodes. The overall voltage drop is again the externally applied bias of $\pm 1\,\mathrm{V}$. Whereas the individual drops or steps show different values. The voltage drops in cross section 3, (Fig. 4.9 e)), show a clear deviation for positive and negative applied bias. Remarkable is especially the left ZnO grain, adjacent to the grounded electrode, where the lines do not overlap. Cross section 4 (Fig. 4.9 f) is an example where the voltage drops show less asymmetry and the grain adjacent to the electrode has nearly the same potential for both applied biases. This means that -

even at current paths with more than one involved ZnO GB - pronounced asymmetric behavior can be found.

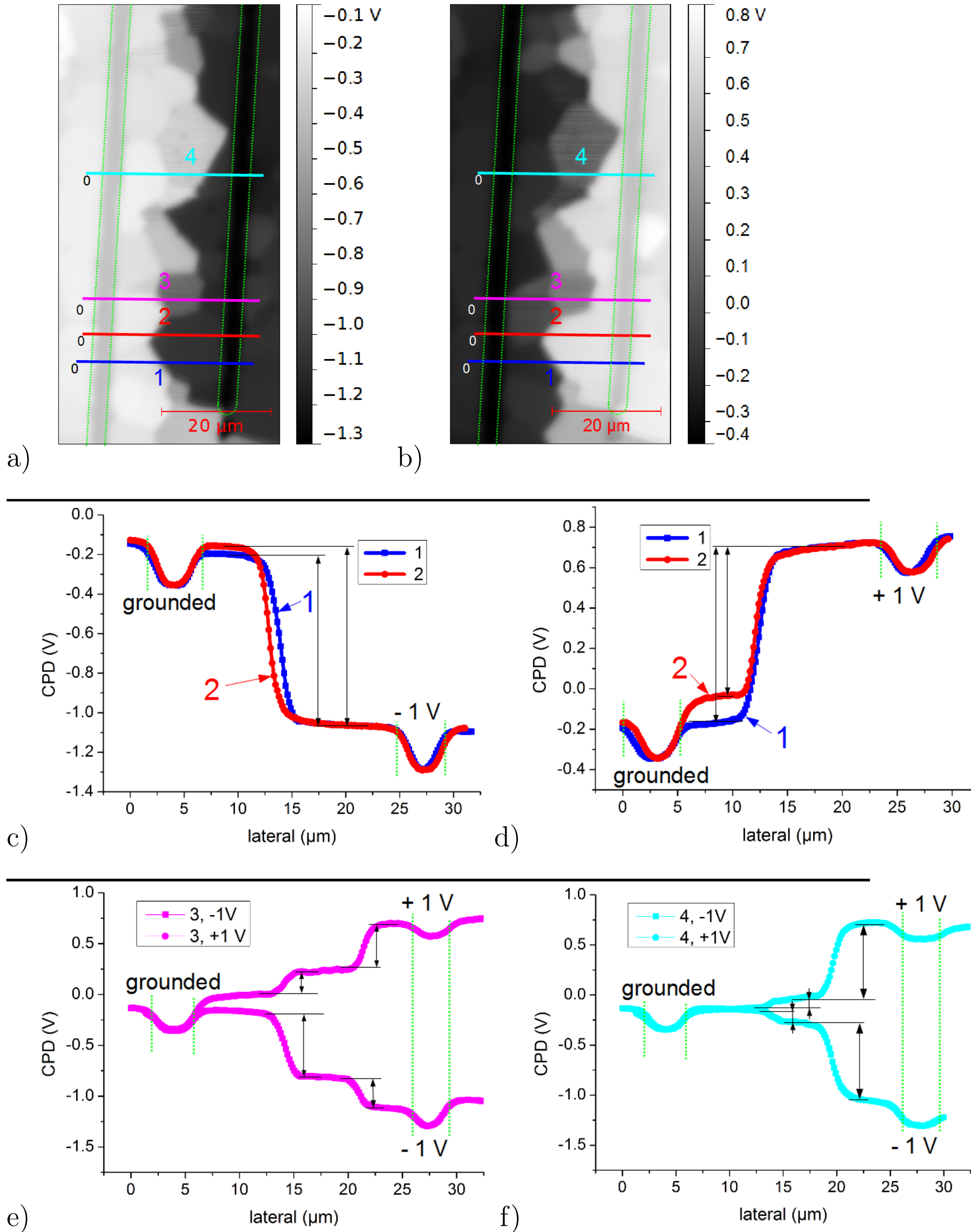

Figure 4.9: SSPM investigation of the hot spot area; a) SSPM image with $-1\,\mathrm{V}$ bias applied; b) SSPM image with $+1\,\mathrm{V}$ bias applied; c) cross sections at lines 1 and 2 at $-1\,\mathrm{V}$; d) cross sections at lines 1 and 2 at $+1\,\mathrm{V}$; e) cross sections at line 3, both directions; f) cross sections at line 4, both directions.

5 µm grain size sample

The sample presented in Fig. 4.10 is an example for a combined KPFM and SSPM investigation on a 5 µm grain size system. The height and CPD images are depicted in Fig. 4.10 a) and b). It was possible to apply a bias of 8 V between the MLV electrodes due to the smaller grain diameter without risking a damage of the sample. The resulting SSPM map is depicted in Fig. 4.10 c). A 3D graph was chosen to illustrate the typical terrace like potential levels.

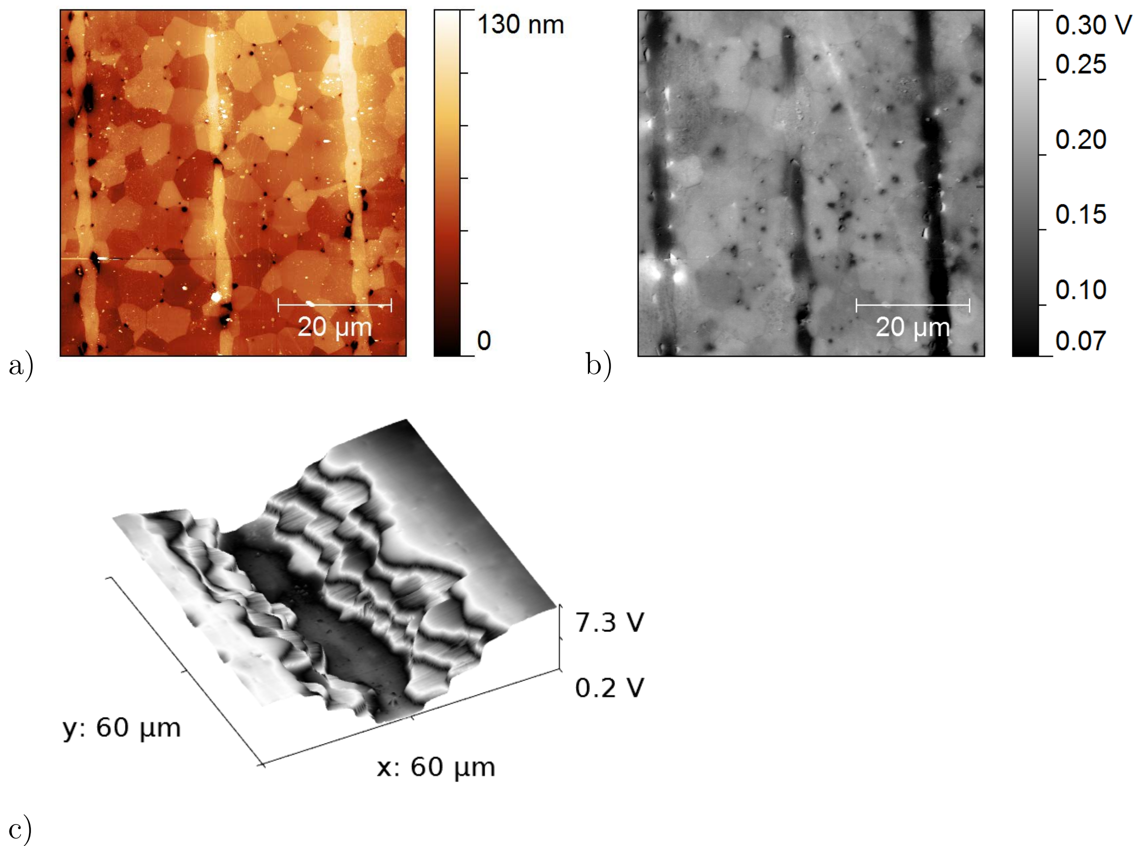

Figure 4.10: KPFM and SSPM study of a sample with 5 µm grain size; a) Height image; b) CPD map; 3D SSPM profile at + 8 V applied

4.1.3 SIM investigations

The aim of the scanning impedance microscopy (SIM) measurements was to obtain frequency dependent electrical properties of individual varistor grain boundaries. Such frequency dependent properties are the charging of the GB and thus the capacity, the movement of ions in the electric field, the width of the depletion layer, and the charge carrier mobility. Additional to the frequency dependence, varistor GBs show a highly non-linear current-voltage behavior which means that the conductivity is also depending on the magnitude of the applied voltage. The SIM measurements were performed during a stay at the Center for Nanophase Materials Science (CNMS), at the Oak Ridge National Lab (ORNL), Tennessee, USA. The model employed for analysis and data interpretation that has been tried to use here was proposed by S. Kalinin for SIM investigations of ferroelectric $BiFeO_3$ [33]. In this model every ZnO GB is assumed as a parallel circuit of a resistor (R_{GB}) and a capacitor (C_{GB}) as depicted in Fig. 4.11. The resistances of the grain interiors (R_{GI} and R_{GII}) are not included in the considerations due to their small contribution to the device behavior.

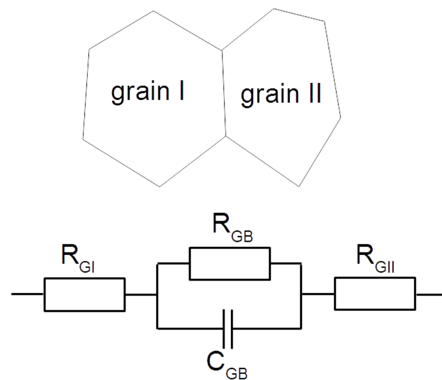

Figure 4.11: Equivalent circuit model of a grain boundary.

Equation 4.5 describes the impedance or complex resistance at the grain boundary between the two grains i and j:

$$Z_{GB\,i-j}(V_{DC},\omega) = \frac{1}{\frac{1}{R_{GB\,i-j}(V_{DC})} + i\omega C_{GB\,i-j}(V_{DC},\omega)} \tag{4.5}$$

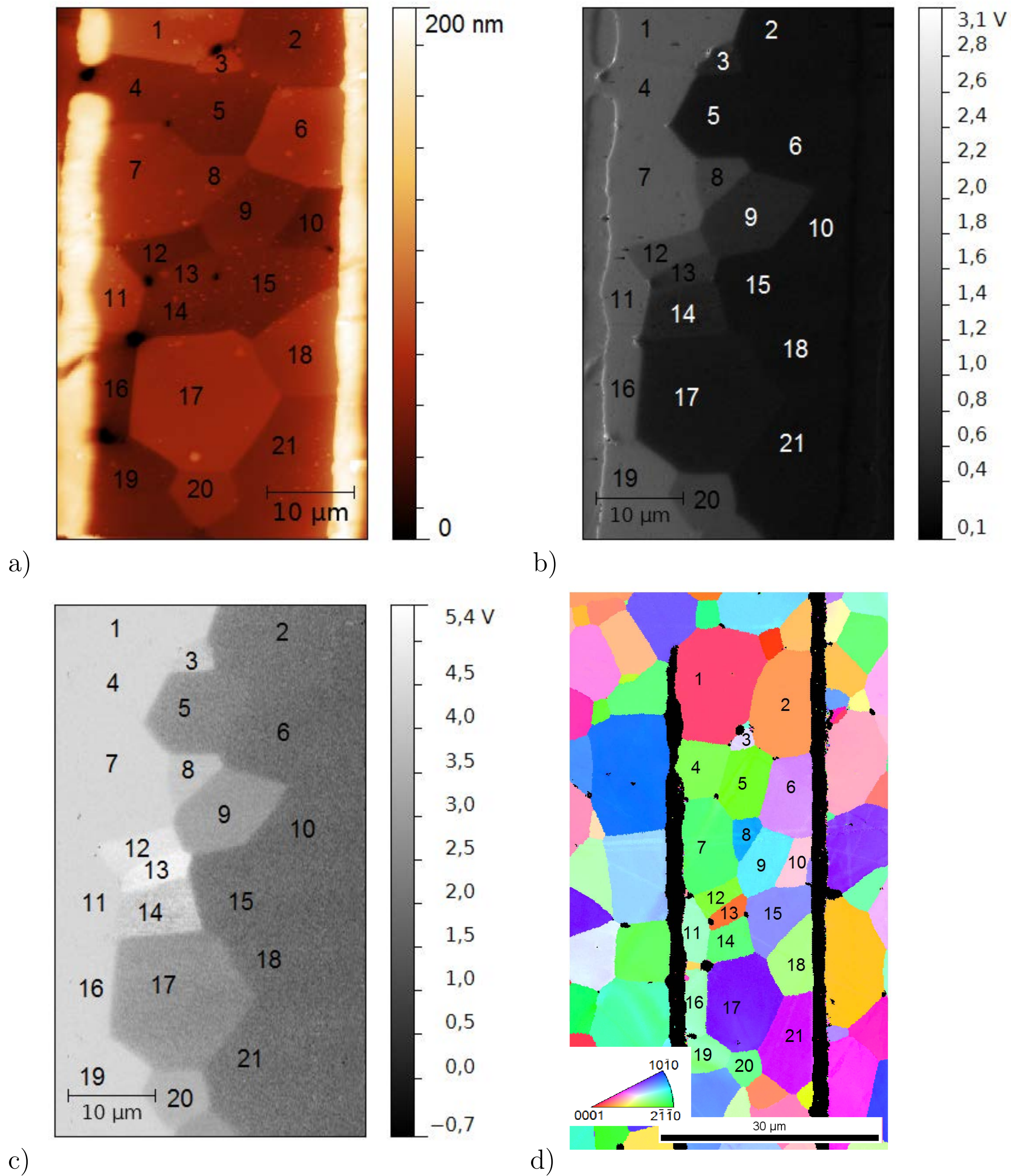

Figure 4.13: SIM measurements at 0V, 20 kHz; a) heigt image; b) SIM amplitude; c) SIM phase; d) EBSD map of the same area; The numbers indicate the investigated ZnO grains.

The same are was also investigated by SSPM (see Fig. 4.14) to obtain the local DC potential V_{DCloc}.

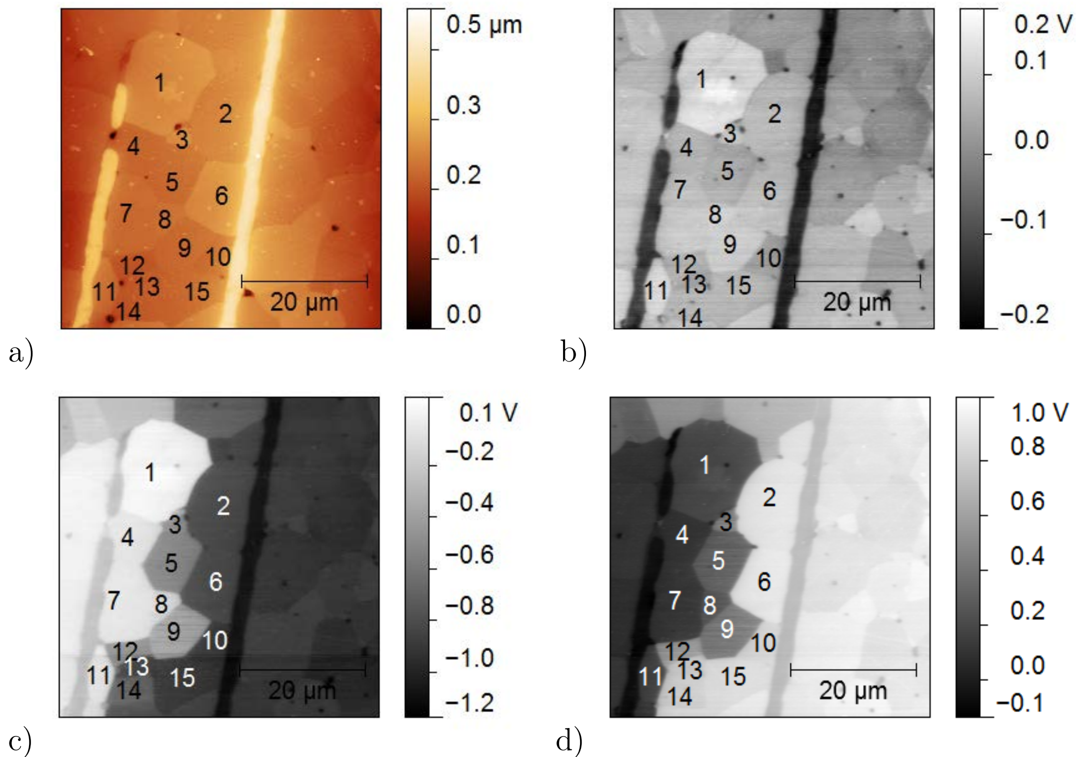

Figure 4.14: SSPM measurements of the area which was investigated by SIM with indicated ZnO grains; a) height image; b) CDP map; c) SSPM measurement at −1 V; d) SSPM measurement at +1 V;

For further analysis, especially the ZnO grains nr. 13 and 14 are considered, because these two grains share grain 11 as closest connection to the left electrode and grain 15 as closest connection to the right electrode. This makes a difference between these two grains independent from the properties of their neighboring grains. In Fig. 4.15 the local SIM amplitudes over external DC voltage and AC frequency are plotted for the grains 11, 13, 14, and 15. A strong increase of the measured amplitude at 60 kHz was observed for all measurements.

This significant increase is most likely caused by an measurement error. The resonance frequency of the employed AFM cantilever was at 70 kHz and thus the signal is strongly amplified close to that frequency. Additional, topography and SIM signal were measured in our first attempt applying single pass technique and not in a two pass mode which has been proposed in the literature [17, 18].

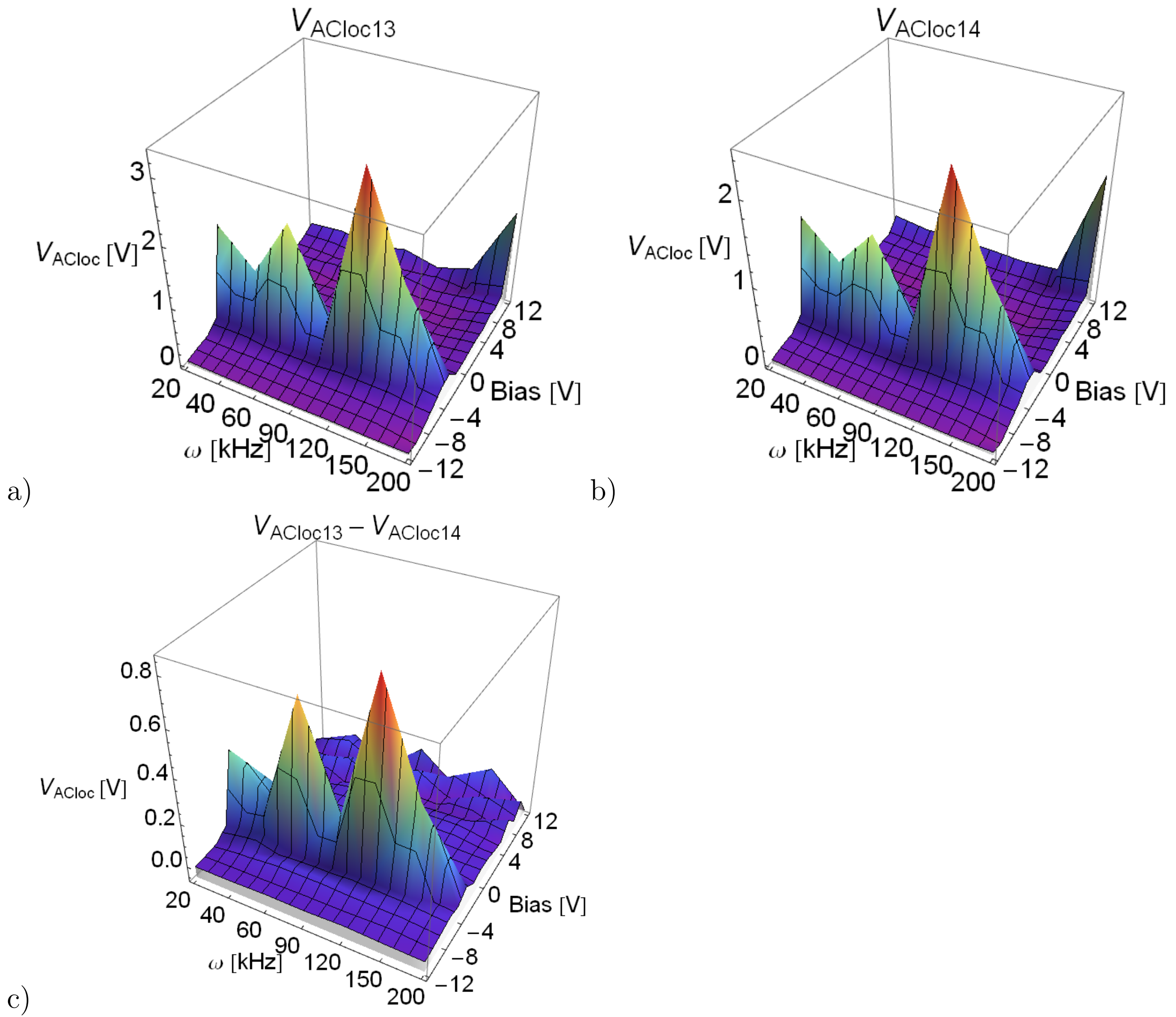

Figure 4.16: V_{ACloc} plotted over external DC bias and AC frequency; a) V_{ACloc} grain 13; b) V_{ACloc} grain 14; c) V_{ACloc} difference between grains 13 and 14.

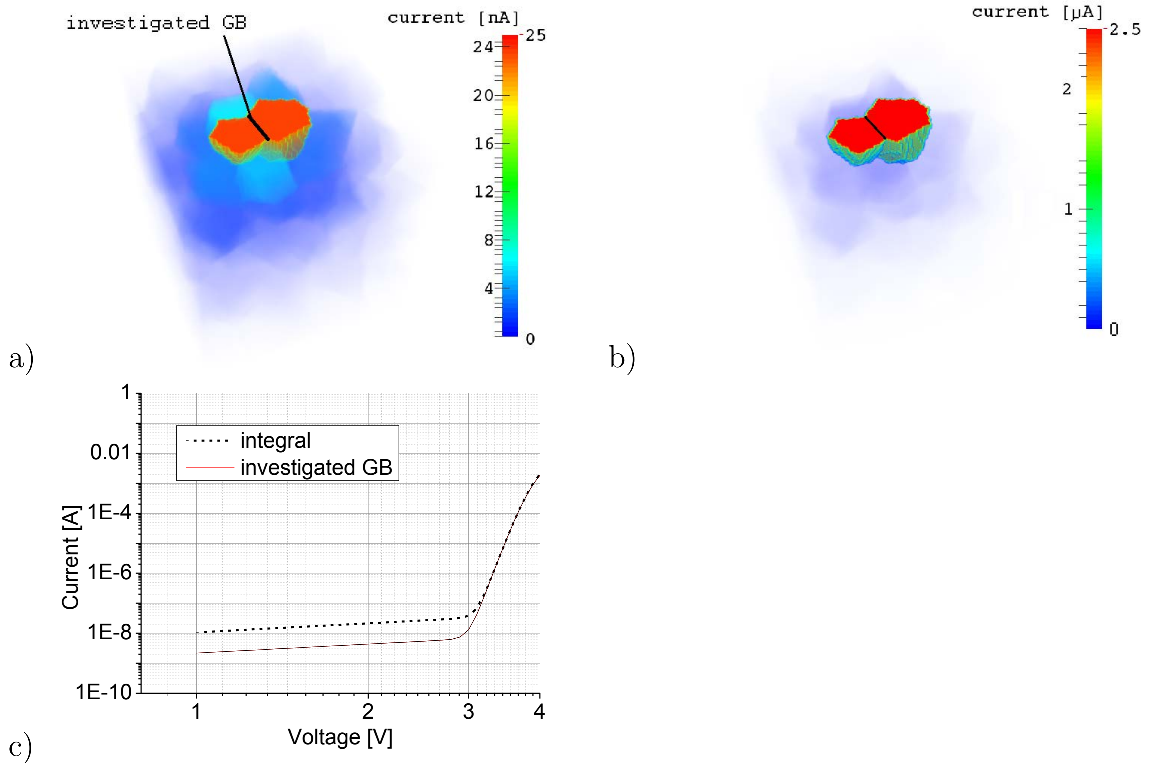

Figure 4.17: Simulated M4PP measurement; a) relative current flow at 2.2 V; b) relative current flow at 3.4 V; c) simulated I-V characteristics for the investigated GB and the entire ensemble in a double logarithmic plot.

4.2.2 Experimental results

In the following, the results of M4PP measurements of individual ZnO grain boundaries and of individual ZnO grain - MLV electrode interfaces are presented. As convention, forward direction (FWD) means a positive voltage applied to probe 1, backward direction (BWD) means a negative voltage applied to probe 1. The samples were taken from the series with 8 μm grain size and only one pair of electrodes.

ZnO-ZnO grain boundary properties

For the ZnO grain boundary measurements, the varistor electrodes were grounded to prevent electrostatic charging of the samples, and only the inactive area (not between the MLV electrodes) with at least two grain boundaries distance from the electrodes was investigated to avoid current flow through the varistor electrodes.

4.3 Bismuth system, AFM based investigations

4.3.1 C-AFM investigations

A C-AFM investigation of a Bismuth doped sample is presented in Fig. 4.25. The heigt image in a) shows ZnO grains and other phases like spinel eclusions and the grain boundary phase as described in section 2.2.3. The electrode can be clearly seen in the current image Fig. 4.25 b). As already seen for the Pr system, the ZnO grains represent areas with constant current signal. The highest current is found in grains close to the electrodes and is decreasing with distance to the electrode. Nonconductive phases appear in the current image as dark areas mainly between the conductive ZnO grains. In the current image a diagonal eight to nine µm wide stripe, which shows no current signal can be seen. This stripe is assumed to origin from a thin film of residuals from the sample preparation. To increase the visibility of grains with a lower current the color scale was set from 0 to 1 nA whereas the maximum current of the white areas is 10 nA.

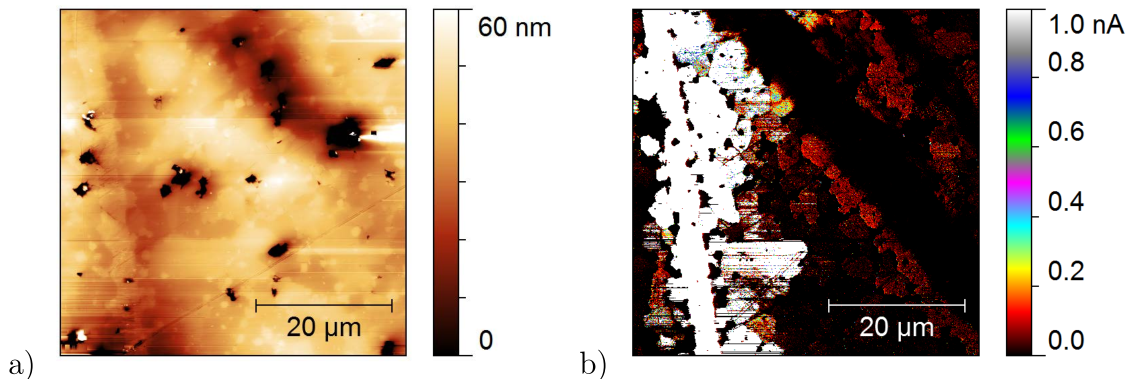

Figure 4.25: C-AFM investigation of a Bi system sample; a) height image; b) current image at + 8 V.

Photolithographic deposition of silver dots

In order to establish Ohmic contacts between the AFM tip and the sample surface, Ag dots were deposited with a photolithographic process on a Bi system sample by J. Fleig, TU Wien. The sample with dots is displayed in an optical micrograph in Fig. 4.26 a) and in an AC mode height image in Fig. 4.26 b). The Ag dots are circular with a diameter of 5 µm and a height of ~50 nm. The white debris with a height of ~0.6 µm

above the dots is regarded as residual from the photolithographic process. The density of the deposited dots caused short circuits over ZnO grain boundaries and the residuals from the photolithographic process were covering the AFM tip. Therefore meaningful electrical measurement were not possible and this method was not further pursued.

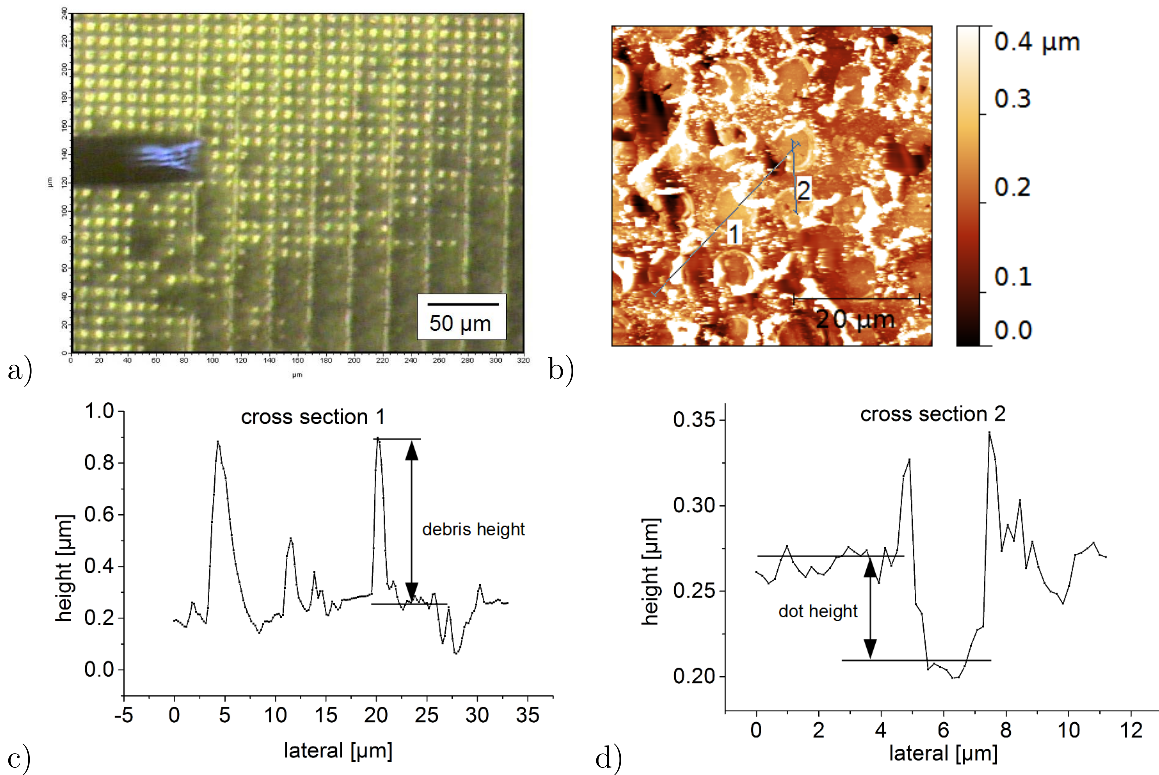

Figure 4.26: Photolithographic deposited Ag-dots; a) optical microscopy image; b) height image; c) cross section 1; d) cross section 2.

4.3.2 KPFM and SSPM investigations

The results of a KPFM and SSPM investigation of a Bi system sample are displayed in Fig. 4.27. For this investigation, a specimen with an average grain size of 5 µm and an electrode distance of approximately 30 µm was used. The typical microstructure of a Bi system (see section 2.2.3) can be seen in the height image, Fig. 4.27 a) and in the CPD image Fig. 4.27 b). The spinel phases with a diameter of less than 1 µm are found at the grain interior. The Bi-rich phase at the grain boundary and especially at the grain triple junctions is strongly visible as bright areas in the CPD image. Also, several holes with a diameter up to 5 µm can be seen in the microstructure. These holes are pores from

sintering or breakouts from polishing. Fig. 4.27 c) and d) are SSPM scans wit a bias of −8 V and +8 V applied. The red marked cross sections are displayed in Fig. 4.27 e). A terrace like structure can be seen as in the Pr system samples. The spinel phases are not visible in the SSPM images since they are at the same potential as the surrounding grain.

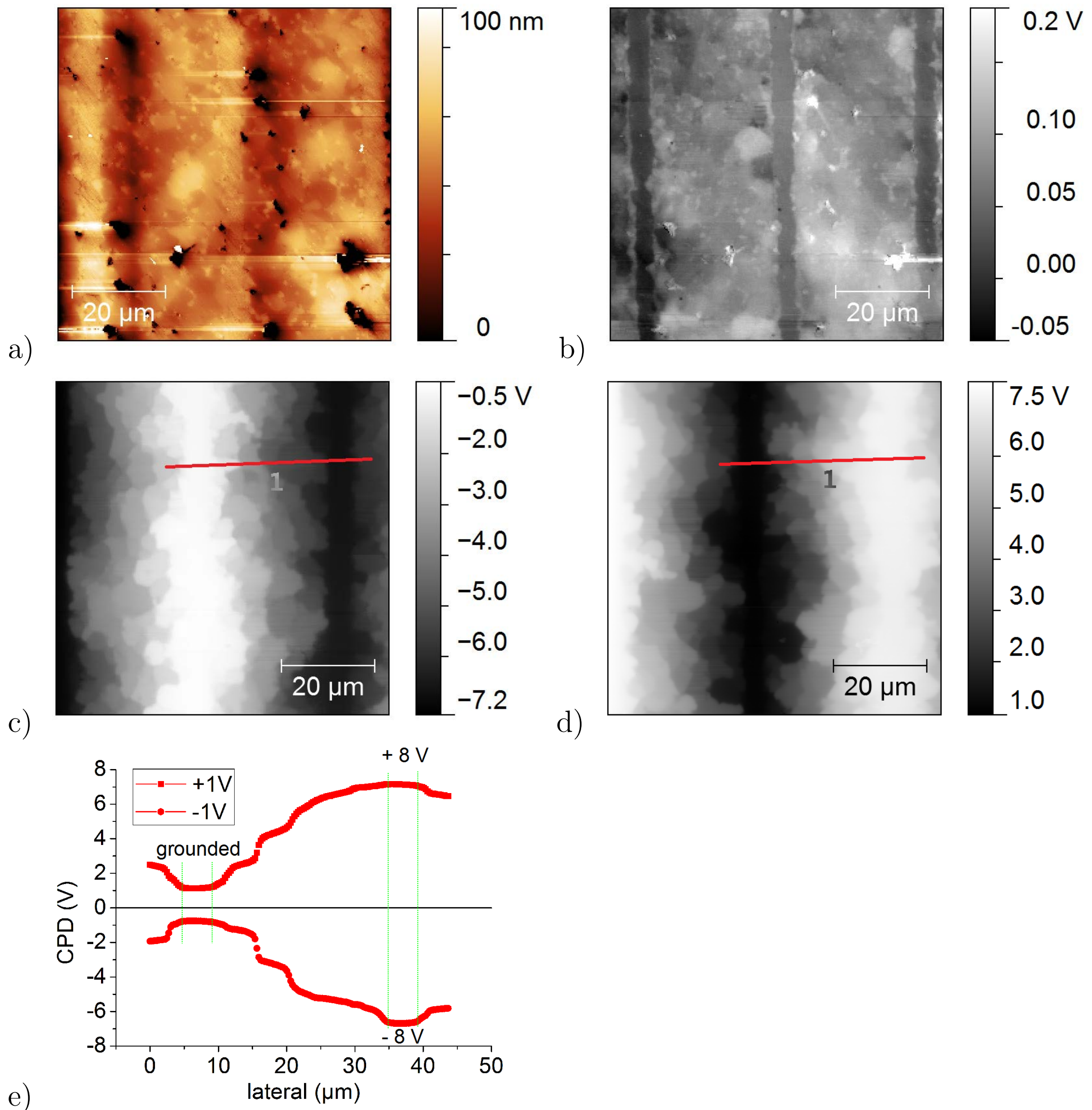

Figure 4.27: KPFM and SSPM investigation of an Bi doped specimen; a) height image; b) CPD map; c) SSPM map at −8 V; d) SSPM map at +8 V; e) cross sections from c) and d)